Ex Fission ad Astra:
Extending Nucleon-Nucleus Interactions to the Fission Fragment Region

by

Kyle Beyer

A dissertation submitted in partial fulfillment
of the requirements for the degree of
Doctor of Philosophy
(Nuclear Engineering and Radiological Sciences)
in the University of Michigan
2024

Doctoral Committee:

Associate Professor Brian C. Kiedrowski, Chair
Professor Christine Aidala
Dr. Amy Lovell, Los Alamos National Laboratory
Professor Sara Pozzi
Dr. Cole Pruitt, Lawrence Livermore National Laboratory

"But to return to the main thing, that prompt and delayed. Now what are the orders of magnitude of these things? Well, if you take a look at a neutron resonance of a few volts, electron volts, the lifetime is of the order of [...] 10 to the minus 15 seconds. On the other hand, the structure [of fluctuations in the total cross section] is of the order of a few MeV or more. Now that gives you a lifetime, or a time constant if you wish, of the order of 10 to the minus 22, 10 to the minus 23 seconds. So you have an enormous range between 10 to the minus 15 and 10 to the minus 23. And the question is, isn't there something in between? So of course, again, instead of asking the question directly or trying to answer it directly, we looked at some phenomena. You know, without experimentalists we'd be all dead."

— Herman Feshbach[1]

[1]Addressing an audience at the Massachusetts Institute of Technology in a lecture titled: "The Optical Model" [54].

Kyle Beyer

beykyle@umich.edu

ORCID iD: 0000-0002-2695-2478

Dedicated to my parents, Mona and Larry Beyer

Acknowledgments

I have the privilege of having a long list of people to whom I am indebted to for their collaboration and support. First, my advisor Brian Kiedrowski, with whom I've been working since I was an undergraduate at Michigan, who has been instrumental in my young career in research;

My collaborators in this work, Cole Pruitt and Amy Lovell, who have provided invaluable advice on both technical and professional topics, and have had large hands in shaping this project;

My committee members, Professors Christine Aidala and Sara Pozzi, who have been involved in my education since my undergraduate years;

Courtney Wagoner, for her indispensable administrative expertise;

Meghan McGarry, who made the connections that lead to this project;

Pablo Giuliani and Daniel Odell, who were already working on what I wanted to work on but better, and let me join along for the ride, and Pablo again for getting me a great job;

Stefano Marin and Nathan Giha, to whom I am indebted to and inspired by for their curiosity and ambition to pursue the scientific questions that fascinate them. This work wouldn't be possible without their input and enthusiasm about nuclear fission. I miss our late night talks about physics;

To Aaron Tumulak, who has always been my first line of defense when I don't understand something, and amongst the first to whom I excitedly explain something when I actually do understand it;

To Mike Hua, Devin Mussells, Flynn Darby, Zach Welker, Lauren Green, Ashwin Rao, Chris Swenson, and Maria diMayorca, your friendship and camaraderie made my (long) tenure at Michigan a membership in a community rather than a job;

Outside of work, I am indebted to my family and friends for their love and support. To my parents, Mona and Larry, and my siblings Kaitlyn and Matt, I am incredibly lucky to have you;

To Dana my love, you inspire me and keep me grounded. To Emmy, many of my best ideas have come on our walks together; you always know just what to say. If they let dogs be co-authors you would have your share of credit;

To Gabe and Jared, my oldest and closest friends. I don't know where I'd be without you, but it sure wouldn't be here;

To Yeabsera, Marissa, Kunal, Zach, Yatri, Kat and Charlie; your friendship is so important to me. Thank you for keeping me aware that there is a world outside of physics;

Finally, it is thanks to the influence of three skilled educators at the Battle Creek Area Mathematics and Science Center, in Walter Erhardt, and Karen and Charlie Payson, that I am on the path that I'm on today.

Preface

This work was funded by the Consortium for Monitoring, Technology, and Verification under Department of Energy National Nuclear Security Administration Award Number DE-NA0003920, performed under the auspices of the U.S. Department of Energy by Los Alamos National Laboratory under Contract 89233218CNA000001 and under the auspices of the U.S. Department of Energy by Lawrence Livermore National Laboratory under Contract DE-AC52-07NA27344.

This research was supported in part through computational resources and services provided by Advanced Research Computing (ARC), a division of Information and Technology Services (ITS) at the University of Michigan, Ann Arbor.

Table of Contents

List of Figures

Abstract

A key ingredient for modeling nuclear reactions of all kinds is the optical potential, an effective interaction between nucleons and nuclei. Formally, it results from a reduction of the many-body quantum mechanics of the A-body nucleus to a single-nucleon scattering state interacting with an A-1 body core, and can be constructed microscopically using realistic nucleon-nucleon forces. However, the workhorses in nuclear reaction modeling and nuclear data evaluation are phenomenological optical potentials, fit primarily to elastic scattering cross sections on β-stable isotopes. Extrapolating to unstable, neutron rich, isotopes — as in the case for nuclear fission, or the astrophysical r-process — presents a source of un-quantified uncertainty.

In this work, we take steps to push the boundary of our quantitative modeling of nuclear reactions away from the valley of β-stability and into the fission fragment region. We perform the first uncertainty quantification and comparison of optical models in observables relating to the de-excitation of fission fragments, using a phenomenological potential constrained by decades of scattering data, and a microscopic potential built from chiral forces consistent with quantum chromodynamics. We find large uncertainties, especially for neutron-fragment correlated observables, and discuss future calibrations of fission model parameters. Next, we discuss the relationship between nuclear matter and the optical model. We explore the implications of the isovector dependence of the optical potential on the symmetry energy of nuclear matter, a fundamental quantity governing phenomena from the scale of nuclei to neutron stars. We show that scattering observables on β-stable nuclides are poor constraints of the symmetry energy, relative to a theoretical approach.

Finally, to make future Bayesian calibration of optical potentials to new constraints, like those from fission, more computationally tractable, we develop and demonstrate a novel,

projective model order reduction scheme, Active Subspace Quilting, an extension of the Reduced Basis Method to nonlinear manifolds. We demonstrate a 3 order of magnitude speedup with negligible loss of accuracy.

Chapter 1

Introduction & Motivation

Nuclear physics connects phenomena at length scales from the subatomic to the astrophysical, and governs the core of all the matter we interact with every day. Understanding how free nucleons interact with nuclei is an important window into this field, which is foundational to science, society and security. Our current understanding of nuclear reactions is limited by the tractability of the many-body quantum problem in finite systems. Current ab-initio methods are limited to light ions for exact dynamics including continuum degrees of freedom [126]. For reactions involving larger isotopes, the typical approach is to use an effective nucleon-nucleus interaction, arising from the formal reduction of the many-body degrees of freedom to an effective single-particle problem, for which exact dynamics are tractable. This effective interaction, the optical model potential (OMP), has been studied for at least 7 decades [81].

The ubiquity of the effective nucleon-nucleus interaction as an ingredient in reaction theory motivates the quest for an accurate nucleon-nucleus OMP that describes target isotopes across the nuclear chart (a global OMP). Particular effort is being made to construct such a global model that is predictive out to the drip lines, that simultaneously describes bound states and the continuum, and is consistent with the theoretical underpinnings of the strong force. This will likely be a core activity of the nuclear reaction theory community

in the coming decades [75].

Nuclei are bound by the strong nuclear force, which arises from quantum chromodynamics (QCD). QCD is an asymptotically free theory at high energy. As the universe cooled, the quark and gluon degrees of freedom condensed into complex, color-neutral baryonic structures which have a self-interaction mediated by residual color polarization; akin to a Van-der-Waals force between electrically neutral polarized atoms or molecules. Further cooling leads to the further condensation of these nucleons into a dizzying diversity of structures produced across the nuclear chart: the atomic nuclei. Understanding how nucleons self-organize into such diverse and complex structures, and how this behavior arises from the symmetries of the underlying high-energy degrees of freedom, is a foundational goal of nuclear physics, and the subject of chiral effective field theory (χ-EFT) [114]. Recently, a global microscopic optical potential, the Whitehead-Lim-Holt (WLH) potential, has been constructed from the effective nucleon self-interaction in nuclear matter using chiral forces consistent with QCD [178].

On the other hand, the workhorses in nuclear reaction theory are phenomenological global OMPs. These models are parameterized in a variety of functional forms, and their parameters are calibrated to elastic scattering experiments on stable targets, which yield differential elastic scattering cross sections and analyzing powers at a variety of beam energies, as well as angle integrated elastic and total cross sections. In applications, such as those surveyed in section 1.1, these models are often then extrapolated away from stability, for which experimental data are unreliable or non-existent. Is this extrapolation justified?

Global phenomenological OMPs such as Koning-Delaroche (KD) [95] provide workhorse models for the nucleon-nucleus interactions that are key ingredients in reaction phenomenology. This is exemplified in Fig. 1.1, which compares the isotopes to which KD was calibrated, to the fission product yield (FPY) in the spontaneous fission of ^{252}Cf. Modeling the de-excitation of fragments produced in nuclear fission is an important example of an application requiring predictive OMPs away from stability, and is examined in this work.

However, the extrapolation away from the isotopic and energy regions for which these models are fit introduces uncertainty that is unquantifiable using only experimental data from the valley of β-stability. A recent advance in phenomenological global optical potentials was the construction of an updated, uncertainty-quantified, version of the KD potential using Bayesian statistics, the Koning-Delaroche uncertainty quantified (KDUQ) potential [139, 140].

Confronting the KDUQ and WLH potentials to a broad range of orthogonal experimental and theoretical constraints relating to nuclei away from stability is thus a useful activity; the phenomenological model well reproduces its corpus of training data, but requires extrapolation that microscopic approaches do not. The microscopic approach is consistent with the underlying symmetries of QCD, but requires its own theoretical approximations, the limits of applicability of which have yet to be charted.

Addressing the fundamental questions in nuclear physics, and the applications subsequently surveyed, requires an understanding of nuclear reaction phenomenology away from stability [75, 145]. The advent of the rare isotope beam era has begun to widen the experimentally accessible region of the isotopic chart, with significant increases still to come [19]. Few-body reaction theory provides an important framework to study these phenomena, and is underpinned by assumptions about the nucleon-nucleus interaction; the optical potential. Corresponding experimental efforts which study exotic nuclei or astrophysically relevant nuclei using transfer and breakup reactions [125, 104], single-particle spectra and quenching in knockout reactions [6], nuclear fission to understand far from equilibrium many-body nuclear dynamics [155], characterizing reactions involving the production and decay of compound nuclei due to their ubiquity; all of these require an OMP for interpretation.

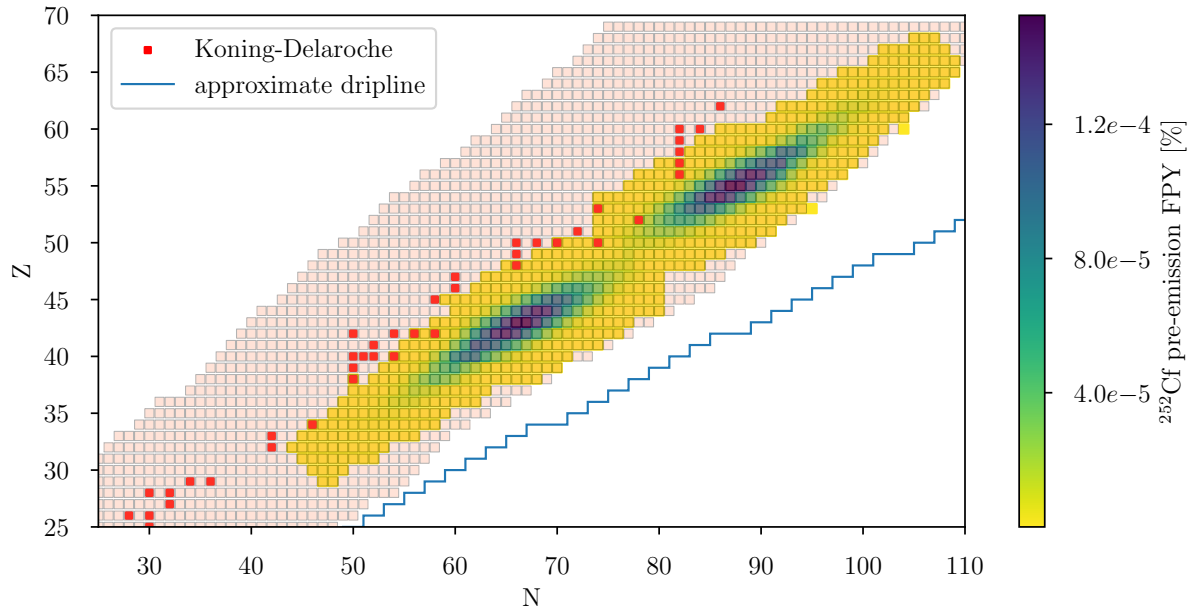

Figure 1.1: Chart of isotopes in the fission fragment region, where the isotopes used to constrain the commonly used Koning-Delaroche phenomenological neutron-nucleus global optical potential [95] (red squares) are compared to ^{252}Cf (*sf*) pre-emission fragment yield distributions (or FPY), as generated by CGMF [160]. Also included for demonstration is the approximate location of the neutron dripline, ascertained by the location at which the neutron removal threshold, as calculated using the semi-emprical mass formula, crosses 0; $S_N(N,Z) = E_B(N,Z) - E_B(N-1,Z) < 0$.

1.1 Survey of applications of optical potentials for neutron-rich isotopes

Observed elemental abundances of metal-poor stars, and measured meteoric and solar system isotopic abundances, display a variety of peaks corresponding to different mechanisms of nucleogenesis in the universe. The locations of peaks and associated isotopic abundances paint a picture in which roughly half the elements heavier than iron had their genesis in an astrophysical rapid-neutron capture process (the r-process), which flowed far from the valley of stability and through neutron-rich nuclei. The conditions required for such reactions are extreme neutron densities; $\sim 10^{20}\text{cm}^{-3}$ [104]. The gravitational wave observation of neutron star merge GW170817 by the LIGO/VIRGO collaboration in 2017, and the observation over subsequent days and weeks of the γ-ray ("kilonova") afterglow resulting from the β-decay of unstable neutron-rich nuclei, unambiguously confirmed neutron star mergers as r-process sites [1, 4]. However, they may not be the only ones; core-collapse supernovae and other compact object mergers have been postulated as r-process sites, amongst many others [136]. Other interesting candidates include the tidal disruption of white-dwarf stars in the gravitational field of intermediate mass black holes [3, 147]. Fig. 1.2 summarizes current knowledge of the nucleogenesis of the periodic table.

Unraveling the mysteries of the origin of the atomic nuclei requires modeling the cataclysmic astrophysical events required to produce the sufficient conditions for the r-process. Simulations of the gravitational and electromagnetic signals of these events provide clues about where to point telescopes to make interesting observations. This task requires as a model input the masses, β-decay half lives and delayed emission probabilities, and thermally-averaged radiative neutron capture (n,γ) cross sections, for the roughly 5000 neutron-rich isotopes throughout the reaction network. The results are highly sensitive to the neutron capture cross section, especially in the "cold" r-process in which thermal equilibrium in neutron capture and photodisintegration is never achieved [104]. The r-process

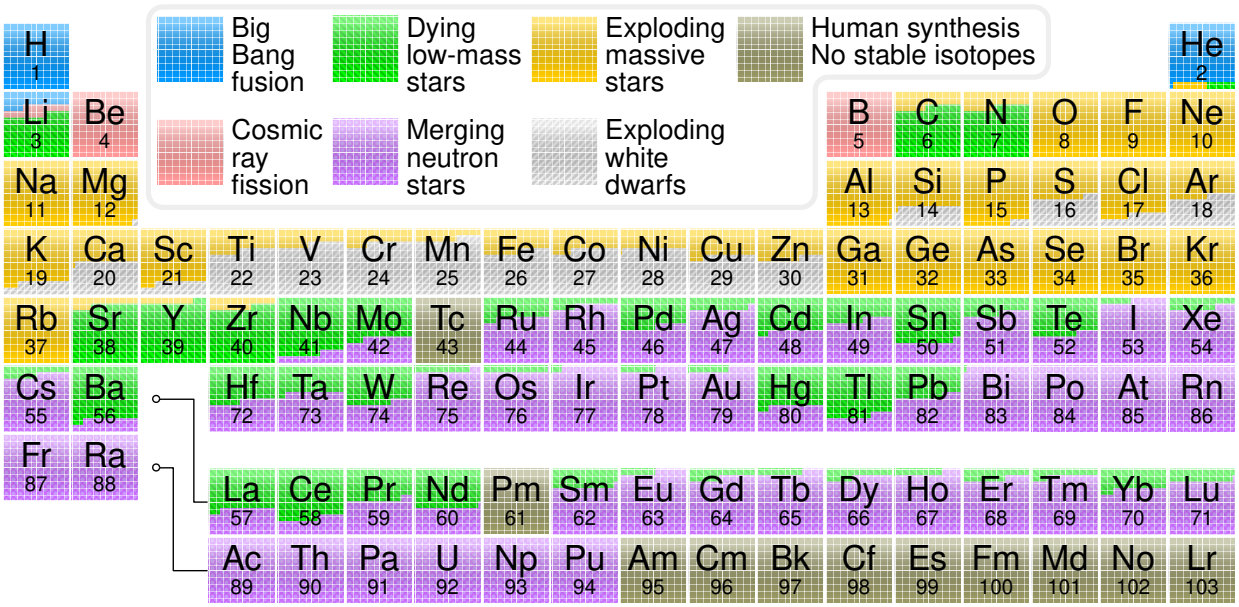

Figure 1.2: A periodic table colored by mechanism of nucleosynthesis, reprinted from [35]

is the mechanism expected to have produced the actinides, and when the flow reaches these heavy elements, "fission recycling" can occur, where fission products repopulate the intermediate mass neutron-rich nuclei in the reaction network; thus another model input becomes the distribution of fission products. Few of these properties can be directly measured due to the β-instability of the relevant neutron-rich target isotopes, in particular, evaluation of the (n,γ) cross sections and fission product yields often rely on phenomenological global optical potentials, extrapolated far from the β-stable and spherical isotopes to which they are calibrated [104].

Outside of the big scientific questions relating to nucleogenesis, the optical potential is an important ingredient for the treatment of any reactions involving compound nuclei, many of which have implications on technology, society and security. Constraining their extrapolation away from stability will improve the description of the prompt de-excitation of neutron-rich fission fragments, and the yields of long-lived fission products. Fission event generators are required for simulation of any system in which event-by-event correlations amongst fission products are relevant, which includes nuclear non-proliferation

scenarios such as portal monitoring and standoff measurements [146]. Accurate fission event generators are also important for the interpretation of experimental fission observables relating to open questions about the scission process [180, 155, 63, 116, 117], and for evaluation of prompt fission neutron spectrum (PFNS) and other fission quantities for actinides [165, 25]. Monte Carlo Hauser-Feshbach (MCHF) codes, such as CGMF used in this work, are commonly employed in these efforts, as fission produces multiple correlated signatures [112, 113, 160].

Optical potentials are relied upon as a tool in the evaluation of nucleon-nucleus cross sections, especially where experimental data is lacking. Improving accuracy of evaluated cross sections for nuclei in the fission fragment region is important for applications in energy, national security and medicine [146]. Particular scenarios include modeling the fuel depletion in nuclear fission power reactors, perturbations to or diversions from spent nuclear fuel in containment, nuclear forensics scenarios, active interrogation of special nuclear material, as well as medical diagnostics, imaging and treatment using radiation [75].

1.2 Uncertainty quantification and model order reduction

While the optical potential is an important component of much of nuclear reaction theory and is upstream of nuclear data relevant to many applications, it is also one of the greatest sources of uncertainty in reaction analysis [75, 139]. The development of uncertainty-quantified OMPs, with special focus on neutron-rich isotopes, has been the subject of a recent corresponding theoretical effort. Simultaneously, there has been a focus on applying rigorous uncertainty quantification using Bayesian statistics to the calibration of phenomenological optical potentials [139, 31, 108, 94, 110, 30, 157]. It is becoming clear that the resulting uncertainties on derived observables due to the optical model can be substantial, and Bayesian analysis allows for a more accurate characterization, and systematic

reduction, of them.

It has long been known that the OMP is multi-modal, exhibiting ambiguities where multiple parameter values produce identical observables [81]. Thus, statistical analyses of phenomenological models should consider model parameter spaces holistically, sequentially introducing new and orthogonal data as constraints until the multi-modality is eliminated. An illustrative example discussed by Hodgson [81] is the discrete ambiguity in the depth of the real part of the optical potential: multiple regularly spaced values (e.g. $\sim 50, 100, 150 \ldots$ MeV) all reproduce scattering observables. However, the depth of ~ 50 MeV corresponds to shell model binding energies, and thus the larger depth modes can be rejected as unphysical. It is thus with the holistic incorporation of quantities which treated as urelated — in this case, both binding energies and cross sections — that the model becomes both predictive and unique; a necessary condition if one has any hope of extrapolation. It is also by this same process that those quantities, which are unrelated in their measurement, become related in their description by a single, unique, and unified model.

These Bayesian studies often require the calculation of observables at hundreds of thousands or even millions of samples in parameter space, thus nuclear physicists have in recent years turned to the well-established field of model order reduction to construct computationally efficient emulators [121]. In particular, the reduced basis method (RBM), a type of projective model order reduction (PMOR) has emerged as a valuable tool in nuclear reaction theory [64, 20]. These methods have the potential to be transformative, allowing for uncertainty quantification that would otherwise require high-performance computing centers to be performed on personal computers. By the same token, the combinations of emulators and high-performance computing has the potential to allow access problems that would otherwise be intractable.

1.3 Outline of dissertation

The remainder of this dissertation is organized as follows:

- Chapter 2 develops the mathematical formalism of the OMP, the effective nucleon-nucleus interaction, beginning with the many-body nuclear Hamiltonian. The approach taken is most closely related to the Feshbach-Fano partitioning, but its relation to nuclear matter and many-body propagator theoretical approaches is discussed. Particular attention is paid to the construction of the two models under consideration in this work: KDUQ and WLH. By considering the distribution of complex-energy eigenvalues of the many-body nuclear Hamiltonian as a distribution, the statistical approach to the compound nucleus (CN) is developed and connected to the OMP.

- Chapter 3 discusses the role of this picture of the CN in the de-excitation of fission fragments. Next it presents the methodology and results of the first uncertainty-quantification of fission observables due to both a phenomenological and a microscopic optical potential, making detailed comparison to experiment. We find significant uncertainties, especially in neutron-fragment correlated observables. The prospect of directly constraining optical potentials with fission observables is discussed.

- Chapter 4 reviews the relation between the optical potential and the symmetry energy of nuclear matter and its density slope. It discusses the implications of this relation on the optical potentials considered in this work, and compares to results from terrestrial experiments and astrophysical observations. We find that scattering observables on β-stable isotopes are poor constraints of the symmetry energy, and recommend future phenomenological global optical potentials include bound state information.

- Chapter 5 discusses the need for computationally efficient surrogate models to make possible the model calibration proposed in the previous chapters, and in the applica-

tion of Bayesian statistics to nuclear reaction phenomenology at large. The formalism for the RBM is developed, the software `Reduced Order Scattering Emulator (ROSE)` is presented, and results are demonstrated for Bayesian calibration of a local optical potential, showing speedups of 2 to 3 orders of magnitude with negligible loss of accuracy. Then, the novel active subspace quilting (ASQ) method is developed and demonstrated, extending the RBM to global optical potentials.

- Chapter 6 summarizes the results of the different pieces of this work, reconnects them to the broader scientific and societal context, and discusses the path forward.

Chapter 2

Theoretical Formalism

In this chapter we introduce the many-body Hamiltonian, in the framework of the *target-state expansion*, to formulate an infinite multi-channel problem. Using the *optical reduction* we will exactly reduce this to an effective problem on an arbitrary, finite subset of our Hilbert space: the $\mathbb{P}$-space. We will understand this reduction in terms of the Feshbach projection-operator formalism, or Feshbach-Fano partitioning [56, 55], although this reduction has been performed in other contexts by reducing a many-body Green's function, using tools developed in the context of the Landau quasi-particle theory [76, 44, 42, 115, 90], and the formalisms are equivalent in scattering [115, 42, 90]. This technique can also be understood in terms of a similarity transformation on the many-body Hamiltonian that softens the hard-core component of the nucleon-nucleon interaction [158].

We will then derive the Hauser-Feshbach branching ratios by making statistical assumptions about the distribution of eigenvalues of the complimentary $\mathbb{Q}$-space Hamiltonian, which will allow us to factorize the amplitudes for process involving a compound nucleus into transmission coefficients between incoming and outgoing channels. This will determine the governing equations for the de-excitation process.

Finally, we will discuss practical aspects of calculating optical potentials, and examine the two optical potentials used in this work: Whitehead-Lim-Holt (WLH) and Koning-

Delaroche uncertainty quantified (KDUQ).

2.1 The optical reduction

Consider the many-body Hamiltonian for an $A+1$-body nucleus, in the center of mass frame:

$$\mathcal{H}^{A+1} = \sum_{i}^{A+1} T_i + \sum_{ij}^{A+1} V_{ij} + \sum_{ijk}^{A+1} V_{ijk} + \ldots \tag{2.1}$$

where $T_i = \frac{\hbar^2 k_i^2}{2\mu_i}$ is the center-of-mass frame kinetic energy of nucleon i. Here, we see that nucleons in a many-body system feel two, three, and, generally, N-body forces, where the sums are over pairs of nucleons in the first force term, and over all sets of three nucleons in the second, etc. In particular, 3-body forces are expected to play a more prominent role in neutron-rich nuclei [78]. However, the inclusion of 3-body forces in the formalism is trivial[1] and is neglected going forward.

We can factor the $A+1$-body Hamiltonian into a core A-body Hamiltonian, and a single-particle Hamiltonian. The latter contains kinetic energy, as well as the sum of interactions of all A nucleons in the core with our single nucleon:

$$\mathcal{H}^{A+1} = \mathcal{H}^{A} + T_{A+1} + \sum_{i}^{A} V_{i,A+1}. \tag{2.2}$$

We refer to the last term in Eq. 2.2 as the *final state interaction* when nucleon $A+1$ is in a scattering state. We have a complete and orthonormal set of $A+1$ body states and corresponding energies, and likewise for the A-body states:

[1] In practical ab-initio calculations of microscopic optical potentials, realistic 3-body forces may, in fact, be a great complication. For our purposes, however, the inclusion of 3-body forces amounts to a change in the coupling potential $V_{n'n}^{j'l',jl}$ of Eq. 2.11, but does not impact the concept of the optical reduction that constructs the effective nucleon-nucleus force from it.

$$\mathcal{H}^{A+1} |\Psi_m^{A+1}\rangle = E_m |\Psi_m^{A+1}\rangle \tag{2.3}$$

$$\mathcal{H}^{A} |\Psi_n^{A}\rangle = E_n |\Psi_n^{A}\rangle \,. \tag{2.4}$$

We decompose the asymptotic Hilbert spaces acted upon by these Hamiltonians into channels. At negative energies we have a discrete spectrum of bound states of the $A+1$ system, and at positive energies we have a dense spectrum of product states consisting of an excited residual core and a single particle in scattering state

$$|nkjl\rangle \equiv |\Psi_n^A\rangle \otimes |kjl\rangle \,, \tag{2.5}$$

where

$$|kjl\rangle \equiv |k\rangle \sum_m \mathcal{Y}_{jl}^m \tag{2.6}$$

$$= |k\rangle \sum_{m_s m_l} i^l \langle lsm_l m_s | jm\rangle \, Y_l^{m_l} \chi_s^{m_s} \tag{2.7}$$

is the state of nucleon $A+1$, with asymptotic kinetic energy $E = \hbar^2 k^2 / 2\mu$, with μ being the reduced mass of the system. Here, l, $s = 1/2$ and j respectively label the orbital, spin and total angular momentum quantum numbers, with m_l, m_s and m their respective projections. $\chi_s^{m_s}$ is the spin wavefunction, Y_l^m are the orbital wavefunctions, e.g., the spherical harmonics, and $\mathcal{Y}_l^{m_l}$ are the corresponding spin-orbital angular wavefunctions. For a thorough discussion of this partial wave expansion, see Section A.1.

The neutron-removal threshold is $S_N^{A+1} = E_0^{A+1} - E_0^A$, where $n = 0$ refers to the ground state of the respective system. The Fermi energy for neutrons in the A-body system lies at $\epsilon_F \equiv -S_N^{A+1}$ (for neutrons in particle states, neutron holes have a slightly different Fermi energy, and all their energies lie below it, rather than above it). Thus, we have a discrete

spectrum of excited states of the A-body system for $-S_N^{A+1} < E < 0$, and a dense spectrum for $E > 0$ corresponding to continuum states. A similar analysis holds for protons.

We have an infinite number of such channels, each described by one of these excited states of the residual core. We label them by n. For compactness, we will use this labeling for both discrete and continuum states, and use the summation symbol $\sum$ to indicate a sum over discrete states, and an integral over the continuum. The positive energy S_N^A is the threshold for removal of a second neutron, and so on.

It is important to remember that, while we have orthonormality for the eigenstates of $\mathcal{H}^{A/A+1}$, the states $|nkjl\rangle$ are not necessarily normalized or orthogonal to any $|\Psi_n^{A+1}\rangle$. In fact, the normalization of such an overlap $\langle\Psi_m^{A+1}|0kjl\rangle$ is referred to as a *spectroscopic factor*; it is the projection of the ground $(n = 0)$ A-body state with a single nucleon in scattering state $|kjl\rangle$ onto the excited state $|\Psi_m^{A+1}\rangle$. In a non-interacting system, these are all unity. It is the presence of correlations that causes a fragmentation of the single-nucleon energies (or, equivalently, a mixing of single-nucleon states), placing nucleons above the Fermi-energy and corresponding holes below it.

Of course, energy, parity and total angular momentum are symmetries of the center-of-mass (COM)-frame Hamiltonian, so we have a triangular sum rule for total angular momenta given an initial $A + 1$ nucleus in some state m:

$$|I_n - j| < I_m < I_n + j, \tag{2.8}$$

as well as conservation of energy,

$$E_m = E + E_n. \tag{2.9}$$

We use the *target-state expansion*; projecting $\left(\mathcal{H}^{A+1} - E\right) = 0$, using the $A + 1$-body Hamiltonian as written in Eq. 2.2, onto the target states, Eq. 2.5, yielding the coupled-channels equation:

$$\langle n'k'j'l'| \left(-\frac{\hbar^2}{2\mu}\frac{d^2}{dr^2} + \sum_{n'} V_{n'n}^{j'l',jl} - (E - E_n^A) \right) |nklj\rangle = 0. \tag{2.10}$$

Here, we have defined the channel coupling potential as resulting from the target-state expansion of the final state interaction:

$$V_{n'n}^{j'l',jl} = \sum_{m',m} \left\langle \Psi_{n'}^A \otimes \mathcal{Y}_{j'l'}^{m'} \middle| \sum_i^A V_{i,A+1} \middle| \mathcal{Y}_{jl}^{m} \otimes \Psi_n^A \right\rangle. \tag{2.11}$$

This is an infinite[2] system of coupled single-body equations, which can be solved by truncation, provided a suitable model for the nucleon and transition densities for the relevant excited states, and 2-body nucleon forces V_{ij}. The amplitude for a given transition is provided by the asymptotic values of the wavefunctions in the coordinate basis, $\lim_{r\to\infty} \langle r|nkjl\rangle$.

Rather than truncating, we will exactly account for propagation of states not explicitly included in the expansion using the Feshbach-Fano partitioning [181], which we will formulate explicitly in terms of the Green's functions, following [162]. We begin by partitioning the A-body Hilbert $\mathbb{H}^A$ space into compliments; $\mathbb{H}^A = \mathbb{P} \oplus \mathbb{Q}$, using respective idempotent projection operators $\mathcal{P} : \mathbb{H}^A \to \mathbb{P}$ and $\mathcal{Q} : \mathbb{H}^A \to \mathbb{Q}$:

$$\begin{aligned} \mathcal{P} &\equiv \sum_{n\in\mathbb{P}} |\Psi_n^A\rangle \langle \Psi_n^A| \\ \mathcal{Q} &\equiv \sum_{m\in\mathbb{Q}} |\Psi_m^A\rangle \langle \Psi_m^A|, \end{aligned} \tag{2.12}$$

which have the properties

[2]This is uncountably infinite, in fact, if continuum A-body states are included

$$\begin{aligned}
\mathcal{P} + \mathcal{Q} &= \mathbb{1} \\
\mathcal{P}^2 &= \mathcal{P} \\
\mathcal{Q}^2 &= \mathcal{Q} \\
\mathcal{Q}\mathcal{P} &= \mathcal{P}\mathcal{Q} = 0.
\end{aligned} \tag{2.13}$$

We will then formally solve the system for states in $\mathbb{P}$ using the propagator for channels in the $\mathbb{Q}$-space. We have:

$$\begin{aligned}
\mathcal{H}^{A+1} &= T_{A+1} \\
&\quad + \mathcal{P}^\dagger \left(\mathcal{H}^A + \sum_i^A V_{i,A+1} \right) \mathcal{P} \\
&\quad + \mathcal{Q}^\dagger \left(\mathcal{H}^A + \sum_i^A V_{i,A+1} \right) \mathcal{P} \\
&\quad + \mathcal{P}^\dagger \left(\mathcal{H}^A + \sum_i^A V_{i,A+1} \right) \mathcal{Q} \\
&\quad + \mathcal{Q}^\dagger \left(\mathcal{H}^A + \sum_i^A V_{i,A+1} \right) \mathcal{Q} \\
&\equiv \mathcal{H}_{\mathcal{P}\mathcal{P}} + \mathcal{H}_{\mathcal{P}\mathcal{Q}} + \mathcal{H}_{\mathcal{Q}\mathcal{P}} + \mathcal{H}_{\mathcal{Q}\mathcal{Q}},
\end{aligned} \tag{2.14}$$

where the last equality defines the symbols $\Lambda^\dagger \mathcal{H} \Omega = \mathcal{H}_{\Lambda\Omega}$. T_{A+1} operates outside the A-body Hilbert space, and commutes with $\mathcal{P}$ and $\mathcal{Q}$; however, we will absorb it into $\mathcal{H}_{\mathcal{P}\mathcal{P}}$ for convenience. We further define partition Green's functions such that:

$$\begin{aligned}
\lim_{\eta \to +0} G_{\mathcal{P}}(E) \left(E - H_{\mathcal{P}\mathcal{P}} + i\eta \right)^{-1} &\equiv \mathcal{P} \\
\lim_{\eta \to +0} G_{\mathcal{Q}}(E) \left(E - H_{\mathcal{Q}\mathcal{Q}} + i\eta \right)^{-1} &\equiv \mathcal{Q}.
\end{aligned} \tag{2.15}$$

From here on out, we will drop the limit in our notation, and implicitly assume the limit of η is being taken to 0 from above. The identity

$$A^{-1} = B^{-1} + B^{-1}(B - A)A^{-1} \tag{2.16}$$

can be used to generate a Dyson equation for the full A-body propagator $A^{-1} = G \equiv \left(E - \mathcal{H}^A + i\eta\right)^{-1}$ in terms of the partition Green's functions.

$$G = (G_\mathcal{P} + G_\mathcal{Q}) + (G_\mathcal{P} + G_\mathcal{Q})(\mathcal{H}_{\mathcal{PQ}} + \mathcal{H}_{\mathcal{QP}})G. \tag{2.17}$$

Multiplying from the left by $\mathcal{P}$ or $\mathcal{Q}$, we have the coupled equations

$$\begin{aligned} \mathcal{P}G &= G_\mathcal{P} + G_\mathcal{P}\mathcal{H}_{\mathcal{PQ}}G \\ \mathcal{Q}G &= G_\mathcal{Q} + G_\mathcal{Q}\mathcal{H}_{\mathcal{QP}}G, \end{aligned} \tag{2.18}$$

either of which we can formally solve by substitution. Choosing the former yields

$$\mathcal{P}G = G_\mathcal{P} + G_\mathcal{P}\mathcal{H}_{\mathcal{PQ}}\left(G_\mathcal{Q} + G_\mathcal{Q}\mathcal{H}_{\mathcal{QP}}G\right). \tag{2.19}$$

Multiplying from the left by $(E - \mathcal{H}_{\mathcal{PP}} + i\eta)$ and consolidating terms of G, we have

$$\left(E - \mathcal{H}_{\mathcal{PP}} - \mathcal{H}_{\mathcal{PQ}}G_\mathcal{Q}\mathcal{H}_{\mathcal{QP}} + i\eta\right)\mathcal{P}G = \mathcal{P} + \mathcal{H}_{\mathcal{PQ}}G_\mathcal{Q}. \tag{2.20}$$

Finally, we multiply from the right by $\mathcal{HP}$,

$$\left(E - \mathcal{H}_{\mathcal{PP}} - \mathcal{H}_{\mathcal{PQ}}G_\mathcal{Q}\mathcal{H}_{\mathcal{QP}} + i\eta\right)\mathcal{P}G\mathcal{H}\mathcal{P} = \mathcal{H}_{\mathcal{PP}} + \mathcal{H}_{\mathcal{PQ}}G_\mathcal{Q}\mathcal{H}_{\mathcal{QP}}, \tag{2.21}$$

and, rearranging, we are left with

$$\mathcal{P}G\mathcal{H}\mathcal{P} = G_{om}H_{om} \tag{2.22}$$

where we have defined the optically reduced Green's function,

$$G_{om} \equiv \left(E - H_{om} + i\eta\right)^{-1}, \tag{2.23}$$

as well as the optically reduced Hamiltonian,

$$H_{om} \equiv \mathcal{H}_{\mathcal{PP}} + \mathcal{H}_{\mathcal{PQ}} G_{\mathcal{Q}} \mathcal{H}_{\mathcal{QP}}. \tag{2.24}$$

The significance of this quantity is stated in Eq. 2.22; we have derived a Hamiltonian which produces the same Dyson equation as that of the full Hamiltonian projected onto $\mathbb{P}$. Explicitly evaluating $\mathcal{H}_{om}$ in terms of Eq. 2.2, we have

$$\mathcal{H}_{om} = \mathcal{H}_{\mathcal{PP}} + V_{dpp}, \tag{2.25}$$

where we have defined the *dynamic polarization potential*, which includes virtual effects from states in the $\mathbb{Q}$-space. For any state $|\alpha\rangle \in \mathbb{P}$, we find, by inserting a complete set of A-body states

$$\left\langle \alpha \left| V_{dpp}(E) \right| \alpha' \right\rangle \equiv \sum_{\beta \in \mathbb{Q}} \frac{\left\langle \alpha \left| V^{j'l',jl}_{m'm} \right| \beta \right\rangle \left\langle \beta \left| V^{j'l',jl}_{m'm} \right| \alpha' \right\rangle}{E - E^A_\beta + i\eta}, \tag{2.26}$$

where $|\alpha\rangle$ and $|\beta\rangle$ are shorthand for some state on the appropriate space, e.g. $|nkjl\rangle$. Clearly this is energy dependent, and examination of Eq. 2.11 reveals it is also non-local. Using the identity

$$\frac{1}{z \pm i\eta} = \mathcal{P}\frac{1}{z} \pm i\pi\delta(z), \tag{2.27}$$

(where $\mathcal{P}$ here denotes the principal part, not to be confused with the projection operator onto $\mathbb{P}$) we find that the imaginary part of the dynamic polarization potential gives the strength, as a function of energy, of the final state interaction to couple states on the $\mathbb{P}$-space to the $\mathbb{Q}$-space:

$$\left\langle \alpha \left| \mathfrak{Im}\, V_{dpp}(E) \right| \alpha \right\rangle = \sum_{\beta \in \mathbb{Q}} \left| \left\langle \alpha \left| V^{j'l',jl}_{m'm} \right| \beta \right\rangle \right|^2 \delta(E - E^A_\beta). \tag{2.28}$$

This is called the *strength function* when $|\alpha\rangle$ is on the elastic channel. It is the defect of $\mathcal{H}_{om}$ from Hermiticity, and encapsulates the non-unitary time evolution of the $\mathbb{P}$-states corresponding to loss of flux to $\mathbb{Q}$. It can be shown that, for $|\alpha\rangle$ that are stationary scattering state solutions to $(\mathcal{H}_{om} - E) = 0$, the strength function is proportional to $1 - |\mathcal{S}_{\alpha\alpha}|^2$, the unitary deficit to the $\mathcal{S}$-matrix in the α channel. We define this quantity as the transmission coefficient $\mathbb{T}_\alpha$:

$$\mathbb{T}_\alpha \equiv 1 - |S_{\alpha\alpha}|^2 \tag{2.29}$$

Thus we have a complex, non-local and energy dependent interaction in $\mathcal{H}_{om}$. Similarly, for any states $|\alpha\rangle, |\alpha'\rangle \in \mathbb{P}$, we have

$$\begin{aligned} \langle \alpha | \mathcal{H}_{\mathcal{PP}} | \alpha' \rangle &= T_{A+1} + E^A_\alpha + \left\langle \alpha \left| V^{j'l',jl}_{m'm} \right| \alpha' \right\rangle \\ &\equiv T_{A+1} + E^A_\alpha + V_{\mathcal{PP}} \end{aligned} \tag{2.30}$$

The last term is just the mean force exerted on nucleon $A+1$ by all nucleons in the A-body state labeled by α; we have used it as the definition of $V_{\mathcal{PP}}$. If $|\alpha\rangle$ refers to the ground state, this would be considered the *mean-field* contribution to the optical model potential. We define the optical model potential

$$V_{om} = V_{\mathcal{PP}} + V_{dpp} \tag{2.31}$$

such that

$$\langle \alpha | \mathcal{H}_{om} | \alpha' \rangle \equiv T_{A+1} + E^A_\alpha + \langle \alpha | V_{om} | \alpha' \rangle . \tag{2.32}$$

The corresponding steady-state Schrödinger-like equation generated by Eq. 2.32; $(\mathcal{H}_{om} - E) = 0$, has stationary scattering states as solutions for $E > 0$. It is formally solved by G_{om} (see Eq. 2.23), which generates a Dyson equation for scattering amplitudes in terms of the free

propagator, which we define:

$$G^{(0)}(E) \equiv [E - \mathcal{H}_0 + i\eta]^{-1}. \tag{2.33}$$

Here $\mathcal{H}_0 \equiv \mathcal{H}_{om} - V_{om}$. The resulting Dyson equation, which is the result of the same identity from Eq. 2.16, is:

$$G_{om} = G^{(0)} + G^{(0)}\, V_{om}\, G_{om}, \tag{2.34}$$

or, in terms of the $\mathcal{T}$-matrix:

$$G_{om} = G^{(0)} + G^{(0)}\, \mathcal{T}\, G^{(0)}. \tag{2.35}$$

Here, we have used the definition of the $\mathcal{T}$-matrix:

$$\mathcal{T} \equiv V_{om} + V_{om}\, G_{om}\, V_{om}. \tag{2.36}$$

Combining these two we find the Lippmann-Schwinger equation, which generates the Born series for scattering amplitudes:

$$\mathcal{T} = V_{om} + V_{om}\, G^{(0)} \mathcal{T}. \tag{2.37}$$

It is important to note that the single-nucleon scattering states generated by Eq. 2.37, are really states on $\mathbb{P}$; unnormalized product states of an A-body core state and a single-nucleon scattering state. However, the optically-reduced propagator produces the exact same Dyson equation as that produced by the projected many-body Green's function $\mathcal{P}^\dagger G \mathcal{P}$; this is the statement of the optical reduction.

A few final notes are warranted. It can further be shown that V_{om} should satisfy a dispersion relation [55, 57] which connects the real and imaginary parts over all energies. This has been shown to be related to causality when the formalism is extended to include

both particle and hole states [115]. Optical model potential (OMP) analyses making use of this are referred to as dispersive optical model (DOM) analyses. While they are not considered in this work, they have been used effectively to construct local[3] OMPs that formally connect bound and continuum energy scales [43, 141, 5, 41].

It is useful to consider the alternative Green's function development of the optical potential, e.g. as in [12, 115, 90, 44], as it develops how to construct the relevant many-body states perturbatively using particle-hole excitations on top of the mean field, and formally connects the self-energy to the optical potential in the perturbative expansion of the single-nucleon propagator. This requires extending for formalism to include hole states below the Fermi energy. Capuzzi and Mahoux have pointed out that the Feshbach formalism followed here reproduces the same asymptotic scattering states [27, 28].

2.2 Connecting to scattering quantities

If one were to solve Eq. 2.10 for states in $\mathbb{P}$, or, equivalently, solve $(H_{om} - E) = 0$ using an exact form for V_{om}, in coordinate space, one would typically use a *partial wave expansion*, and the result would be the set of partial-wave states $\{\psi_n^{jl}(r) \equiv \langle r|nkjl\rangle\}_{n\in\mathbb{P}}$. These are stationary 1-body scattering states, and their asymptotic behavior determines amplitudes and subsequent cross sections. This asymptotic analysis can be performed in the coordinate basis using a double Fourier-Bessel transform [44], or in the time-dependent formalism in terms of the Møller operators [162]. In the latter case one explicitly sees that the time-evolution on the $\mathbb{P}$-space is non-unitary, and that this imaginary component of V_{om} results in a non-unitary $\mathcal{S}$-matrix. We understand the loss of flux from the $\mathbb{P}$-space through the transmission coefficients defined in Eq. 2.29.

We will take the time-dependent approach, first defining the $\mathcal{S}$-matrix as a product of isometric operators — the Møller operators — mapping from asymptotic scattering states

[3] That is to say, isotopically local within the chart of isotopes. DOM analysis requires the use of an optical potential that is non-local in coordinate space.

to the actual scattering orbits, following [162]:

$$\langle \alpha | \mathcal{S} | \alpha' \rangle \equiv \langle \alpha | \Omega_-^\dagger \Omega_+ | \alpha' \rangle \,. \tag{2.38}$$

The Møller operators are in turn defined

$$\Omega_\pm \equiv \lim_{t \to \mp\infty} e^{i\mathcal{H}_0 t} e^{-i\mathcal{H}t}. \tag{2.39}$$

We are concerned with $\mathcal{H} \equiv \mathcal{H}_{om}$, $\mathcal{H}_0 \equiv \mathcal{H}_{om} - V_{om}$. That is, our full Hamiltonian is the optical Hamiltonian, and the "free" Hamiltonian corresponds to that of nucleon $A+1$ not interacting at all with the residual core, as is the case asymptotically. We can write

$$\langle \alpha | \mathcal{S} | \alpha' \rangle = \lim_{t \to \infty} \langle \alpha | \left[e^{i\mathcal{H}_0 t} e^{-2i\mathcal{H}t} e^{i\mathcal{H}_0 t} \right] | \alpha' \rangle \,. \tag{2.40}$$

We can generate an integral equation in terms of asymptotic states by writing the derivative of the quantity in brackets $[\dots]$ as

$$\frac{d}{dt} [\dots] = -i \left(e^{i\mathcal{H}_0 t} V_{om} e^{-2i\mathcal{H}t} e^{i\mathcal{H}_0 t} + e^{i\mathcal{H}_0 t} e^{-2i\mathcal{H}t} V_{om} e^{i\mathcal{H}_0 t} \right). \tag{2.41}$$

We now write the $\mathcal{S}$-matrix as the time integral of this quantity:

$$\begin{aligned} \langle \alpha | \mathcal{S} | \alpha' \rangle &= \langle \alpha | \alpha' \rangle - i \lim_{\epsilon \to +0} \int_0^\infty dt e^{-\epsilon t} \langle \alpha | \frac{d}{dt} \mathcal{S} | \alpha' \rangle \\ &= \langle \alpha | \alpha' \rangle - i \lim_{\epsilon \to +0} \int_0^\infty dt e^{-\epsilon t} \langle \alpha | \left(e^{i\mathcal{H}_0 t} V_{om} e^{-2i\mathcal{H}t} e^{i\mathcal{H}_0 t} + e^{i\mathcal{H}_0 t} e^{-2i\mathcal{H}t} V_{om} e^{i\mathcal{H}_0 t} \right) | \alpha' \rangle \,. \end{aligned} \tag{2.42}$$

We have introduced the damping factor ϵ, which is justified if the original integral is absolutely convergent. This requirement is intimately related to the requirement that the interaction potential be localized in space, e.g., approaches 0 sufficiently rapidly as $r \to \infty$ [162]. However, if this is not the case, one can always reformulate $\mathcal{H}_0$ to subtract out the

long-range component, which requires treatment of the asymptotic scattering states as under the influence of that long-range force. This is how Coulomb potentials are treated.

When $|\alpha\rangle = |nkjl\rangle$, e.g. α describes a stationary scattering state in channel n, we have

$$\begin{aligned}\langle nkjl|\mathcal{S}|k'j'l'n'\rangle &= \delta(k-k')\delta_{ll'}\delta_{jj'}\delta_{nn'} \\ &\quad -i\lim_{\epsilon\to+0}\int_0^\infty dt\left\langle nkjl\right| V_{om}e^{i\Delta-2\mathcal{H}t-\epsilon} + e^{i\Delta-2\mathcal{H}t-\epsilon}V_{om}\left|n'k'j'l'\right\rangle,\end{aligned} \tag{2.43}$$

where $\Delta \equiv E_{k'} + E_k$. We can evaluate this integral in terms of the optical Green's function, yielding

$$\begin{aligned}\langle nkjl|\mathcal{S}|n'k'j'l'\rangle &= \delta(k-k')\delta_{ll'}\delta_{jj'}\delta_{nn'} \\ &\quad +\frac{1}{2}\lim_{\epsilon\to+0}\langle nkjl|\,V_{om}G_{om}(\Delta/2+i\epsilon) + G_{om}(\Delta/2+i\epsilon)V_{om}\,|n'k'j'l'\rangle\,.\end{aligned} \tag{2.44}$$

Using the Lippmann-Schwinger equation (Eq. 2.37), we can write the $\mathcal{S}$-matrix in terms of the $\mathcal{T}$-matrix:

$$\begin{aligned}\langle nkjl|\mathcal{S}|n'k'j'l'\rangle &= \delta(k-k')\delta_{ll'}\delta_{jj'} \\ &\quad +\frac{1}{2}\lim_{\epsilon\to+0}\left[\frac{1}{E_{k'}-E_k+i\epsilon}-\frac{1}{E_{k'}-E_k-i\epsilon}\right]\langle nkjl|\,\mathcal{T}_{om}(\Delta/2+i\epsilon)\,|n'k'j'l'\rangle \qquad (2.45)\\ &= \delta(k-k')\delta_{ll'}\delta_{jj'}\delta_{nn'} - 2\pi i\delta(E_{k'}-E_k)\langle nkjl|\,\mathcal{T}_{om}(E_k)\,|n'k'j'l'\rangle\,. \qquad (2.46)\end{aligned}$$

We have used the definition of $\delta(z)$ to achieve this final result, which is our expected relation between the on-shell $\mathcal{T}$ and $\mathcal{S}$ matrices. We see that, indeed, the scattering observables are entirely determined by the value of either $\mathcal{S}(E)$ or $\mathcal{T}(E)$ at $E = \frac{\hbar^2k^2}{2\mu}$.

The asymptotic analysis in the time-independent formalism is equivalent [162]. It is worthwhile performing as well, as, when performed in the momentum basis, it readily yields the differential scattering, as well as total and reaction cross sections. As mentioned,

the transformation to the coordinate frame using a double Fourier-Bessel transform provides a partial wave expansion in orbital angular momentum quantum numbers l, which is a convenient calculational framework for cross sections in terms of partial wave matrix elements, e.g. $\mathcal{S}_{njl,n'j'l'}(E)$.

The result of such an analysis gives, for incident particles in the elastic channel $|0kjl\rangle$, the asymptotic form of $u_{njl}(r)/r \equiv \psi_n^{jl}(r)$ as $r \to \infty$:

$$u_{nj'l'}(r) \to \frac{i}{2}\left(\delta_{ll'}\delta_{jj'}\delta_{n0}H_l^-(\eta,kr) - \mathcal{S}_{nj'l',0jl}(E_k)\sqrt{\frac{k}{k'}}\,H_l^+(\eta,k'r)\right), \tag{2.47}$$

where $H_l^{\pm}(\eta,z)$ are the outgoing and incoming Coulomb-Hankel functions, which span the solutions to the free Schrödinger equation, e.g. in which $V_{om} = 0$, and η is the Sommerfeld parameter, which is 0 for neutral particles (see Section A.1).

One may define the partial wave scattering amplitude for a plane wave $\mathbf{k}$

$$f(n'\mathbf{k}' \leftarrow n\mathbf{k}) \equiv -(2\pi)^2\mu\,\langle n'\mathbf{k}'\,|\,\mathcal{T}_{om}(E_k)\,|\,n\mathbf{k}\rangle\,, \tag{2.48}$$

such that the differential cross sections are formed by the contraction of the scattering amplitude matrix by the outgoing and incoming state vectors denoted, respectively, by $\xi_{n'}$ and ξ_n:

$$\frac{d\sigma}{d\Omega}(n'\mathbf{k}' \leftarrow \mathbf{k}n) = |\xi_{n'}f(n'\mathbf{k}' \leftarrow n\mathbf{k})\,\xi_n|^2\,. \tag{2.49}$$

The elastic cross section refers to $n = n' = 0$. The total elastic cross section is the integration of this quantity over solid angle $\Omega = (\theta,\phi)$. Here, $\theta = \mathbf{k}\cdot\mathbf{k}'$, and ϕ is the polar angle. The optical theorem, a result of unitarity, gives it as a function of the forward amplitude [162]:

$$\mathfrak{Im}f(n\mathbf{k} \leftarrow n\mathbf{k}) = \frac{\hbar k}{4\pi}\sigma^{nn}(\mathbf{k}). \tag{2.50}$$

Section A.1 provides these quantities, as well as the reaction cross section in terms of a partial wave expansion in orbital angular momentum, appropriate for a spin-1/2 nucleon incident on a spin-zero target.

2.3 Connecting to the compound nucleus

So far, we've been concerned with the on-shell properties of the propagators, and the resulting scattering matrices, which completely determines the scattering amplitudes and cross sections. Now, we turn our attention to the spectrum of eigenvalues of $\mathcal{H}_{\mathcal{QQ}}$ on the complex plane, and, subsequently, the analytic properties of the resulting off-shell poles in the corresponding scattering matrices. Specifically, we take inspiration from random matrix theory in treating this spectrum as a *distribution*, which we will use to establish the connection between $\mathcal{H}_{om}$ and the statistical de-excitation of the compound nucleus.

The $\mathcal{S}$-matrix is a meromorphic function in the complex energy plane; analytic everywhere except for a set of poles corresponding to eigenvalues z, $(\mathcal{H}_{\mathcal{QQ}} - z) = 0$, as well as a branch cut along the positive real axis, running through branch points at each threshold for emission of another particle; $0, S_n^A, S_n^{A-1}, \ldots$ on our energy scale [162]. It can be shown that the set of poles on the so-called physical energy sheet, with $\mathfrak{Im}k > 0$, correspond to spatially localized bound states. We call the poles on the unphysical sheet, with $\mathfrak{Im}k < 0$, resonances. When they are located close to the positive real axis, they may contribute to features in energy dependent cross-sections.

Near a pole on the unphysical sheet at complex energy $E = E_R - i\Gamma$, the most general form for the $\mathcal{S}$-matrix can be written (absorbing the momentum ratios into $\mathcal{S}$)[162]:

$$\mathcal{S}_{\alpha\alpha'} = \mathcal{S}^{bg} - i\frac{\gamma_{\alpha'}\gamma_{\alpha}}{E - E_R + i\Gamma}, \tag{2.51}$$

where $\mathcal{S}^{bg}$ is the background contribution. This gives rise to the multi-level Breit-Wigner parameterization, an expansion of the $\mathcal{S}$-matrix in terms of these poles:

$$\mathcal{S}_{\alpha'\alpha} = e^{i\phi_{\alpha'}} \left[\mathbb{1} - i \sum_{\beta} \frac{\Gamma_{\alpha\beta}\Gamma_{\alpha'\beta}}{E_\beta - E - \frac{1}{2}\Gamma_{\beta\beta}} \right] e^{i\phi_\alpha}. \tag{2.52}$$

Here, the matrices $\Gamma_{\alpha\beta}$ determine the widths and couplings of each resonance, and ϕ are the hard-sphere phase shifts (see Section A.1). This is a widely used formula for parametrizing resolvable resonances, and is related to the phenomenological R-matrix [40, 163].

In practice, measurements are taken with a wave packet with some energy width ΔE, not a plane wave. In the case $\Delta E \gg \Gamma$, rather than seeing an energy-dependent scattering feature, one sees the time-dependent process of the formation and decay of a virtual state with lifetime $\hbar/\Gamma$. This suggests the introduction of the energy-averaged optical potential:

$$V_{om}(E) \leftarrow V_{om}(E + i\Delta E). \tag{2.53}$$

This offset above the real line has the effect of, within the resolution of the experiment, making *all* resonances in the $\mathbb{Q}$-space — which live below the real line — broad and overlapping. In practice, the ΔE should be chosen so that the $\mathbb{P}$-space corresponds to states with lifetime $\tau \ll \hbar/\Delta E$, and vice-versa for the $\mathbb{Q}$-space. Thus, the offset ΔE, and it's resulting Hilbert-space partitioning, delimits between direct, short-lived reactions in $\mathbb{P}$, and long-lived compound nucleus (CN) states in the $\mathbb{Q}$-space. The common choice of $\mathbb{P}$-space corresponding to only the elastic channel is tantamount to a treatment of *all* non-elastic reactions as compound nucleus (CN) states, and smoothing over even experimentally resolvable resonances with a large ΔE.

For the treatment of CN phenomena with an OMP, we are thus considering the case of the *average* behavior of many overlapping resonances. It is thus useful to consider the distribution of these resonances in the complex plane as a statistical distribution. In particular, one considers the matrices Γ as *random matrices*, resulting from the asymptotic overlaps of eigenvectors of the random matrix $\mathcal{H}_{\mathcal{Q}\mathcal{Q}}$, which has E_α as eigenvalues. Specifically, these

matrices belong to the Gaussian orthogonal ensemble (GOE) [167, 80]. We will briefly review the schematics of this theory, and how it leads to, along with unitary on the entire Hilbert space; $\mathbb{P} \oplus \mathbb{Q}$, the factorization of the formation and decay amplitudes[4] for the CN, i.e., the Hauser-Feshbach formalism.

The energy averaging leads to an alternate definition of the $\mathcal{S}$-matrix, with a smoothly varying direct contribution and rapidly varying CN contribution:

$$\mathcal{S}_{\alpha\beta} = \langle \mathcal{S}_{\alpha\beta} \rangle + \hat{\mathcal{S}}_{\alpha\beta}. \tag{2.54}$$

Here $\langle f \rangle$ refers to the average of a quantity f over an energy region, and $\hat{f}$ refers to the standard deviation of the fluctuations. By unitarity of the $\mathcal{S}$-matrix, we can write

$$\begin{aligned} \delta_{\alpha\beta} &= \sum_{\gamma} \mathcal{S}_{\alpha\gamma} \mathcal{S}^{*}_{\beta\gamma} \\ &= \left\langle \sum_{\gamma} \mathcal{S}_{\alpha\gamma} \mathcal{S}^{*}_{\beta\gamma} \right\rangle + \sum_{\nu} \langle \mathcal{S}_{\alpha\nu} \rangle \langle \mathcal{S}_{\beta\nu} \rangle . \end{aligned} \tag{2.55}$$

The first term in Eq. 2.55 is the fluctuating CN contribution, and the second is direct, allowing us to write the generalized, or Satchler, transmission coefficient as

$$\begin{aligned} T_{\alpha\beta} &\equiv \left\langle \sum_{\gamma} \mathcal{S}_{\alpha\gamma} \mathcal{S}_{\beta\gamma} \right\rangle \\ &= \delta_{\alpha\beta} - \sum_{\gamma} \langle \mathcal{S}_{\alpha\gamma} \rangle \langle \mathcal{S}_{\beta\gamma} \rangle . \end{aligned} \tag{2.56}$$

We have used unitarity to relate the first and second moments of the $\mathcal{S}$-matrix, and defined $T_{\alpha\beta}$; a real number between 0 and 1, which determines the probability that, if a transition from channels α to β is observed, it proceeds through an intermediate CN. By comparison to Eq. 2.29, we see that the previously defined transmission coefficients are simply the diagonal elements of this matrix

[4] This factorization is a formal statement of the Bohr compound nucleus theory - in which the excitation energy is equilibrated over many degrees of freedom and the CN becomes "memoryless".

$$\mathbb{T}_\alpha = T_{\alpha\alpha}. \tag{2.57}$$

The cross section for such a transition reads:

$$\sigma_\alpha^{\text{rxn}} = \frac{\pi g_\alpha}{k_\alpha^2}\left(1 - |S_{\alpha\alpha}|^2\right) \tag{2.58}$$

$$= \frac{\pi g_\alpha}{k_\alpha^2}\mathbb{T}_\alpha. \tag{2.59}$$

We now derive the branching ratios for the decay of the CN in terms of the transmission coefficients. Consider the microscopic requirement of detailed balance for a cross section for a channel transition $\sigma_{\alpha\beta}$ and its time-reversed process:

$$\frac{k_\alpha^2}{g_\alpha}\sigma_{\alpha\beta} = \frac{k_\beta^2}{g_\beta}\sigma_{\beta\alpha}. \tag{2.60}$$

Here, g_β refers to spin-statistical factors for a channel β. We have used the fact that, neglecting width-fluctuation corrections, one can factorize a CN cross section into the reaction cross section through the entrance channel $\sigma_\alpha^{\text{rxn}}$ and the branching ratio to decay through exit channel β, Γ_β/Γ:

$$\begin{aligned}\sigma_{\alpha\beta} &= \sigma_\alpha^{\text{rxn}}\frac{\Gamma_\beta}{\Gamma} \\ &= T_\alpha\frac{\pi g_\alpha}{k_\alpha^2}\frac{\Gamma_\beta}{\Gamma}.\end{aligned} \tag{2.61}$$

Here, we have used the definition of the reaction cross section as in Eq. 2.58. By combining Eq. 2.60 with Eq. 2.59, we immediately find

$$\frac{\mathbb{T}_\alpha\Gamma_\beta}{\Gamma} = \frac{\mathbb{T}_\beta\Gamma_\alpha}{\Gamma}, \tag{2.62}$$

We have shown that transmission coefficients and branching ratios are identical up to

normalization, and we can immediately write the branching ratios for decay into a given channel in terms of these transmission coefficients:

$$\begin{aligned} p(\beta) &= \frac{\Gamma_\beta}{\Gamma} \\ &= \frac{T_\beta}{\sum_\nu T_\nu}, \end{aligned} \tag{2.63}$$

where the sum in the denominator runs over all open channels that respect the symmetries of the system. Eq. 2.63 can also include photon emission in full competition with neutrons, with $\mathcal{T}_\beta$ also representing the photon transmission coefficient, e.g. as calculated according to giant resonance parameters. For the case of neutron evaporation, the probability of a given initial CN decaying through a given channel β is the fractional width given in Eq. 2.63.

We have the formula for the probability for the compound nucleus to de-excite through a decay channel, corresponding to neutron emission with energy E in COM-frame, consisting of an excited residual core with energy E_n^A, such that $E_n^A = E_m^{A+1} - E - S_n^{A+1}$. Where we do not have information on individual discrete levels, we turn the sum in Eq. 2.63, which is over channels n with definite COM-frame energy E_n, into an integral with measure $dE'_n = \rho(E_0 - E_n - S_n, n)dE'$, which defines the level density $\rho(E, \alpha)$. This leads us to the fractional width for neutron evaporation:

$$p(E, j, I_n, \pi_n) = \frac{\mathbb{T}_{jl}^{I_n \pi_n}(E)\, \rho_{jl}^{I_n \pi_n}(E_m^{A+1} - E_n^A - S_n^{A+1})}{\sum_{j' I' \pi'} \int dE'_n\ \mathbb{T}_{j'l'}^{I'\pi'}(E')\, \rho_{j'l'}^{I'\pi'}(E_m^{A+1} - E_n^A - S_n^{A+1})}. \tag{2.64}$$

Eq. 2.64 is the central result of the Hauser-Feshbach theory, and is used to model the emission of neutrons from an excited CN. Here, the superscript $I\pi$ implies the limitation to states jl in the subscript that satisfy the triangle relation Eq. 2.8, and conserve parity. Resolved discrete excited states of the residual core may be included by keeping them in a discrete sum. In practice, the continuum is discretized into uncoupled bins.

One can use Eq. 2.64 to model the decay chain of compound nuclei. Decay by nucleon

emission requires as ingredients only the level density of the residual core, and the OMP which describes the effective interaction between the residual core and the emitted nucleon. Generalized optical potentials between clusters of nucleons (e.g. between a nucleus and an α-particle), straightforwardly extend this framework to include emission of clusters. As mentioned, photon emission may also be included by extending the definition of $\mathbb{T}_{jl}^{I\pi}(E)$ using photon strength functions.

In this way, given an initial nucleus with well-determined excitation energy, spin and parity, one can compute the probability to decay via a specific mode, to a residual nucleus with another excitation energy, spin and parity, and an emitted species of radiation. In fact, the probability in Eq. 2.64 defines a Markov process, in which the current state of the system (e.g. A, Z, E, J, π) solely determines its probability of evolving to the next state. By sampling from this probability, one can generate an ensemble of *histories*, each specifying a trajectory of de-excitation, beginning with an initial excited nucleus, and ending in a stable (or long-lived) state. From many such histories, one can reconstruct experimental observables relating to the emitted radiation, including full correlations between energy, angle, multiplicity and species, as well as with the remaining stable or long-lived nuclei that are produced. This is called the Monte Carlo Hauser-Feshbach (MCHF) formalism, and we discuss it in more detail in the context of our study of fission in Chapter 3. First, however, we provide the necessary discussion of how, in practice, to calculate and use the optical potential, paying attention to, how, in particular, the optical potentials studied in this work were determined.

2.4 Calculating the optical potential

We have now developed the formal theory of the optical potential, and connected it to direct and compound reaction observables. In this section we elucidate how to practically make use of the optical potential, describing the two optical potentials used in this work:

KDUQ [139] and WLH [178]. We pay particular attention to the respective approximations they require, and the common functional form they take. We first describe the common features of both potentials in the context of our developed formalism.

To calculate the optical potential exactly, one would need the same information as to calculate the (non-truncated) matrix of coupling potentials $V_{n'n}^{j'l',jl}$, that is to say, each of the infinite number of A-body states $|\Psi_n^A\rangle$, as well as realistic nucleon-nucleon forces. In practice, V_{om} is often parameterized phenomenologically. It can in principle be calculated microscopically using one of a variety of ab-initio many-body schemes, however the reach of these is currently limited to light nuclei. Alternatively, one can access the entire nuclear chart by applying many-body schemes in nuclear matter, and folding to nuclear density distributions in finite nuclei, as in the WLH potential or the semi-microscopic Jeukenne-Lejeune-Mahaux-Bruyéres (JLMB) potential [178, 9].

For practical reasons, often an approximate local optical potential is used. Perey and Buck developed the idea of the local equivalent potential, which produces the same asymptotic wavefunctions outside the range of the potential, and therefore the same scattering matrices, as the non-local potential, at the cost of gaining additional energy dependence [137]. This is discussed in detail from a nuclear matter perspective in [90]. Accordingly, one can write the non-local $V_{om}(\mathbf{k}, E)$, which is on-shell when $E = E_k = \hbar^2 k^2/2\mu$ by taking a Fourier transform from coordinate space $V_{om}(\mathbf{r} - \mathbf{r}', E)$. Then, the ratio of the effective mass $m^\star$ to the actual nucleon mass m is defined as

$$\frac{m_k}{m} = \left(1 + \frac{m}{k}\left[\frac{\partial}{\partial k}\mathfrak{Re}V_{om}(k, E)\right]_{E=E_k}\right)^{-1} \tag{2.65}$$

$$\frac{m_E}{m} = 1 - \left[\frac{\partial}{\partial E}\mathfrak{Re}V_{om}(k, E)\right]_{E=E_k} \tag{2.66}$$

$$\frac{m^\star}{m} \equiv 1 - \frac{k}{m}\frac{dk}{dE_k} = \frac{m_k}{m}\frac{m_E}{m} \tag{2.67}$$

This effective mass ratio occurs due to the dressing of the bare nucleon mass with its

effective self-interaction, V_{om}. It is empirically ~ 0.7 in nuclear matter [90]. m_k describes the contribution due to the non-locality, while m_E describes the contribution due to dynamic coupling to the $\mathbb{Q}$-space. Nuclear matter studies have been effective in informing the energy dependence for phenomenological optical potentials. We return to this in Chapter 4.

A downside to using a local optical potential is that the interior part of the wavefunction for a non-local and local-equivalent potential will not necessarily be the same, which impacts distorted-wave Born approximation and coupled-channels calculations that use local potentials. This extra energy dependence also prevents the use of the dispersion relation connecting states above and below the Fermi-energy [53].

Another common approximation is to take the $\mathbb{P}$-space as simply the elastic channel, in which the residual A-body core is in its ground state $|\psi_0^A\rangle$. This corresponds to the entrance channel for a typical scattering experiment. In fact, when excited states are added to $\mathbb{P}$, V_{om} is sometimes then referred to as the generalized optical potential [57]. Both optical potentials studied in this thesis take the $\mathbb{P}$-space as the elastic channel: $\mathbb{P} \equiv \{|\Psi_0^A\rangle\}$. Both potentials studied in this thesis attempt to construct this exact form of V_{om} through very different approaches.

Both OMPs studied in this work are local in coordinate space. The radial part of the Schrödinger-like scattering equation $(\mathcal{H}_{om} - E) = 0$, with a local potential optical potential, acts on the (reduced) wavefunctions $\frac{1}{r}u_{jl}(r) \equiv \psi_0^{jl}(r) \equiv \langle r|0kjl\rangle$. It is written as

$$\Big(-\frac{d^2}{dr^2}+\frac{l(l+1)}{r^2} + \frac{2\eta k}{r} + \frac{2\mu}{\hbar^2}V_{om}(r;\boldsymbol{\omega}) - k^2\Big)u_{jl}(r) = 0. \tag{2.68}$$

For a charged system, the Coulomb interaction potential is characterized by the Sommerfeld parameter, which is defined $\eta \equiv Z_1 Z_2 e^2 \mu/\hbar^2 k$, with charges Z_1 and Z_2 for the projectile and target. For neutral projectiles, $\eta = 0$. The optical potential $V_{om}(r;\boldsymbol{\omega})$ is a function of a set of parameters $\boldsymbol{\omega}$.

Both optical potentials include real and complex volume, surface, and spin-orbit terms, each with strength, V, radius, R, and diffuseness, a:

$$
\begin{aligned}
V(r;\boldsymbol{\omega},jl) = & -V_v f(r,R_v,a_v) \\
& -iW_v f(r,R_w,a_w) \\
& -i4a_d W_d \frac{d}{dr} f(r,R_d,a_d) \\
& +2\mathbf{l}\cdot\mathbf{s}\left(V_{so}+iW_{so}\right)\left(\frac{\hbar}{m_\pi c}\right)^2 \frac{1}{r}\frac{d}{dr} f(R_{so},a_{so}).
\end{aligned} \tag{2.69}
$$

The Woods-Saxon function is defined as

$$
f(r,R,a) \equiv \left[1+\exp\left(\frac{r-R}{a}\right)\right]^{-1}. \tag{2.70}
$$

For the spin-orbit part, we considering spin-zero targets with spin-1/2 projectiles. The coupling can then only take the values:

$$
2l\cdot s = \begin{cases} l & \text{if } j = l+\frac{1}{2} \\ -(l+1) & \text{if } j = l-\frac{1}{2} \end{cases}. \tag{2.71}
$$

The scale factor associated with the spin-orbit term uses the pion mass m_π such that $\left(\frac{\hbar}{m_\pi c}\right)^2 \approx 2$ fm^2 [163]. In general, for the global optical potentials, a set of sub-parameters determine the functional dependence of the depths, radii, and diffuseness of each term as a function of the energy, A and Z.

This is an extremely common form used and refined by optical potential practitioners, and has been able to produce very good agreement with experiment [81]. Both optical potentials studied in this work use the same general form, each employing some physically-motivated functional form for the depth, radii and diffusenesses of each term in Eq. 2.69 as a function of A, Z, and E. Each global OMP is thus exactly specified by the set of parameters that determine the functional dependence of each term's depth, radius and diffuseness as a function of A, Z and E. In this work, we deal with uncertainty-quantified optical potentials,

which are instead equipped with a multivariate distribution of those parameters.

Of particular importance are the parameters that determine how the V_{om} changes away from stability. Depth terms that can be separated into isoscalar and isovector components are said to take the Lane form [101, 102]. This form arises from simple considerations. Effective nucleon-nucleon forces contain terms which are dependent on the isospin projection of the two nucleons, $\mathbf{t}_1 \cdot \mathbf{t}_2$. This is true phenomenologically, for forces fit to nucleon-nucleon scattering and bound states of ^2H (e.g. [182]). In the case of the chiral forces, such as those which determine the WLH potential, they arise naturally from exchange of mesons, the effective force carriers for low-energy quantum chromodynamics (QCD) [114].

By averaging the isospin-projection terms in the 2-body nucleon forces V_{ij} over the nucleons in the target, as in Eqs. 2.26 and 2.30, one finds both the static and dynamic optical potential depths have terms which are dependent on the target-projectile isospin projection, $\mathbf{T} \cdot \mathbf{t}$. Accordingly, we adopt a form for each depth term that is broken into isoscalar and isovector terms, respectively, V_0 and V_1, which are independent of N and Z independently, but not necessarily to A:

$$V = V_0 + (\mathbf{T} \cdot \mathbf{t}) V_1. \tag{2.72}$$

This form leads us to

$$V_{n/p} = V_0 \pm \frac{\delta}{4} V_1, \tag{2.73}$$

where $\delta = \frac{N-Z}{N+Z}$, and the appropriate Clebsch-Gordan coefficients have been used. Here, the $+(-)$ signs are for neutrons(protons). This formalism naturally accounts for isospin mixing in nucleon-nucleus reactions, as is observed in quasi-elastic (p,n) reactions to isobaric analogue states.

In practice, it is difficult to determine a useful form that is truly Lane-consistent, primarily due to the breaking of isospin symmetry by the Coulomb interaction. Both optical

potentials studied in this work use a weaker form in which $V_{n/p} \neq V_0 \pm \frac{\delta}{4} V_1$. Instead, global neutron and proton optical potentials are fit with some parameters remaining consistent and others separate. The Lane form typically used is then is still as in Eq. 2.72, where V_0 and V_1 depend only on mass and energy, and now V_0 and V_1 may not be the same for neutrons and protons. Phenomenologically, V_1 should be negative, reflecting the fact that neutrons are less bound in neutron-rich systems than in proton-rich systems (and vice-versa for protons), and should decrease monotonically with energy [95].

The δ dependent depth terms V_1 are expected to be generally energy dependent, following the same considerations as the full optical reduction, Section 2.1. In phenomenological models they are only constrained by stable isotopes corresponding to a rather narrow range of δ. In particular, the imaginary surface component of the optical potential is peaked at low energies, reflecting that low-energy neutrons are preferentially absorbed, and emitted, from the fringe regions of the nucleus, where nucleon density, and, therefore, Pauli blocking effects, are diminished relative to the interior [124]. Understanding the isovector dependence of this low-energy imaginary surface strength is essential for understanding low-energy compound-nuclear processes involving isotopes away from β-stability, such as in fission or the r-process.

In fact, it has been shown that the isovector components of OMPs are poorly constrained in the low energy (100s of keV) region, with strength functions suggesting a suppression of neutron-capture strength in the neutron-rich region, and simulations predicting a strong sensitivity of r-process reaction rates to the isovector dependence, especially for drip-line nuclei [71]. Moreover, the symmetry energy of nuclear matter, as well as its first-order density dependence about saturation density, is contained in the energy dependence and isovector component of the single-nucleon self-energy [183]. It is clear that understanding how optical potentials change away from stability is tantamount to providing stricter constraints, phenomenologically or microscopically, on the isovector dependence of the various depth parameters contained in Eq. 2.69.

Finally, we turn our attention to the two optical potentials we study in this work, paying specific attention to how they determine their isovector dependence.

2.4.1 KDUQ

The phenomenological OMP tested in this thesis was KDUQ [139], fit to differential elastic scattering cross sections and analyzing powers, proton reaction cross sections, and neutron total cross sections. This is an uncertainty-quantified version of the workhorse phenomenological OMP Koning-Delaroche [95], which updates the original potential using robust outlier rejection and Bayesian calibration. The original potential is valid for 1 keV up to 200 MeV, for (near-) spherical nuclides in the mass range $24 \leq A \leq 209$. The default parameterization of Koning-Delaroche, as provided in [95], is the default OMP in `CGMF`. The set of parameters and functional forms for each terms depth, radius, and diffuseness are listed in [95]. An approximate Lane-consistency is achieved by forcing certain isovector depth parameters to be consistent between the neutron and proton potentials.

We now review the Bayesian framework used in calibrating KDUQ. The Bayesian calibration of the optical potential Eq. 2.69 refers to finding the conditional probability for a set of parameters, $\boldsymbol{\omega}$, given a set of physical observations, y. The statistical model relating the observations and the optical potential (OP) is of the form

$$y = \mathrm{OP}(\boldsymbol{\omega}) + \boldsymbol{\varepsilon}, \tag{2.74}$$

where $\mathrm{OP}(\boldsymbol{\omega})$ represents the set of observables — differential and angle-integrated cross sections, analyzing powers — that were calculated from the optical model. $\boldsymbol{\varepsilon} \sim \mathrm{N}(\mathbf{0}, \boldsymbol{\Sigma})$ is the residual error, which was assume follows a multivariate Gaussian distribution with mean $\mathbf{0}$ and covariance matrix $\boldsymbol{\Sigma}$.

The Bayesian calibration refers to the identification of the conditional probability density $p(\boldsymbol{\omega}|y)$, referred to as the *posterior* of $\boldsymbol{\omega}$. Given $p(\boldsymbol{\omega})$, the *prior* of $\boldsymbol{\omega}$, the posterior is found

via applying Bayes' theorem, i.e.,

$$p(\boldsymbol{\omega}|y) = \frac{p(y|\boldsymbol{\omega})p(\boldsymbol{\omega})}{p(y)} \propto p(y|\boldsymbol{\omega})p(\boldsymbol{\omega}), \tag{2.75}$$

The conditional probability density $p(y|\boldsymbol{\omega})$ is called the *likelihood* function, which provides a metric for comparing $\mathrm{OP}(\boldsymbol{\omega})$ with the physical observations y. In a typical case, with a single observable, the likelihood is constructed as

$$p(y|\boldsymbol{\omega}) \propto |\boldsymbol{\Sigma}|^{-\frac{1}{2}} \exp\left\{-\frac{1}{2}(y - \mathrm{OP}(\boldsymbol{\omega}))^{\mathsf{T}}\boldsymbol{\Sigma}^{-1}(y - \mathrm{OP}(\boldsymbol{\omega}))\right\}. \tag{2.76}$$

Once the posterior is specified, one can build the *predictive posterior* distribution of new unobserved data y^{pred}, given the already observed data, by marginalizing over the model parameters $\boldsymbol{\omega}$:

$$p(y^{\mathrm{pred}}|y) = \int p(y^{\mathrm{pred}}|\boldsymbol{\omega})p(\boldsymbol{\omega}|y)\mathrm{d}\boldsymbol{\omega}. \tag{2.77}$$

This predictive posterior folds together the uncertainty on our model parameters coming from the posterior $p(\boldsymbol{\omega}|y)$ Eq. 2.75, with the expected intrinsic error of new gathered data for a given model parameter $p(y^{\mathrm{pred}}|\boldsymbol{\omega})$.

Markov chain Monte Carlo (MCMC) [62], e.g., the Metropolis-Hastings algorithm, is commonly used to sample from Eq. 2.75. In each iteration, the likelihood function in Eq. 2.76 is evaluated at a different value of $\boldsymbol{\omega}$. This is tantamount to numerically solving Eq. 5.3 for each partial wave until convergence, and then reconstructing a given observable as in Section A.1. In the case of KDUQ, the affine invariant Goodman-Weare sampling algorithm was used [67].

In the case of fitting an OMP to a large corpus of experimental observables, as with KDUQ, one has choices in how to weight different observables, or different experiments, in the likelihood. In [139], two different strategies are taken, denoted the "democratic" and

the "federal". In the democratic ansatz, the data covariance in the likelihood function is assumed to be diagonal, the experimentally reported uncertainties for each data point are augmented with an unreported uncertainty (estimated in an observable-by-observable basis) and the covariance is scaled by k/N, k being the number of model parameters (46), and N being the total number of data points. In the federal ansatz, the data covariance is modified so that data points of observable i are scaled separately by the number of data points belonging to that observable, e.g., by k/N_i. Thus, each observable has equal influence in the likelihood, and each data point has equal influence within its observable. In [139], the two ansatze produced similar calibrated models, and the federal ansatz is used in this work.

2.4.2 WLH

The other optical potential examined in this thesis is the microscopic WLH potential, which was developed in a nuclear matter folding approach [178]. First, in asymmetric nuclear matter, at a variety of densities and asymmetry parameters δ, the single-nucleon self-energy was calculated self-consistently to 2^{nd} order in many-body perturbation theory (MBPT). The advantage of this approach is there is no restriction to the line of stability: the self-energy was calculated for a much wider range of asymmetries than is possible in phenomenological models like KDUQ. Additionally, the self-energy was calculated using nucleon-nucleon forces from chiral effective field theory (χ-EFT), therefore maintaining consistency with QCD. In particular, chiral nuclear forces were employed at next-to-next-to-leading order (N2LO) and N3LO in the chiral expansion. Different choices for the cutoff of the regulator function that suppresses high momentum states were employed.

To apply these nuclear matter self-energies to finite nuclei, they are then folded to nuclear density distributions using the improved local density approximation (I-LDA) to produce optical potentials. The nucleon densities are calculated in mean-field theory with Skyrme effective interactions [106]. The underlying theoretical uncertainty was

approximated by the spread in resulting parameters from five different choices of chiral interaction. The WLH spin-orbit term was developed using a density-matrix expansion at the Hartree-Fock level [85].

The targets considered spanned 1800 nuclei, ranging in mass from $12 < A < 242$, inclusive of light and medium-mass bound isotopes out to the neutron drip line. The energy considered was $E \in [0, 200]$ MeV.

For target nuclei with small proton-neutron asymmetry, the WLH isospin-dependence follows the Lane form with first-order δ dependence, however, for nuclei with larger isospin asymmetries, the WLH potential contains terms with no parallel in KDUQ, which are proportional to the square of the isospin asymmetry, and strongest at low energy. Understanding the phenomenological implications of these higher order terms is especially interesting for neutron-rich nuclei.

Chapter 3

Uncertainty Quantification of Fission Observables

It is the goal of the work presented in this chapter to determine, to what degree, measurements of the prompt emissions provide constraints on the nucleon-nucleus interaction between the residual fragments and their neutron progeny. We investigate this dependence for the first time by propagating two uncertainty-quantified optical model potential (OMP)s through Monte Carlo Hauser-Feshbach (MCHF) fission fragment de-excitation with the CGMF code, and constructing credible distributions for a variety of fission observables. These distributions represent the uncertainty of a given fission observable, due to the parametric uncertainty in an OMP.

To begin, we briefly review the theory of nuclear fission and the subsequent fragment de-excitation. We discuss the modeling of the de-excitation in the Monte Carlo Hauser-Feshbach (MCHF) formalism introduced in Chapter 2, and clarify the role played by the OMP. We describe the current corpus of experimental fission observables, and how to extract those observables from a MCHF calculation.

Next, we state the methodology used for quantifying the uncertainty in these observ-

ables due to the OMP in the MCHF code CGMF in this work. Finally, we show the results of this uncertainty quantification, using the Koning-Delaroche uncertainty quantified (KDUQ) and Whitehead-Lim-Holt (WLH) potentials, comparing to a variety of experiments and discussing the results.

3.1 Nuclear fission and the optical potential

Nuclear fission has been a subject of study since its discovery by Lise Meitner and Otto Frisch in the experimental results of Otto Hahn in 1938. The phenomenon, in which a fissile nuclide - typically an actinide - deforms into an unstable configuration which splits into (typically) two fragments, produces a variety of correlated observables, and spans many orders of magnitude in time.

Historically, efforts to calibrate phenomenological optical potential parameters have relied on elastic scattering experiments. The corpora of experimental data typically include include neutron and proton differential elastic scattering cross sections, $d\sigma/d\Omega$, and total and reaction cross sections, σ_t and σ_{rxn}, respectively. Current work has focused on propagating OMP uncertainties into specific non-elastic reaction channels, such as transfer, charge-exchange and knockout reactions, with the goal of eventually including non-elastic measurements as OMP constraints in the form of Bayesian posteriors for model calibration [179, 77].

In this chapter, we examine the efficacy of expanding this corpus to include compound nucleus (CN) observables in which unstable nuclei are produced, directly into the calibration posterior. Specifically, we focus on observables from fission. This has several potential advantages:

1. measurements of fission fragments and their prompt emissions provide experimental access to unstable nuclei, thereby testing the extrapolations of global OMPs from stability,

2. the energy scale of prompt neutron emissions is typically closer to astrophysically relevant energies than direct reactions in beam-line experiments,

3. and there already exists a large library of historical experimental data for fission-fragment decay spectroscopy, including multi-species correlations

It is also worth noting that CN processes already contaminate elastic scattering measurements at low incident nucleon energy, where compound-elastic processes dominate the cross sections. In one way or another, all phenomenological OMPs that extend to low energies must address this in the calibration. Due to computational limitations, the approximation may be adopted to pre-calculate the CN-elastic cross section with a Hauser-Feshbach (HF) treatment, using a single set of OMP parameters from the prior; that is, the CN-elastic component is typically not adjusted with the calibration [139]. Further, the presence of resolved resonances complicates the energy averaging in practice, making statistical assumptions invalid.

Directly incorporating CN observables, including fission, potentially provides new constraints for phenomenological OMPs at low-energy, that may be under constrained currently. The sensitivity of CN reaction formalisms to model inputs has been tested in the past; for example, for mass-yield models [89, 107], and non-statistical properties [91] in fission, and for level densities in fusion [169].

It is a computationally demanding task to simultaneously quantify uncertainty and correlations between all model inputs for every CN observable of interest. The piecemeal efforts so far have indicated strong sensitivity to level densities, and cases where results disagree significantly with experiment [169]. This indicates the potential efficacy of optimizing model inputs — level densities, OMPs, strength functions, etc. — to CN observables. Indeed,level densities have previously been extracted from neutron evaporation spectra, [173, 143]. It has been suggested that uncertainties in CN observables due to the OMP may be larger than for level densities in some cases; particularly at low energy [139]. Therefore, we take the first steps here to quantify this uncertainty in fission.

Due to the interesting, still not fully understood, physical phenomena associated with fission, and the importance of the reaction to society, it has been subject to extensive measurement and modeling (For an exhaustive review see [159, 151] and references therein). There is, in particular, a rich history of experiments investigating the properties and correlations between the prompt emissions in fission going back at least six decades [150, 116, 132, 180, 82, 60, 24]. Measured observables include the energy and multiplicity of neutrons and photons, and the correlations between them and the fragments themselves.

The observables we consider in this work in particular are the prompt neutrons emitted from the fragments as the de-excite. These signals are correlated with the excitation energy and angular momentum of the fragments following scission as well as the branching ratios for de-excitation. In particular, experiments that measure these neutron fragment correlations [68, 69, 24, 21] require finesse. These experiments are able to approximately reconstruct the center-of-mass frame neutron spectrum by measuring the fragment mass and energy in an Frisch-grid ion chamber in correlations with neutron energies measured by the time-of-flight method in scintillator detectors.

The pre-emission fragment states cannot be directly measured, and the effect of the dependence on the de-excitation model on the reconstructions of the pre-fragment state must be well understood to use experiments to probe open questions about excitation energy and angular momentum sharing in fission [180]. Specifically, it has been observed that OMP predictions of the angular momentum removed by emitted neutron goes against the commonly held belief that fission neutrons are roughly isotropic in the center-of-mass (COM) frame [155].

The fragments produced in fission are neutron-rich and highly excited; born into a state dependent on the conserved quantities (mass, charge, angular momentum, excitation energy, etc.) of the pre-scission CN, its deformation at the saddle point, and the dynamics of scission. It then equilibrates its excess deformation energy into excitation energy, and typically de-excites by promptly emitting neutrons until reaching the neutron removal

threshold. Below the threshold, if still excitation energy dominated, they emit statistical γ-rays. Finally, near the Yrast line, they become angular-momentum dominated by the strong coupling to discrete rotational states. They then emit discrete γ-rays corresponding to the remaining transitions to a stable or long-lived state. Typically, this state is still unstable to β-decay, and further delayed neutron and γ-emission are required before a stable state is reached.

In the MCHF formalism, as discussed in Chapter 2, the optical potential represents the effective interaction between the removed nucleon and the excited residual core. The truncation of the $\mathbb{P}$-space of the OMP to the elastic channel represents one of the most dramatic approximations in modeling many nuclear reactions, including neutron emission from fission fragments. Fission fragments are not generally spherical in their ground state, and even those that are, are expected to have low-lying collective vibrational or rotational/vibrational states. In particular, even-even nuclei with $A < 150$ tend to be more spherical with a spectrum well described by vibrational states, while heavier nuclei are more likely to be deformed in the ground state and exhibit rotational structure [16]. These low-lying states couple to the ground-state and each other, but, importantly, also couple to the $\mathbb{Q}$-space, acting as doorway states to more complicated compound configurations.

These low-lying collective states can be measured in stable even-even nuclei, and calibrating a phenomenological generalized optical potential using collective models for excited states in the $\mathbb{P}$-space well describes scattering data [161]. However, for odd-A nuclei the competition between vibrational and single particle states makes measurement and modeling of low-lying collective states more difficult; moreover, many fission fragments aren't stable enough for measurements anyway.

Promising work has connected microscopic models of collective excited states (e.g. the quasi-particle random phase approximation (QRPA)) to scattering using a folding model, e.g. [50], but this method has not yet realized a global model that is able to make predictions in experimentally inaccessible regions of the nuclear chart. Due to the current

lack of such a global model, what is typically done is to approximate fission fragments as spherical with negligible coupling to low-lying states, as in a single-channel OMP. Thus, we relegate the collective excited states to the $\mathbb{Q}$-space, where they are treated on average as virtual contributions.

3.2 Uncertainty propagation

CGMF [160] is a MCHF code which generates initial configurations for the fission fragments in mass, charge, kinetic energy, excitation energy, spin, and parity, and then samples their de-excitation trajectories by emission of neutrons and γ-rays. It is capable of neutron induced fission on various actinides over incident energies ranging from thermal to 20MeV, as well as spontaneous fission of relevant isotopes.

CGMF samples the initial post-scission fragment masses using a three-Gaussian model with linearl and exponential terms in the energy dependence of both the first and second moments. The energy dependence is tuned to experimental data. The fragment charges are then sampled conditional on the masses using the Wahl systematics [172], and the total kinetic energy (TKE) of the fragments are sampled from empirical distributions when possible, and a Gaussian using a mass-dependent mean and standard deviation tuned to available data otherwise. The total excitation energy (TXE) is then available by energy balance; TXE = $\mathrm{Q_f}$ − TKE, where Q_f is the energy liberated in the fission, depending on the binding energies of the pair of fission fragments created. The partitioning of the excitation energy is done in the Fermi-gas model, in which the temperature ratio of the light to heavy fragment is allowed to be mass dependent, and tuned to prompt neutron properties. The fragment spins are uncorrelated, and chosen from Gaussians centered on the number of geometric levels $J(J+1)$, with width tuned to prompt photon properties. Parity states are assumed to be equiprobable.

Once the post-scission states of the two fission fragments for a history have been sampled,

they are then de-excited in the MCHF formalism, where the decay of the CN is treated as a Markov process, governed by Eq. 2.64, with neutron and photon emission in full competition. The MCHF algorithm, given the conserved quantum numbers of the fully-accelerated post-scission fragment, samples from Eq. 2.64, emitting neutrons and photons until a state is reached that is stable against prompt emissions. The observables are then re-constructed event-by-event.

The nuclear level density is modeled using the Kawano-Chiba-Koura (KCK) systematics, which extends the Gilbert-Cameron model to include an energy dependent level density parameter, and defines the procedure for assigning spin and parity to discrete levels for which it is unknown [92]. This assumption is another potentially large contributor of uncertainty, as level densities are plagued by the same issue as OMPs of extrapolating away from stability, where data is available, but this is not considered here.

It is important to note that certain model inputs (e.g. nuclear temperatures used for excitation energy sharing) in CGMF have been tuned to experimental observables, especially mean neutron multiplicities. This tuning was performed using the default Koning-Delaroche (KD) OMP parameterization, so correlations between these parameters and OMP parameters may be responsible for canceling errors in both. This point will be emphasized in the interpretation of the results.

The fission reactions under consideration were ^{252}Cf (sf) and ^{235}U (n_{th},f). For each of these cases, the uncertainty propagation was done by brute force, with 300 samples from the posterior predictive distributions of each OMP. In this case of WLH, these samples were generated by assuming a multi-variate normal distribution and sampling from the covariance provided in [178]. It should be noted that, although the posterior distributions for WLH are expected to be well approximated by a multi-variate normal, this approximation may lead to a slightly higher proportion of samples drawn from the tails of the distribution. For the case of KDUQ, these samples were taken from the supplemental material of [139], using the federal posterior formulation. For each OMP sample, an ensemble of one million

Monte Carlo histories were generated, from which first and second moments of aggregate observables were re-constructed to compare to experiment.

Some experimental comparisons required kinematic correction for COM-frame prompt fission neutron spectrum (PFNS). In particular, as described in [68], only neutrons with lab-frame energy larger than the pre-emission kinetic energy per nucleon of the emitting fragment were measured. For comparison to this experiment, these cuts were applied event-by-event to the generated histories. A similar cut to compare to data from [21] was determined to have a negligible effect when applied to CGMF histories, and was subsequently ignored. Additionally, mass reconstruction in the relevant experiments has an uncertainty with a standard deviation of roughly 2-4 mass units.

The spread of the mean in each observable over all parameter samples reflects the sum of two uncertainties: the intrinsic parametric uncertainty of each OMP, and the inherent uncertainty due to the limited number of Monte Carlo histories per parameter sample. These uncertainties are assumed to be uncorrelated, so that the total uncertainty σ_t across the ensemble of OMP samples was taken as the quadrature sum of the MCHF uncertainty and the parametric uncertainty of the OMP; so that the latter was estimated as:

$$\sigma_{omp} = \sqrt{\sigma_t^2 - \sigma_{mc}^2}. \tag{3.1}$$

For a given ensemble of histories corresponding to OMP parameter sample i, a Monte Carlo uncertainty σ_{mc}^i was calculated for each observable. For observables that correspond to the mean of a distribution over events (e.g. average prompt neutron multiplicity $\bar{\nu}$), σ_{mc}^i corresponded to the standard error in the mean (SEM), and was estimated directly from the second moment of the distribution of the observable over all histories in the ensemble, by applying the Central Limit Theorem (CLT):

$$\sigma_{mc}^i = \sqrt{\frac{1}{N}\sum_n (k_n^i)^2 - \frac{1}{N^2}\left(\sum_n k_n^i\right)^2}, \tag{3.2}$$

where k_n^i represents the score for the observable of interest in the nth (out of N) histories of the ith sample.

Observables corresponding to distributions (e.g. PFNS), were constructed by histogramming over ensemble histories, in which case the mean of an observable in a bin corresponded to the probability density of k_n^i falling into that bin in a given history. For m times out of N histories in a bin in phase space with width Δx, the mean is $m/(N\Delta x)$. In this case, σ_{mc}^i was estimated in each histogram bin according to a Binomial distribution:

$$\sigma_{mc}^i = \frac{1}{N\Delta X}\sqrt{1-\frac{m}{N}}. \tag{3.3}$$

In either case, σ_{mc} for the observable was then estimated by averaging σ_{mc}^i over all ensembles.

The propagation of uncertainties through `CGMF` was a significant computational task. Calculating fission observables for a single parameter sample (consisting of one million `CGMF` histories) required roughly 30 cpu-hours on the Great Lakes cluster at the University of Michigan, using Intel(R) Xeon(R) Gold 6140 CPUs. The 300 samples required to generate a posterior predictive distribution of observables corresponding to a single potential and fissioning system therefore each required roughly 9300 cpu-hours, or just over 1 cpu-year, and each produced over 300 Gb of history files on disk, after compression.

Within a given ensemble, histories were ran in parallel using the Message Passing Interface (MPI) implementation in the python module MPI for Python (`mpi4py`) [59, 38]. A modified version of `CGMF` was used with `Python` bindings, and all software used to run `CGMF` and analyze results is open-source and available online under the name `omp-uq`. The technology and dependency stack is also open source, and, insofar as possible, managed automatically by `CMake` and `git` submodules, to maximize ease of installation and cross-platform compatibility. The stack includes, as a dependency to the aforementioned fork of `CGMF`, an open-source code for uncertainty-quantification in few-body reaction calculations by the authors called `Optical model ScatterIng & ReactIon Software (OSIRIS)` [14].

OSIRIS accepts as input a set of global optical potential parameters, including for KDUQ and WLH, (e.g. in a `json` file according to the format used by the TOMFOOL code [139] which was used to calculate KDUQ), and calculates potential values and scattering amplitudes. Insofar as was possible, all components in the software stack created by the authors employ unit and regression testing using `pytest` [97] and `Catch2` [86].

3.3 Results

Figure 3.1 displays histograms of $\bar{\nu}$, the mean prompt neutron multiplicities per fission event (inclusive of both fragments). In each of these cases, the Monte Carlo uncertainty in each ensemble was negligible compared to the parametric uncertainty of each OMP, and are therefore not shown. For comparison are a variety of experimental results and evaluations of $\bar{\nu}$. Interestingly, each OMP disagreed with each other to statistical significance, with KDUQ generally being the closest to experiment. WLH universally predicted too large of multiplicities.

This can be interpreted from an energy budget perspective, as shown below (see Fig. 3.2 for example), the WLH optical potential produces softer spectra. For a given initial excitation energy, less energy removed per neutron implies a larger multiplicity.

In all other figures, the shaded regions represent a credible interval of two standard deviations for each OMP, with the colored regions representing the portion of the uncertainty attributable to the OMP parameters, and the grey region due to the Monte-Carlo treatment. Thus, the total shaded regions in the figures represent σ_t, the grey portions σ_{mc}, and the colored portions σ_{omp}. For observables for which the MCHF treatment didn't converge, due to limited number of histories probing the relevant phase space region, σ_{omp} could not be resolved. For most observables, the grey bands are negligible, indicating reasonable estimation of the actual OMP parameter uncertainty.

Figures 3.2 and 3.3 display the lab-frame PFNS for ^{252}Cf (sf) and ^{235}U (n_{th},f) compared

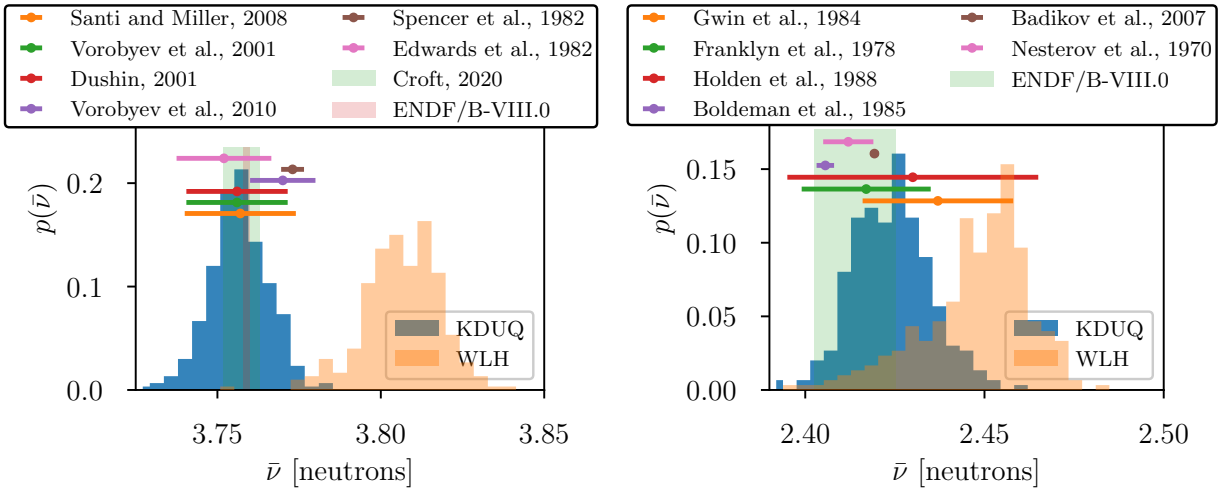

(a) ^{252}Cf (sf)

(b) ^{235}U (n_{th},f)

Figure 3.1: Distribution of average prompt neutron multiplicities produced by the uncertainty-quantified OMPs. (a) Prompt neutron multiplicity in ^{252}Cf (sf), compared to evaluations from Croft et al., [37], and ENDF/B-VIII.0 [22], as well as experimental results from [149, 171, 51, 170, 153, 52]. (b) Prompt neutron multiplicity in ^{235}U (n_{th},f), compared to the ENDF/B-VIII.0 evaluation [22], as well as experimental results and other evaluations [74, 60, 83, 17, 29, 93].

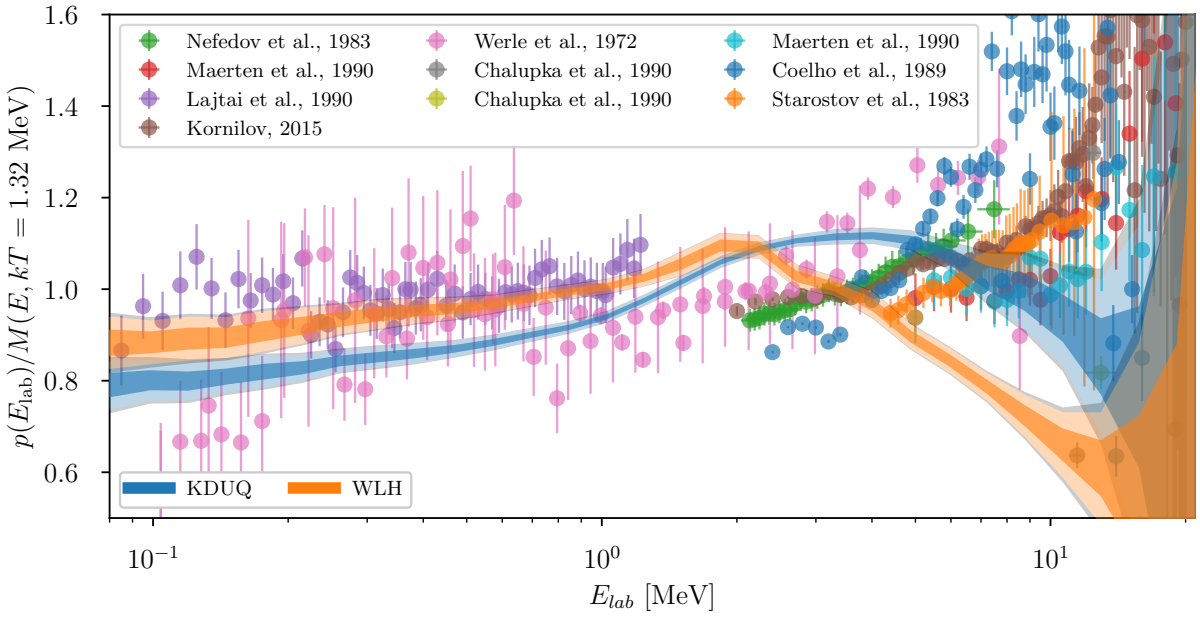

Figure 3.2: PFNS in the lab frame for ^{252}Cf (*sf*) as a ratio to a Maxwellian at kT = 1.32 MeV, compared to experimental results from [118, 127, 100, 96, 176, 32, 34, 154].

to a variety of measurements, all as ratios to a Maxwellian. Clearly, both models predict spectra that are too soft as compared to measurements, WLH especially so. From an energy budget standpoint, this helps explain the results for average neutron multiplicity. In the fast portion of the spectrum, the 1-10 MeV region, sensitivities to OMP parameter uncertainty is well-resolved and significant, especially for ^{235}U ($n_{\rm th}$,*f*).

Figure 3.4 displays the mean single-mass prompt neutron multiplicity for individual fragments as a function of fragment mass, compared to a variety of measurements. For most mass numbers, this observable is not strongly sensitive to the OMP, with the exceptions of the highly asymmetric region for both fissioning isotopes, and the highly symmetric region for ^{235}U.

Figure 3.5 displays the mean single-mass prompt neutron multiplicity as a function of the TKE of both fragments, compared to a variety of measurements. For both fissioning isotopes, this observables is fairly insensitive to both models, except for in the low TKE highly symmetric fission region. This region corresponds to highly deformed fragments

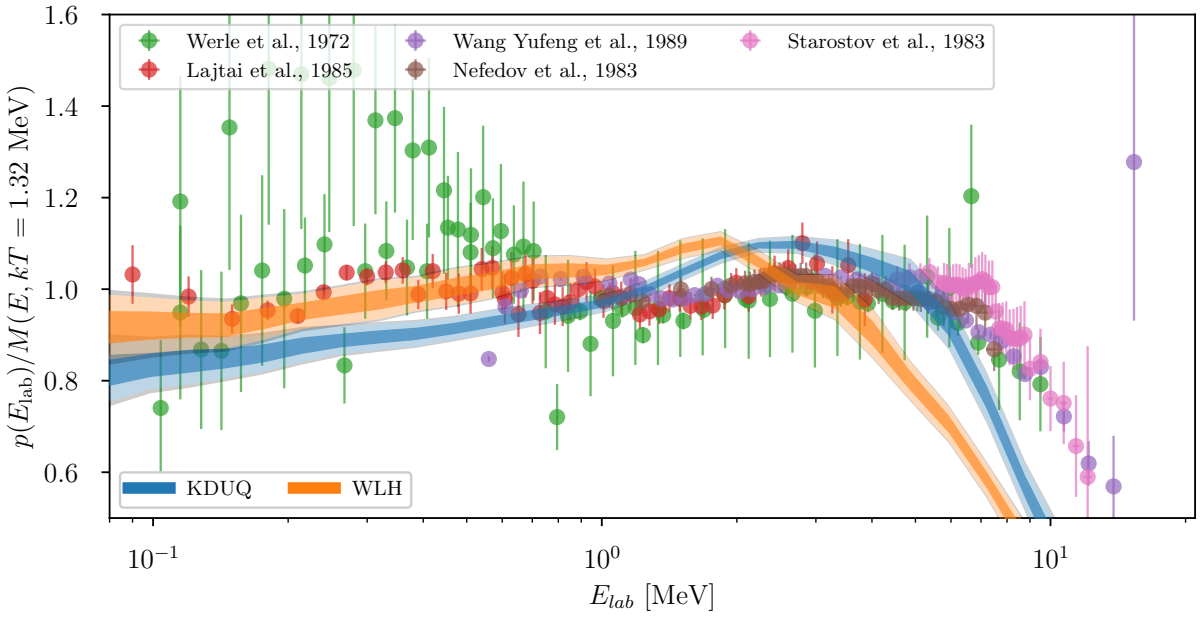

Figure 3.3: PFNS in the lab frame for ^{235}U ($n_{\rm th}$,f), as a ratio to a Maxwellian at kT = 1.32 MeV, compared to experimental results from [176, 99, 184, 127, 154].

post-scission, and, therefore, excitation energy dominated systems during de-excitation. Both models reproduce experiment well, especially the most recent measurement [68]. The insensitivity of mean neutron multiplicity conditional on fragment mass and TKE indicates the utility of these observables for inclusion as constraints of the global optimization of model inputs unrelated to the OMP, especially those related to scission.

Figure 3.6 displays the mean neutron energy as a function of fragment mass. Of course, both models predict spectra that are too soft, however this is not the case uniformly across mass number; the mass dependent behavior of each OMP is different. Interestingly, in the symmetric fission region, the sensitivity of the mean neutron energy was pronounced for ^{235}U, but not for ^{252}Cf. In fact, in the respective symmetric fission regions, both models strongly disagree to experiment for ^{252}Cf, but agree fairly well (despite large uncertainties) for ^{235}U, with WLH agreeing best. Both models exhibit poor agreement, for both fissioning isotopes, in the mass region $125 < A < 135$, which produces fragments near the ^{132}Sn double shell closure. This indicates a potentially rich mass region to investigate with future

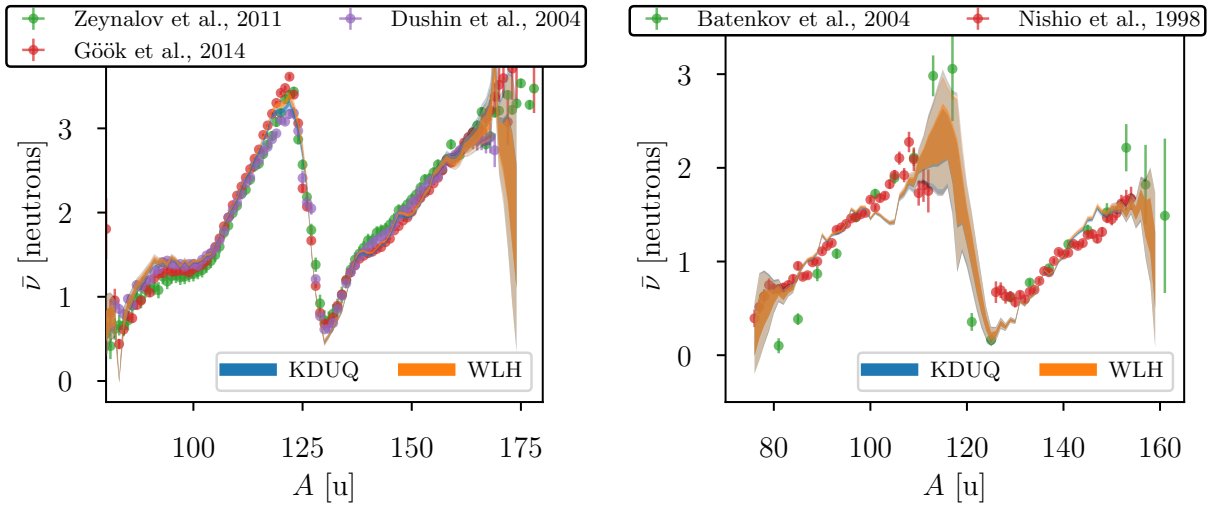

(a) ^{252}Cf (sf) (b) ^{235}U (n_{th},f)

Figure 3.4: Average neutron multiplicity from fragments of a given mass number for (a) ^{252}Cf (sf) compared to experimental results from [185, 24, 21, 45, 68, 51], and (b) ^{235}U (n_{th},f) compared to experimental results from [8, 130]

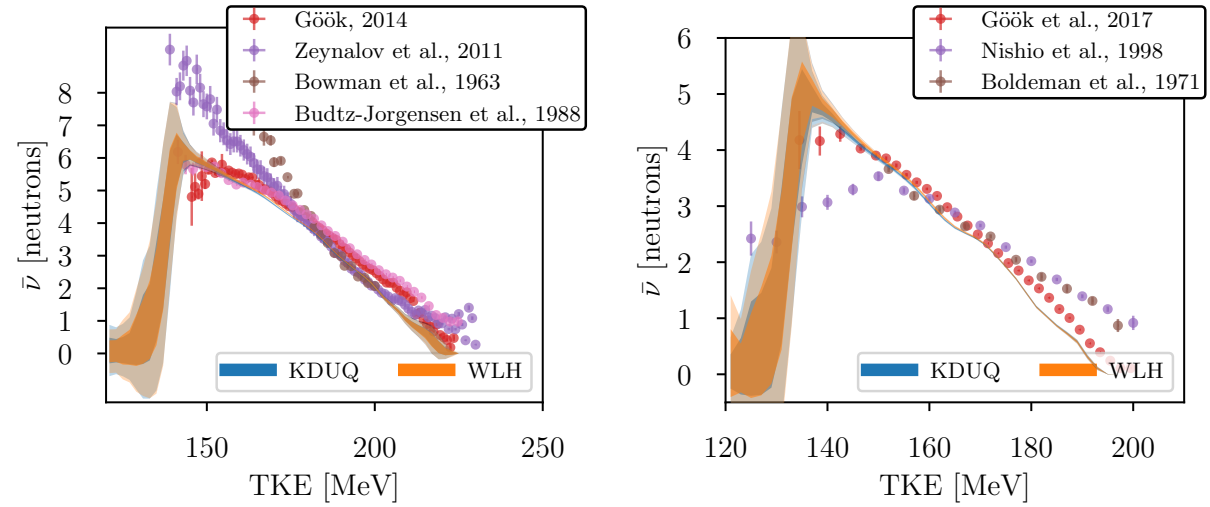

(a) ^{252}Cf (sf) (b) ^{235}U (n_{th},f)

Figure 3.5: Average neutron multiplicity as a function of TKE of the fragments for (a) ^{252}Cf (sf) compared to experimental results from [68, 185, 21, 24], and (b) ^{235}U (n_{th},f) compared to experimental results from [69, 130, 18]

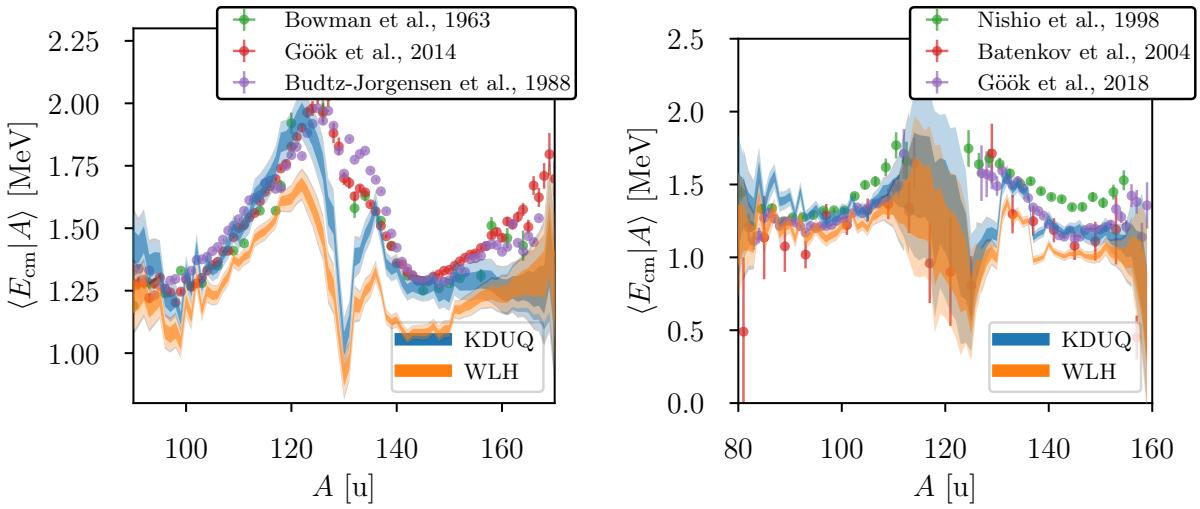

(a) ^{252}Cf (sf) (b) ^{235}U ($n_{\rm th}$,f)

Figure 3.6: Average neutron energy in the COM frame emitted from fragments of a given mass number for (a) ^{252}Cf (sf), compared to experimental results from [21, 68, 24], and (b) ^{235}U ($n_{\rm th}$,f) [130, 8, 69].

fission arm spectrometer experiments, for several reasons: 1) nuclides close to the shell closure are approximately spherical, so there is more validity in applying a spherical optical potential to them as opposed to other fission fragment isotopes; 2) the disagreement with experiment is largest here, but this is unexplained by the OMP uncertainties 3) the two OMPs disagree with each other in this region.

Figure 3.7 displays the mean neutron energy emitted from individual fragments as a function of the TKE of both fragments The shape of the mean neutron energy dependence of both models as a function of TKE is essentially the same, just shifted by $\sim$ 100keV. It is worth noting the disagreement obtained with experiment, further investigation should clarify this issue.

The mas dependence is explored further in Figs. 3.8 and 3.9, where single-fragment COM-frame PFNS are compared to [68], for a few selected mass number pairs. The mean and shape disagreement between the OMPs and experiment demonstrate the potential for fragment-neutron correlated time-of-flight measurements to constrain the mass-

dependence of OMPs away from stability. Particularly interesting is the peaked structure around $\sim$ 1MeV predicted by WLH, uniformly across fragment masses and fissioning isotopes.

On the experimental side, these spectra indicate a strong deviation from Maxwellian behavior for some fragments with some experiments having more than 5 times the number of neutrons in the $\sim$ 10MeV bin than the models predict, albeit with large uncertainties. This feature has been investigated before [91], but the systematic mass-by-mass calibration of model inputs to neutron spectra has yet to be done. Unfortunately, the large experimental uncertainties for most mass numbers does make this a challenge.

The highly asymmetric mass regions for both isotopes are potentially useful as constraints for the OMPs, as they are sensitive while being in regions that are well covered by experiment, with only moderate uncertainties and disagreements between experiments. We would not recommend fitting any non-OMP model inputs to any observables relating to neutron energy, without also considering the OMP amongst the free parameters, as the sensitivity is universally non-negligible.

Figures 3.10 and 3.11 display the mean single-fragment multiplicity conditional upon mass number and TKE of the fragment pair for a few selected mass number pairs. Again we see high sensitivity in the low TKE symmetric region. The experimental data is reproduced well for the most part, with the exception of systematic over/under-estimation for fragment pairs; e.g. $A \sim 104, 131$ in ^{235}U. Both models are essentially identical for these observables.

Figures 3.13, and 3.12 displays the mean neutron energy conditional upon fragment mass and TKE. While this observable could in principle be extracted from most of the other similar experiments; e.g. [68, 69, 24], it is only reported by Bowman et al. [21], and only for ^{252}Cf. As this is the most sensitive observable to the optical model, we recommend further experimental study in this direction. In both experiments, the overall shape as a function of TKE was roughly the same for both models.

Although the experimental data points are sparse, the agreement is reasonable with

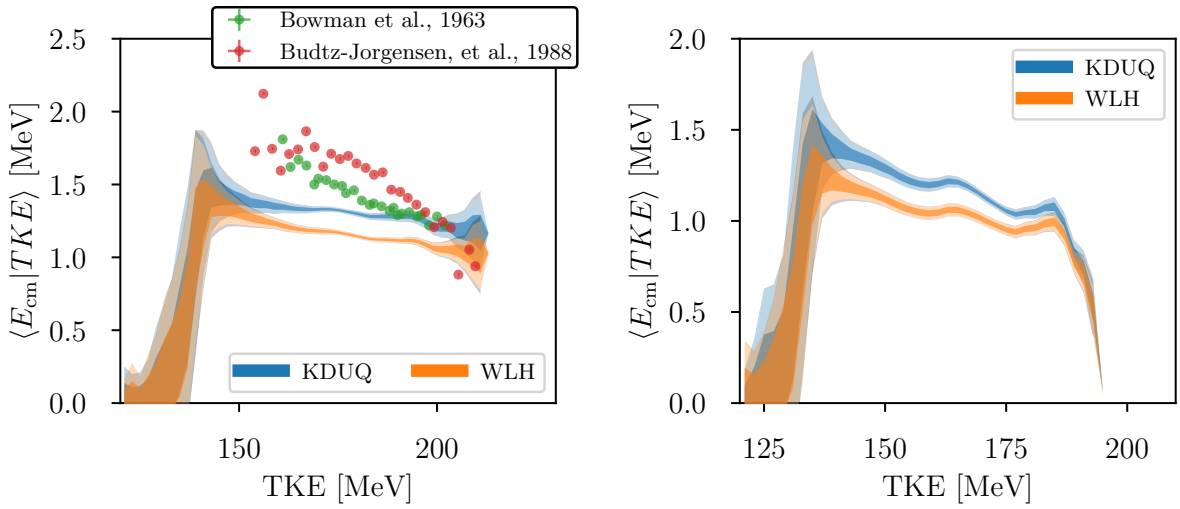

(a) ^{252}Cf (sf) (b) ^{235}U ($n_{\rm th}$,f)

Figure 3.7: Average neutron energy in the COM frame, as a function of the TKE of the fragment pair, for (a) ^{252}Cf (sf) compared to experimental results from [21, 24], and (b). ^{235}U ($n_{\rm th}$,f)

the exception of A = 131, in which it is off by up to an MeV in the region of TKE $\sim$ 200. This is well outside of the parametric model uncertainty, and could potential provide a useful constraint for calibration.

3.4 Discussion

We have shown that neutron-fragment correlated fission observables are sensitive to the form and parameterization of the OMP. In particular, neutron energy spectra are sensitive to OMP form and parameters, especially as a function of TKE. Neutron multiplicities are slightly sensitive due to energy budget considerations, but this is a second order effect and not relevant given the size of experimental uncertainties. On the other hand, neutron energy spectra, when differentiated on mass and TKE, show significant sensitivities in observable regions that converged in the MCHF treatment. The low TKE region is especially sensitive, although it is difficult to access experimentally.

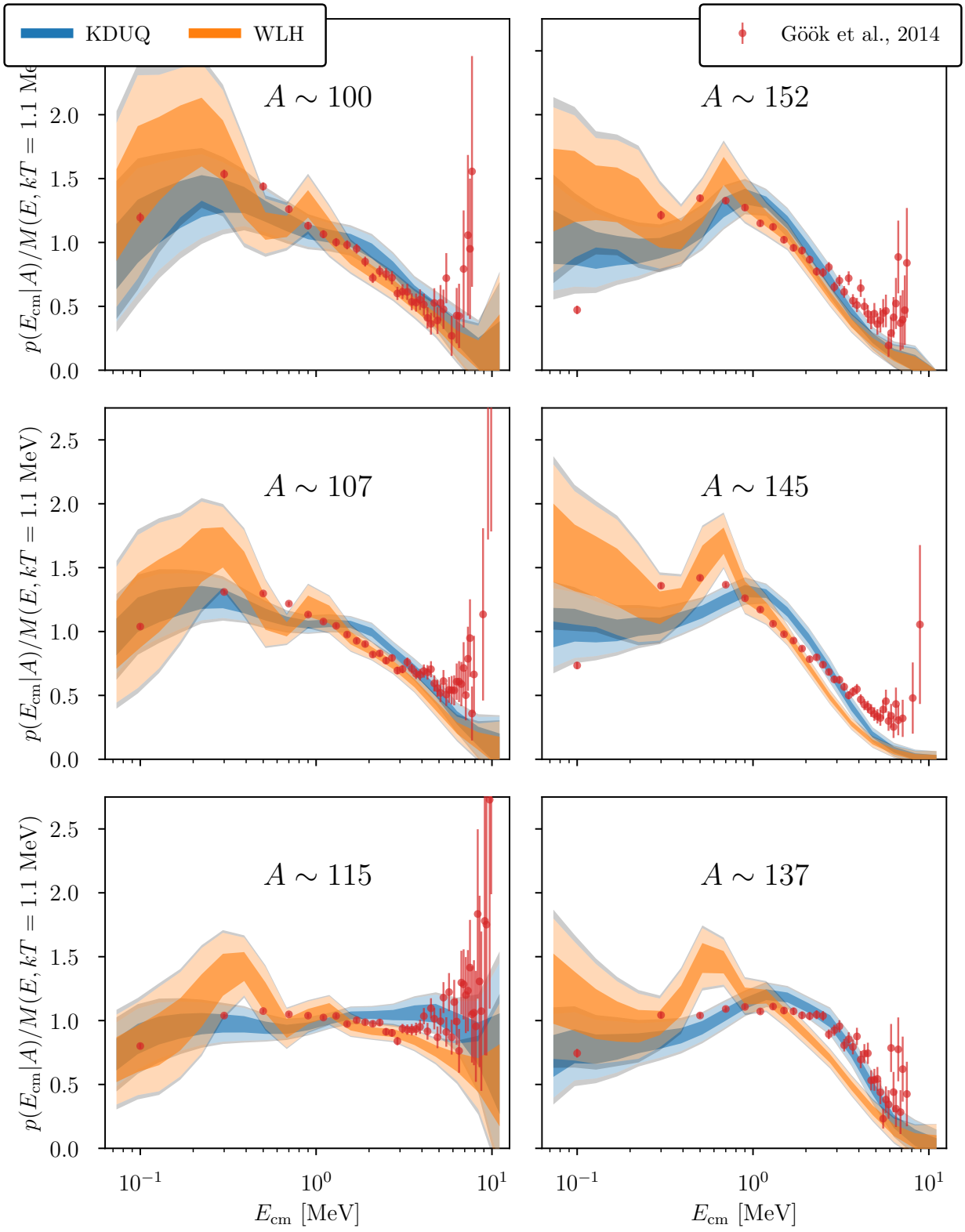

Figure 3.8: PFNS ratio to a Maxwellian with kT = 1.1 MeV, and conditional on fragment mass, for ^{252}Cf (*sf*) compared to experimental data from [68].

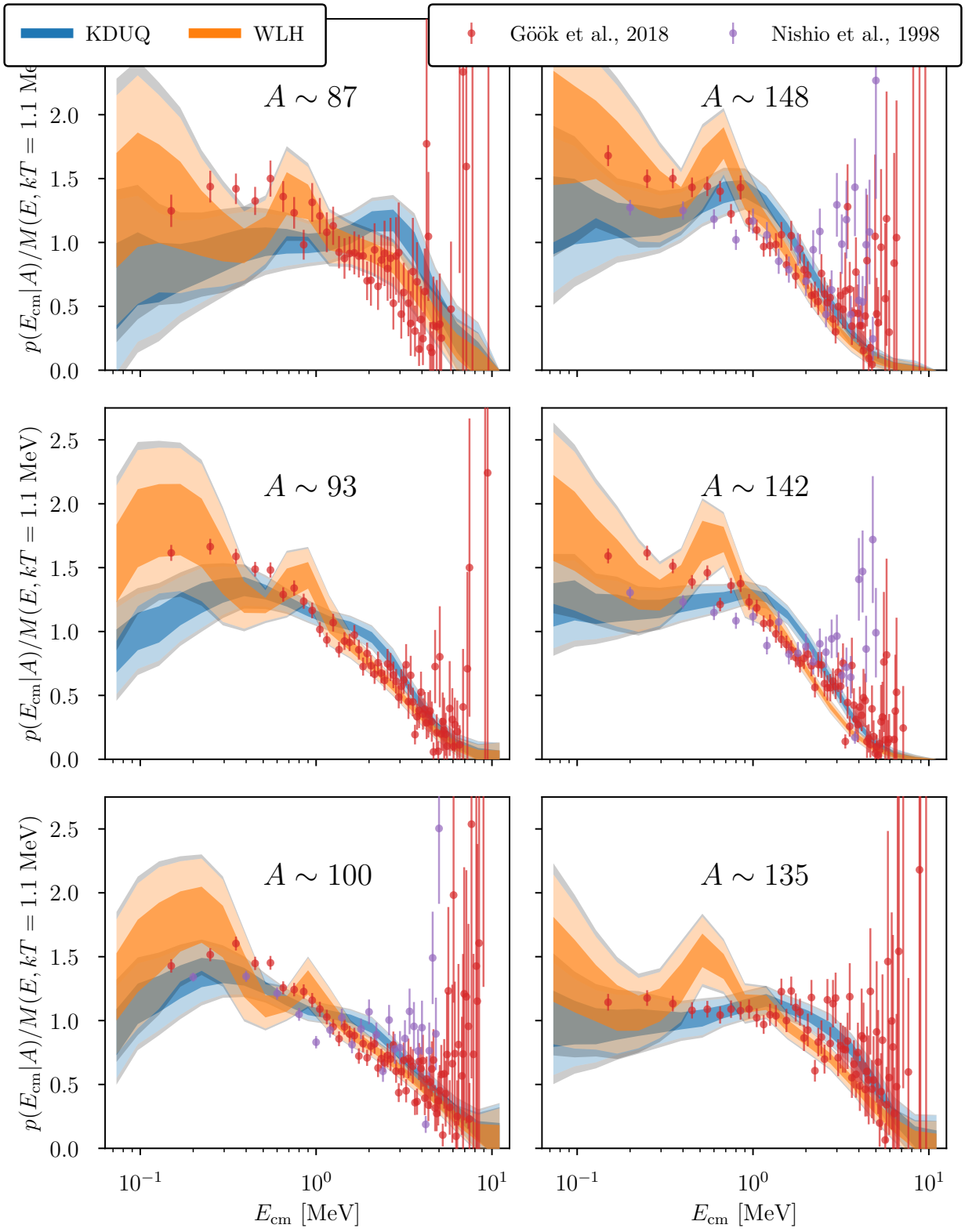

Figure 3.9: PFNS ratio to a Maxwellian with kT = 1.1 MeV, and conditional on fragment mass, for ^{235}Cf (n_{th},f) compared to experimental data from [69, 130].

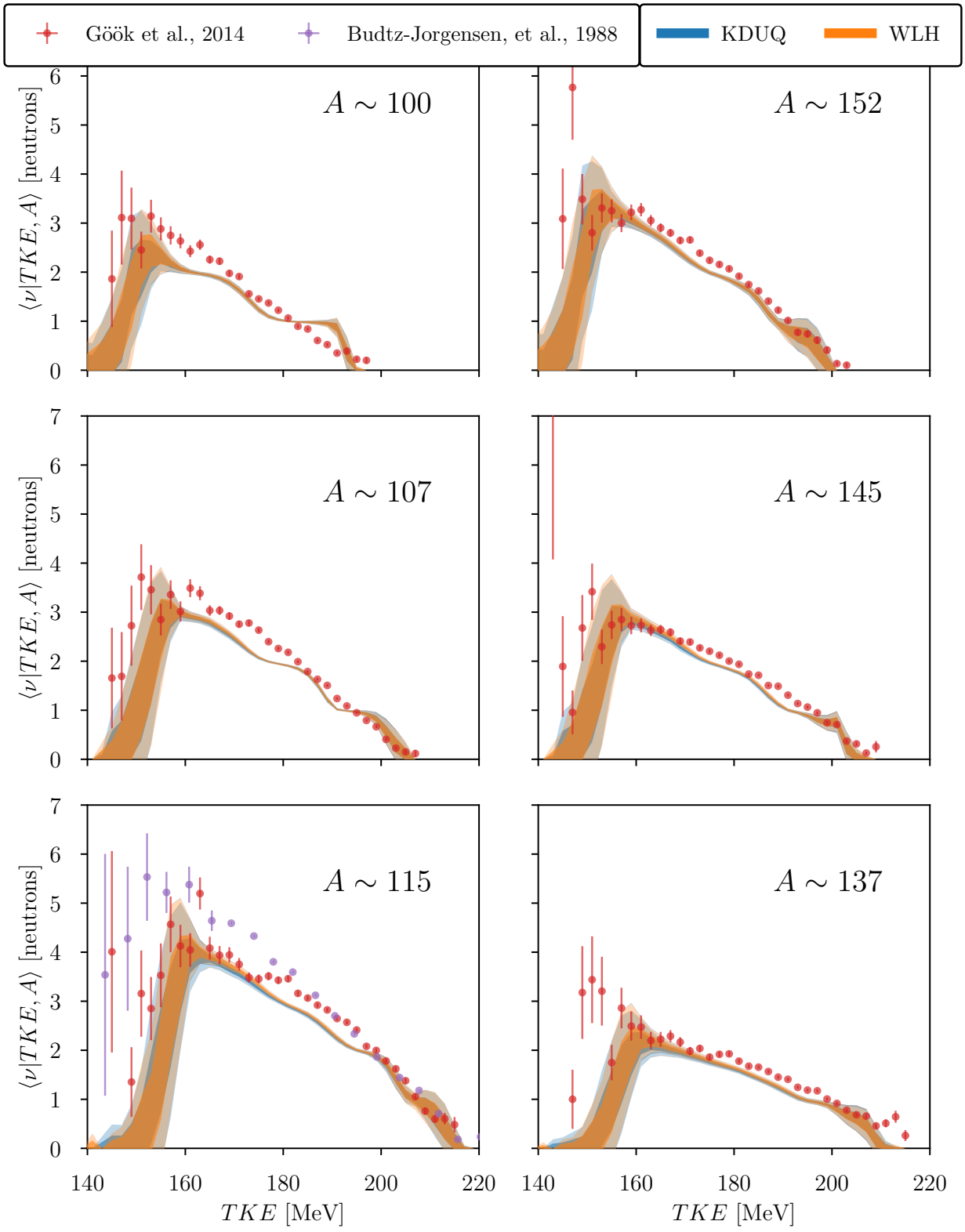

Figure 3.10: Single-fragment neutron multiplicity as a function of the TKE of both fragments, and conditional on fragment mass, for ^{252}Cf (*sf*) compared to experimental data from [68, 24].

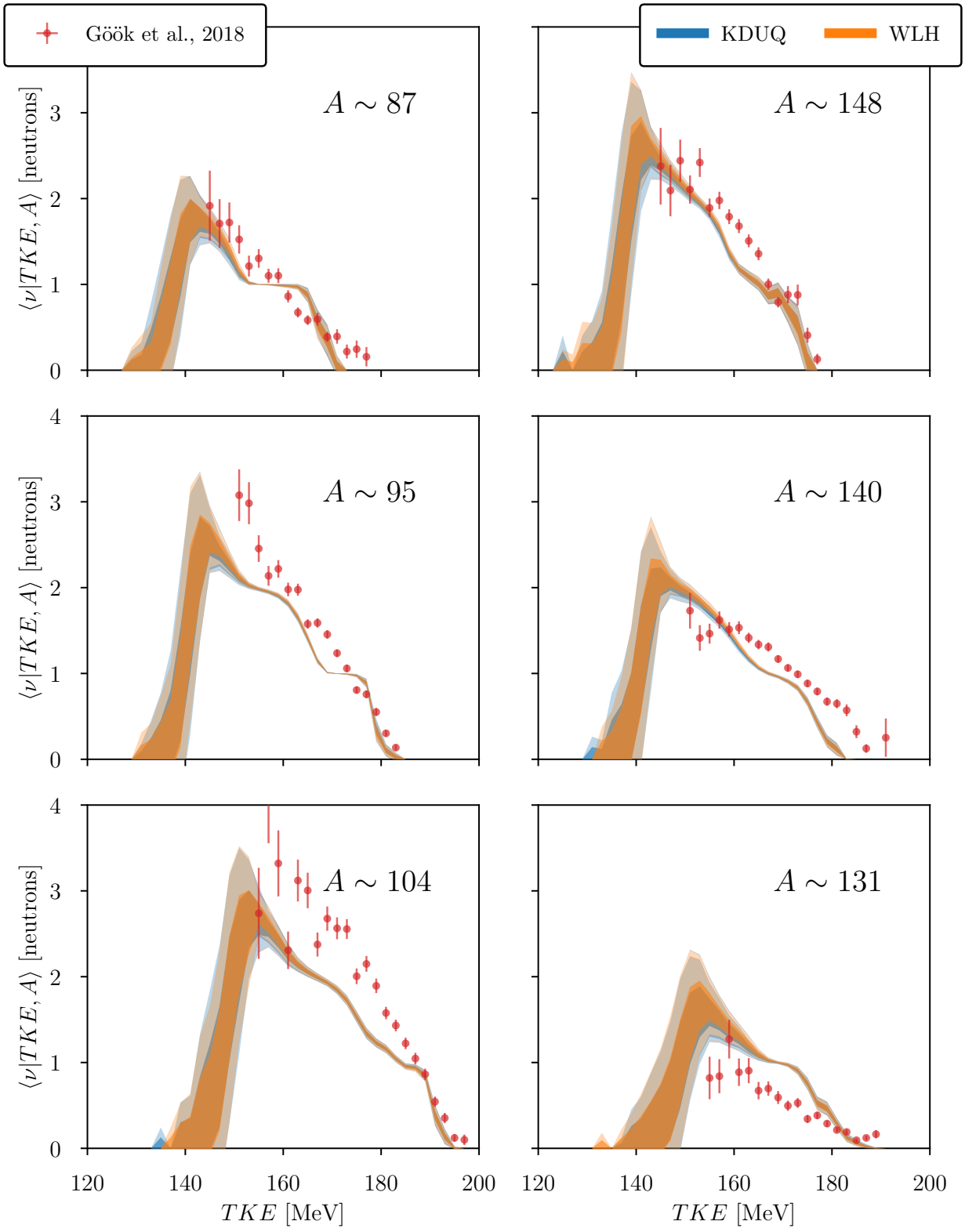

Figure 3.11: Single-fragment neutron multiplicity as a function of the TKE of both fragments, and conditional on fragment mass, for ^{235}U (n_{th},f) compared to experimental data from [68].

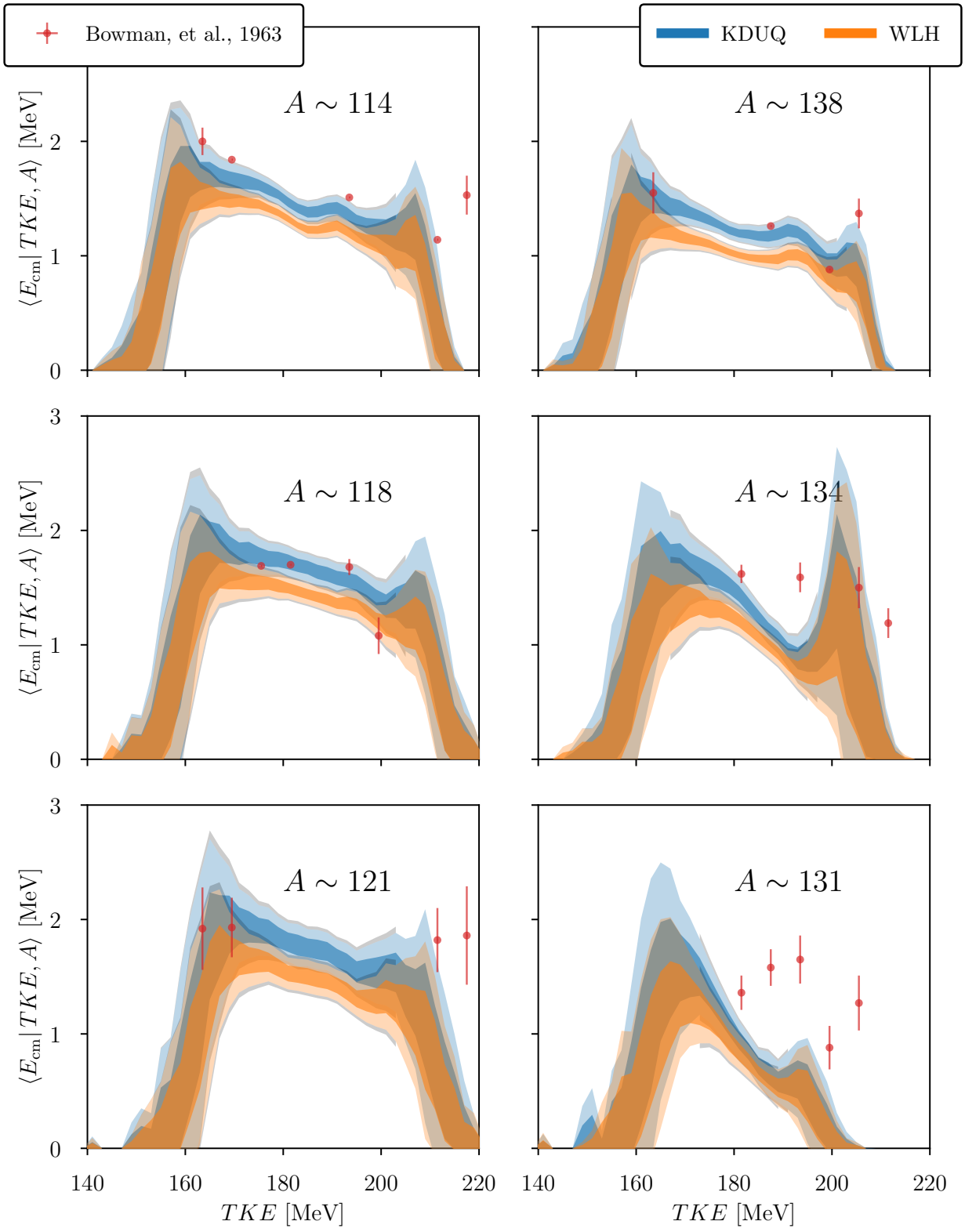

Figure 3.12: Average COM-frame neutron energy as a function of the TKE of both fragments, and conditional on fragment mass, for ^{252}Cf (*sf*) compared to experimental data from [21].

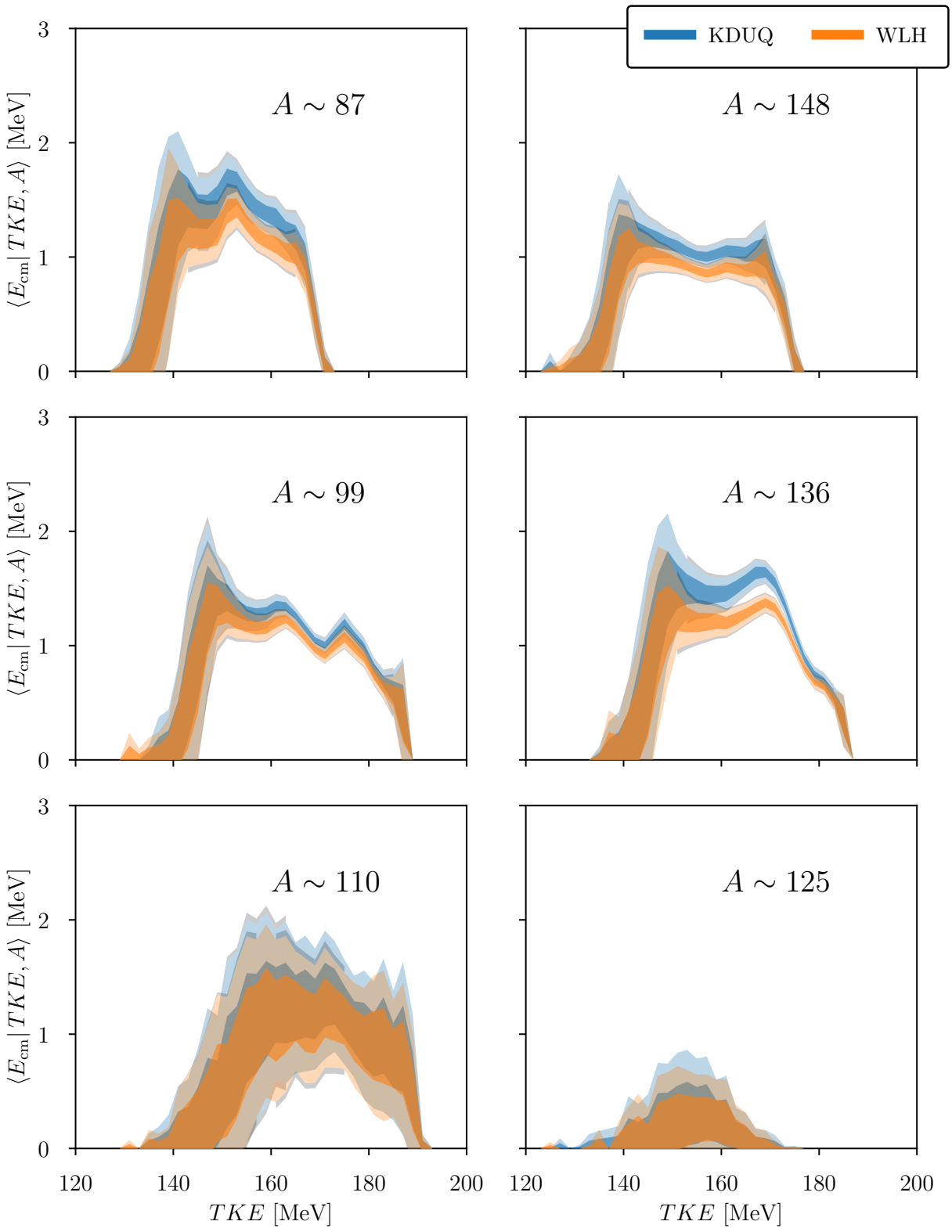

Figure 3.13: Average COM-frame neutron energy as a function of the TKE of both fragments, and conditional on fragment mass, for ^{235}U (n_{th},f).

Of particular interest is the energy spectra of neutrons emitted in the mass region near the ^{132}Sn shell closure. The strong disagreement between experiment and theory cannot be explained purely by the uncertainty in the OMP priors, and, furthermore, the OMP forms disagree with each other in this region to statistical significance. Further study of fission fragment initial conditions, informed by experiment microscopic time-dependent or adiabatic mean-field calculations of scission, may shed light on the role of excitation energy sharing in this region, but the role of the OMPs cannot be ruled out. Additionally, the parameterization of level densities may need to be revisited. Future work should investigate the sensitivity of these fission observables to level density parameters, as well as fission-fragment initial conditions.

Throughout the observables, significant differences were observed between OMP forms. The WLH potential in particular predicted much softer spectra than the phenomenological potential. WLH produced reasonable spectra for light fragments, but was significantly softer than experiment for heavy. This points to potential issues with the nuclear matter folding approach at low energy, due to finite size effects and long-range correlations. This has been pointed out in relation to the JLMB semi-microscopic potential as well [71]. In general, the imaginary strength of microscopic OMPs developed in folding approaches is smaller than that in corresponding phenomenological potentials, likely due to missing configurations that describe, or act as doorway states to, collective excitations which contribute to CN states. For example, at second order in many-body perturbation theory, 3-particle–2-hole states are neglected. Specifically for the WLH potential, the total imaginary part of the potential is less surface peaked than in phenomenological potentials [84].

Especially in the case of fission fragments, we expect low-lying collective excitations to arise in the form of rotational and vibrational modes. Explicitly including these couplings in the form of a coupled-channels OMP would, in principle, provide a better description, but this has not been done in the case of fission due to computational constraints and lack of information about excited states in neutron-rich nuclei. However, as described in Chapter 2,

the HF approach only requires that the branching ratios, not transmission coefficients, to the ground state well describe those to excited states, which alleviates part of this issue.

Future work will explore the possibility of describing deformed fragments by including coupling to low-lying collective excitations. As this is not likely to be computationally tractable within MCHF, emulators capable of significant speed up to the calculation of transmission coefficients are being explored and developed [20, 64, 121]. Additionally, leveraging microscopic descriptions of excited states is worth exploring if they provide predictions different from collective models, or remove poorly constrained input parameters (such as quadrupole deformations of fission fragment ground states) from the calibration.

This effort is directed towards including fission observables as constraints for OMP parameters. As discussed, there are a wide variety of other fissioning isotopes that can be studied, with a large quantity of associated experimental data. In particular, precision fragment-neutron correlated experiments, using time-of-flight fission arm spectrometers, are beginning operation, and promise the most precise fission-fragment measurements to date [120]. Performing these measurements in correlation with prompt neutrons would likely provide the most precise and detailed data, against which to compare fission models, to date. The ability to leverage emulators to do rapid uncertainty quantification of MCHF models for fission – and other CN processes – would open up the door for adding new constrains to OMPs away from stability.

Future work optimizing model inputs to MCHF fission event generators should be guided by this work to include neutron-fragment correlated multiplicities (i.e. $\bar{\nu}$ conditional on A and/or TKE). Furthermore, measurements of mass-dependent neutron energy spectra provide a (admittedly model-dependent) measurement of fragment temperatures [24]. Using these as Bayesian priors in such a calibration, or incorporating them as a constraint in the likelihood function, should be investigated.

Chapter 4

The Optical Potential and the Nuclear Symmetry Energy

In this chapter, we attempt to approximately reconstruct, or unfold, the strength of the nuclear matter optical potential at saturation density, from the Whitehead-Lim-Holt (WLH) and Koning-Delaroche uncertainty quantified (KDUQ) optical potentials, which are formulated for finite nuclei. Then, by applying the Hugenholtz–Van Hove theorem, we can relate this single-particle effective potential to the nuclear matter Equation-of-State (EOS). In particular, we can relate the symmetry energy of the EOS to the isovector part of the optical potentials. Similar analysis done in the past ([183]) has indicated that phenomenological optical potentials are roughly consistent with reconstructions of the symmetry energy at saturation density from terrestrial experiments and astrophysical observations. Here, we revisit this analysis using the uncertainty-quantified optical potentials WLH and KDUQ, and show that this consistency is still true within parametric uncertainty of both models. Interestingly, we find a very large variance in predicted symmetry energy quantities from KDUQ, indicating a fundamental limitation of scattering observables to constrain the symmetry energy. We discuss future improvements that can be made, and discuss correlations

between these nuclear matter EOS quantities and fission observables.

4.1 Formalism

Xu et al., [183] derived in 2010 the relationship between symmetry energy and its density slope, and the optical potential using the Hugenholtz–Van Hove theorem [87]. The value of its density slope around saturation density $L(\rho_0)$ is an important model input in the determination of many quantities relating to heavy and unstable nuclei, including the size of the neutron skin in heavy nuclei [166], and the location of the neutron drip line [135], as well relating to neutron stars, including the core-crust transition density and gravitational binding energy [49, 128]. We perform a similar analysis for KDUQ and WLH, and compare to evaluated global averages, extracted by Li et al., from terrestrial experiments, including atomic masses and neutron skins of Sn isotopes, nuclear masses within the finite-range droplet model (FRDM), Pygmy dipole resonances, and dipole polarizability, and astrophysical observations, including neutron star crust oscillation and r-mode instability [105].

Global neutron and proton optical potentials with depth terms which can be written as

$$V_{n/p}(\rho,k) = V_0(\rho,k) \pm \delta V_1(\rho,k), \tag{4.1}$$

where

$$\delta \equiv \frac{\rho_N - \rho_Z}{\rho_N + \rho_z}, \tag{4.2}$$

are said to be Lane-consistent. We have defined $\rho_{N/Z}$ as the neutron/proton density, δ is the degree of asymmetry. V_0 and V_1 are, respectively, the isoscalar and isovector terms. Lane consistency in an optical potential is simply a statement that the potential depends on the projection of the projectile nucleon isospin on the isospin of the target. We have

included the density ρ as an argument in $V_{0/1}$, as the self-energy is density dependent. Because nuclei exist at the saturation density, the optical potential only provides constraints at $\rho = \rho_0$. Otherwise, it is the same as defined in Chapter 2, with $E = E_k = \frac{\hbar^2 k^2}{2m}$.

In the context of Fermi-liquid theory, the Hugenholtz-Van Hove theorem relates the Fermi energy to the energy density and the pressure of a system at zero temperature. By considering the optical potential as the mass operator in nuclear matter, [115], one can derive the relationship of symmetry energy and its density slope in nuclear matter, to the isovector component of the optical potential. We only consider the volume term, as the surface and spin-orbit terms don't exist in nuclear matter. The expressions derived in [183] read:

$$E_{sym}(\rho) = \frac{1}{3}\frac{\hbar^2 k_F^2}{2m^\star} + \frac{1}{2}V_1(\rho, k_f), \tag{4.3}$$

and

$$L(\rho) = \frac{2}{3}\frac{\hbar^2 k_F^2}{2m^\star} + \frac{3}{2}V_1(\rho, k_f) + k_F \frac{\partial V_1(\rho, k)}{\partial k}\bigg|_{k=k_F}, \tag{4.4}$$

where the Fermi momentum $k_F = \left(\frac{3\pi^2\rho}{2}\right)^{1/3} \approx 1.36$ fm^{-1}. The effective mass splitting in nuclear matter is the difference in the effective mass ratio $m^\star/m$ between neutrons and protons. In terms of the isovector potential:

$$\frac{m_n^\star - m_p^\star}{m} = -2\delta \frac{m}{\hbar^2 k_F^2}\frac{\partial V_1(\rho, k)}{\partial k}\bigg|_{k_F} \Bigg/ \left[1 + 2\left(\frac{m^\star}{m} - 1\right)\right]. \tag{4.5}$$

We extract these quantities from KDUQ and WLH, using the empirical values for nuclear matter of $\epsilon_F = 16$ MeV and $m^\star/m = 0.7$ [90]. Fig. 4.1 displays the uncertainty-quantified energy dependence of the isovector energy in the two potentials. Interestingly, the nuclear matter approach, WLH, and the phenomenological approach based on scattering, KDUQ, agree to within uncertainty above $\sim$ 25MeV, well into the scattering continuum, but they

disagree for bound states above the Fermi energy, and the disagreement becomes worse at more bound energies below ϵ_F. This potentially indicates that the lack of constraints from bound states, especially deeply bound states below the Fermi energy, in KDUQ, cause it to become inconsistent with nuclear matter calculations using chiral forces. Also interesting is the divergence of the uncertainty in the isovector term at high energies. Evidently, this is a difficult quantity to constrain when limited to the valley of stability.

Also of note is the improved agreement of the default Koning-Delaroche (KD) isovector potential with WLH. In fact, below the Fermi energy, the default KD parameterization is outside the KDUQ uncertainty band. This could potentially be due to the extra analytical constraints for Lane consistency used in KD not present in KDUQ (see [95] Eq. 20). This constraint takes the form of an analytical function of energy $g(E)$ chosen to enforce Lane-consistency between neutron and proton real volume depths like so:

$$\begin{aligned} V_n &= (V_0 - \delta V_1) g(E) \\ V_p &= (V_0 + \delta V_1) g(E). \end{aligned} \tag{4.6}$$

The result of this approach to formulating the functional forms for KD is that an approximate Lane consistency is achieved, as the dominant contributions to the isovector part of the real depth term are held the same for potentials for both incident neutrons and protons, and it is only small energy and mass-dependent corrections that break this symmetry. For WLH, far fewer parameters are held consistent between the neutron and proton potentials, so that poorer Lane consistency is achieved.

In general, Coulomb corrections break the simple form of Lane consistency given here. More generally applicable are the full coupled Lane equations, see e.g. the appendix of [101]. To best avoid ambiguities relating to the electromagnetic effects, in the following analysis we construct the isovector depth V_1 using the respective potential forms for neutron projectiles. Alternative formulations (e.g. using the isovector part of the proton depths, or subtracting the full neutron and proton depths) require Coulomb corrections, and are

not explored here. Additionally, the isovector depth is mass-dependent in KD, so we take $A = 208$ to represent an experimentally well-constrained isotopic chain with a large enough mass for the interior of the nucleus to effectively represent nuclear matter.

In the case of a folding potential like WLH, in the local density approximation, the depth term reflects the strength of the nuclear matter potential at the density corresponding to the interior of the nucleus (saturation density), as the Woods-Saxon form factor is equal to 1 at $r = 0$. In principal, the same could be said for phenomenological potentials like KD, however, there is no underlying density-dependent nuclear matter potential used to construct them. A more detailed analysis would apply some unfolding procedure to reconstruct such a density-dependent nuclear matter potential from that for a finite nucleus. To the knowledge of the authors, this hasn't yet been attempted in the literature. Instead, we take the reasonable approximation that the potential strength in the interior of a large nucleus is similar to the self-energy in nuclear matter, justifying the application of the Hugenholtz–Van Hove theorem.

In the following results, we propagate the same parameter samples as in the previous chapter for fission into Eqs. 4.3, 4.4, and 4.5. Namely, we use the federal form of KDUQ, and the same samples generated from a multivariate normal approximation as before for WLH.

4.2 Results & discussion

Figs 4.2 and 4.3 display, respectively, the mass splitting and the relation between E_{sym} and its density derivative $L(\rho)$, extracted from a distribution of 300 parameter samples from each of the posteriors of WLH and KDUQ, with the default KD values indicated. For comparison are the global evaluations of [105]. These paint the, perhaps predictable, picture that the nuclear matter approach of WLH better reproduces nuclear matter properties than does the phenomenological KDUQ. In any case, it is encouraging that the chiral forces reproduce

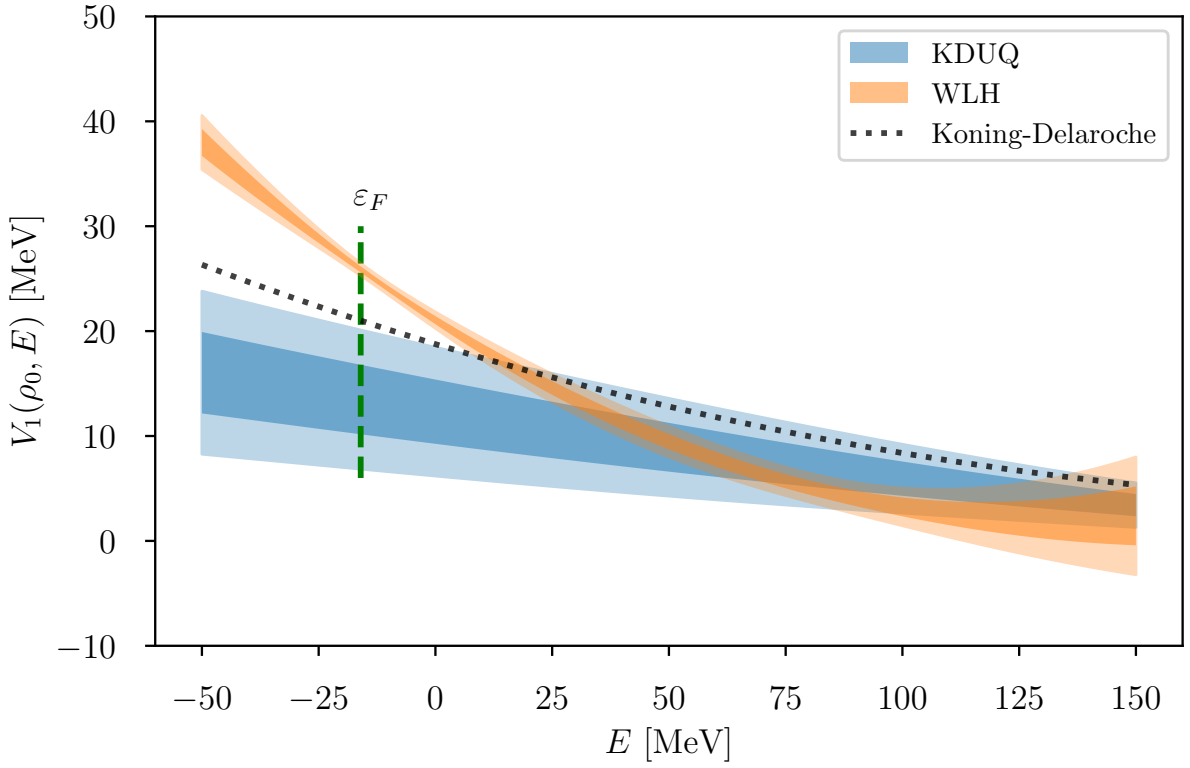

Figure 4.1: The isovector component of the real volume term in WLH and KDUQ as a function of energy. The Fermi energy, ϵ_F, where the symmetry energy and its density slope are extracted, is marked. Compare to Fig. 1 of [183]. Uncertainty bands of 1 and 2 standard deviations are shown, with the mean marked as a solid line.

well these important quantities, as originally pointed out by Whitehead et al. [177].

Moreover, this is an indication that the value of the isovector depth at the Fermi energy in WLH (and its momentum slope about it), are more accurate to terrestrial and astrophysical experiments than is KDUQ. Evidently, because KDUQ is only constrained by scattering with $E > 0$, it does not reproduce symmetry behavior at the Fermi energy that is consistent with nuclear matter. Combined with the fact that scattering data clearly has limits on how much it can constrain V_1 (see the large uncertainties in Fig. 4.1), there is a clear conclusion to be drawn: future work constructing global optical potentials should include constraints from bound states, especially from hole states below the Fermi energy. Furthermore, they should be constructed in such a way to be consistent with these important nuclear matter

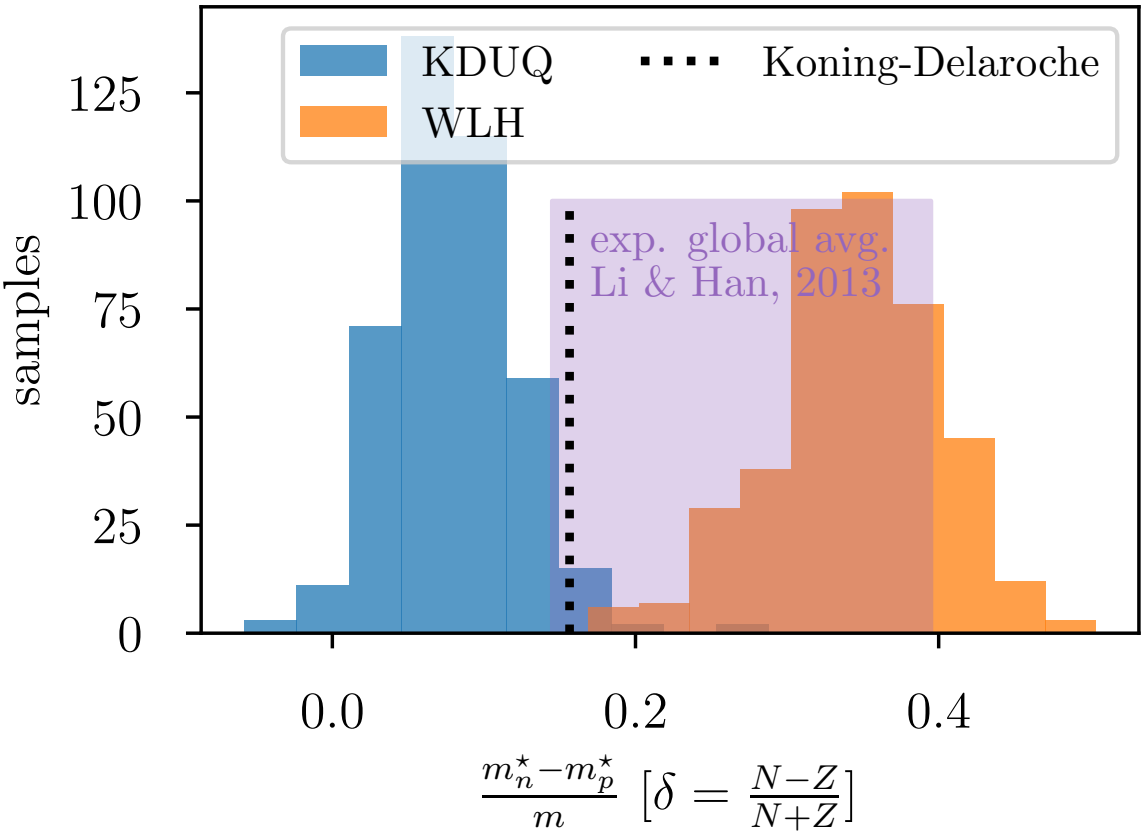

Figure 4.2: The neutron-proton mass splitting in nuclear matter extracted from WLH and KDUQ, as compared to a global average of terrestrial experiments and astrophysical observations from [105].

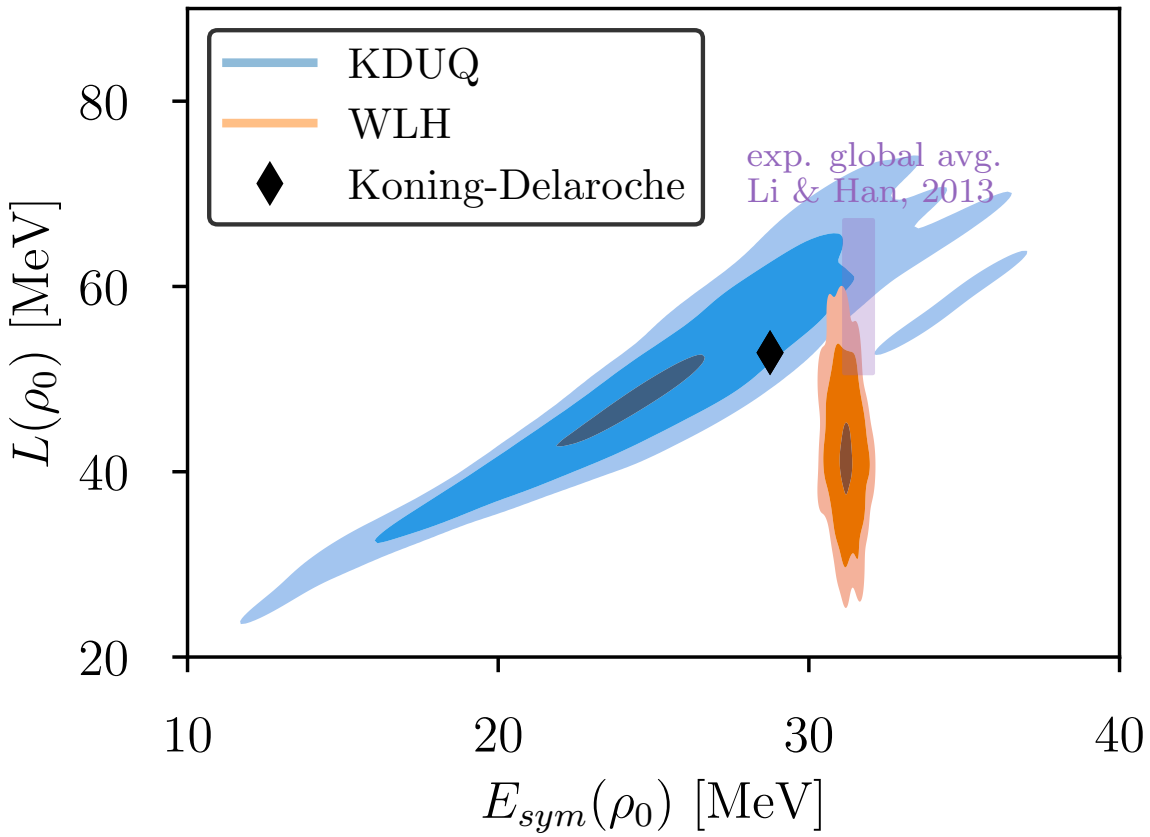

Figure 4.3: The symmetry energy of nuclear matter plotted against its density slope extracted from WLH and KDUQ, as compared to a global average of terrestrial experiments and astrophysical observations from [105], as well as the global average from phenomenological optical model potential (OMP)s [183].

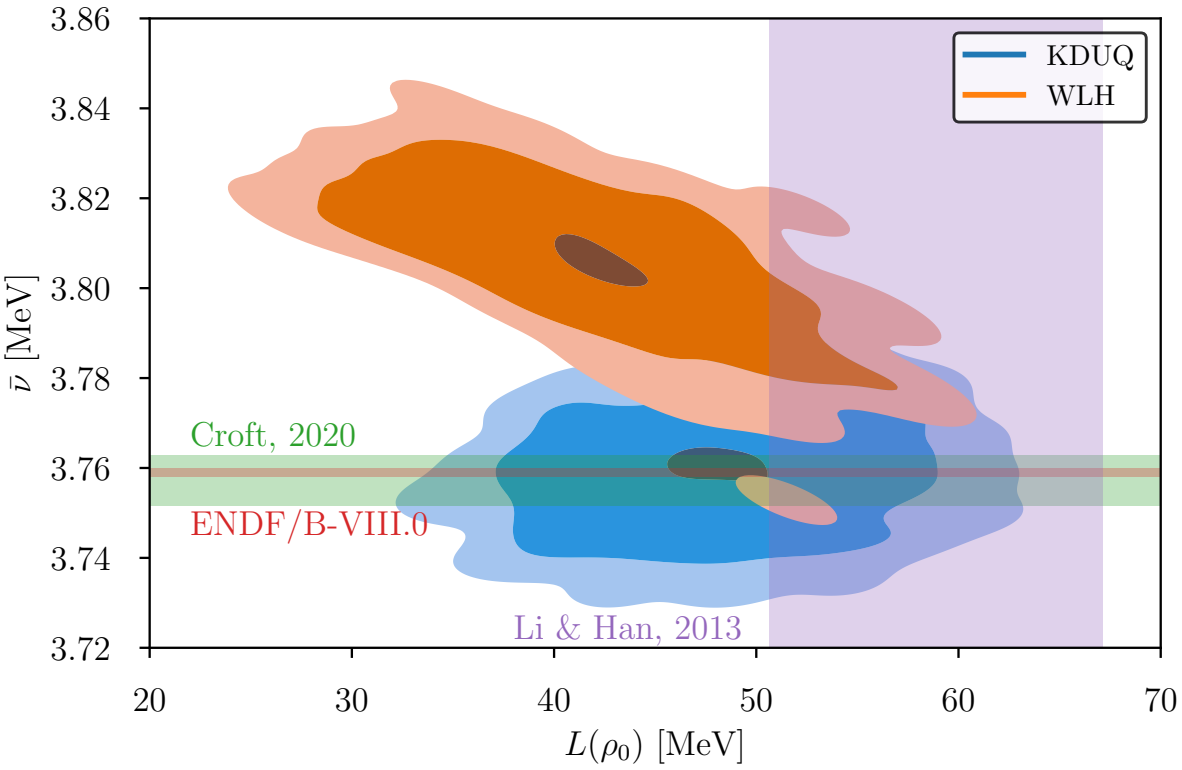

Figure 4.4: The density slope of the nuclear symmetry energy around saturation density, $L(\rho_0)$ plotted against $\bar{\nu}$ in ^{252}Cf(sf). For comparison are evaluations of $\bar{\nu}$ from Croft et al., [37], and ENDF/B-VIII.0 [22], and the experimental global average of the symmetry energy density slope from Li et al., [105].

quantities.

Fig. 4.4 displays the distribution of predictions of the symmetry energy compared to that of $\bar{\nu}$ in ^{252}Cf(sf). This is a concrete example of the application of orthogonal experimental constraints discussed in Section 1.2, as neither of these quantities have been used to constrain an optical potential. It turns out that, for KDUQ, these two quantities are not correlated, while for WLH they are. This indicates broadly that the simultaneous application of fission observables and nuclear matter quantities could be useful for constraining an optical potential using WLH as a microscopic prior. The fact that two quantities that should constrain the extrapolation of KDUQ away from β-stability to the neutron-rich region are not correlated perhaps points to limitations of fitting only to scattering observables.

Chapter 5

Projective Model Order Reduction for Global Optical Potentials

In this chapter, we develop the formalism for and demonstrate a new emulator based on projective model order reduction (PMOR) for two-body scattering. Using a Galerkin formulation, we derive reduced basis method (RBM) (see Refs. [20, 47, 142, 79] and references therein). We demonstrate that the reduced basis method (RBM), equipped with the empirical interpolation method [7, 73], allows for the construction of computationally efficient surrogate models for scattering, even with non-affine interaction terms. In the optical potential defined in Eq 2.69, the non-affine parameters are the radius and diffuseness of each term, as well as the energy dependence of the system.

We introduce the associated software, called the `Reduced Order Scattering Emulator (ROSE)` [133], that is an integrated part of the publicly available BAND software suite[15]. The performance of the emulator is explored and assessed by calibrating a realistic local optical potential by constraining elastic cross sections. These results have also been reported in [134]. These techniques are explained pedagogically with code examples online [66]. We also introduce the software package `just-in-time R-matrix (JITR)`, which is

called within `Reduced Order Scattering Emulator (ROSE)` as a high-fidelity solver of the scattering equations [13].

Next, we discuss the unsuitability of a single RBM-based emulator to perform accurately for a global optical potential across a large swath of the nuclear chart, and across a large energy range. To ameliorate this issue, we develop the active subspace quilting (ASQ) method, which stitches together multiple RBM models as local tangent spaces using techniques similar to the Active Subspace Method of Constantine et al. [36]. We develop a novel, computationally efficient method for discovering the active subspace for an RBM emulator, and outline an iterative procedure to discover the optimal decomposition of the parameter space into local tangent neighborhoods. We demonstrate the effectiveness of this technique for emulating a global optical potential trained on 46 isotopes and multiple of orders of magnitude of energy. We further discuss potential avenues for improving this method into the first production quality tool for projective model order reduction (PMOR) of parametric systems on non-linear manifolds in the context of nuclear physics.

Applications of this method include Bayesian calibration of global optical potentials, and speeding up Monte Carlo Hauser-Feshbach (MCHF) calculations as in `CGMF`. Emulators have potential to bring physicist closer to their model, being able to iterate on model creation rather than spending time running expensive simulations. A good example of this is the Bayesian Mass Explorer [65]. A successful emulator of a global optical potential could be a useful tool for a similar proposed Bayesian Reaction Explorer, in which users could compare experimental data to models of their choice at the click of a button on a website, rather than through a lengthy calculation.

Before we move into the discussion of the PMOR techniques developed in this work, we briefly comment on the modification of the Bayesian framework discussed in Chapter 2 required when using an emulator, with it's own associated error, in model calibration. Once the emulator is built, the posterior likelihood, Eq. 2.75, is modified to account for the emulator's approximate nature, which is characterized by some prediction mean $\mu(\omega)$ and

covariance $\mathbf{\Sigma}_{\text{Emu}}(\boldsymbol{\omega})$. The new, approximate, posterior assumes independence of emulator and observation error:

$$p(\boldsymbol{\omega}|y) \propto |\mathbf{\Sigma} + \mathbf{\Sigma}_{\text{Emu}}(\boldsymbol{\omega})|^{-\frac{1}{2}} \\ \exp\Big\{ -\frac{1}{2}\big(y - \boldsymbol{\mu}(\boldsymbol{\omega})\big)^{\mathsf{T}}\big(\mathbf{\Sigma} + \mathbf{\Sigma}_{\text{Emu}}(\boldsymbol{\omega})\big)^{-1}\big(y - \boldsymbol{\mu}(\boldsymbol{\omega})\big)\Big\} p(\boldsymbol{\omega}), \tag{5.1}$$

A developer of a model using emulators must then be careful to understand well the associated error, and incorporate it into the calibration. We demonstrate this practice in this chapter.

5.1 The reduced basis method (RBM)

We would like to emulate the parametric system, Eq. 2.68. For the local optical potential considered here, $\boldsymbol{\omega}$ is the list of ten parameters:

$$\boldsymbol{\omega} = \{V_v, W_v, R_v, a_v, W_d, R_d, a_d, V_{so}, R_{so}, a_{so}\}, \tag{5.2}$$

that characterize the strength, radius, and diffuseness of real and imaginary volume, imaginary surface, and real spin-orbit Woods-Saxon terms in Eq. 2.69. These parameters define a space, and at each point in space, there is a solution to Eq. 2.68. The core idea behind the success of the RBM is that, although the Hilbert space is of large or infinite dimension, as a function of $\boldsymbol{\omega}$, the solutions live in a low-dimensional, smooth manifold.

It is convenient to rescale Eq. 2.68 by the change of variables $s \equiv kr$. With this rescaling we define a parametric operator $F_{\boldsymbol{\alpha}}$ on the Hilbert space:

$$F_{\boldsymbol{\alpha}}[u(s)] = \Big(-\frac{d^2}{ds^2} + \frac{l(l+1)}{s^2} + \frac{2\eta}{s} + U(s;\boldsymbol{\alpha}) - 1\Big)u(s;\boldsymbol{\alpha}) = 0, \tag{5.3}$$

where the re-scaled nuclear potential

$$U(s;\boldsymbol{\alpha}) = V(s/k,\boldsymbol{\omega})2\mu/\hbar^2k^2 \tag{5.4}$$

now effectively depends on the energy. $\boldsymbol{\alpha}$ will represent all of the quantities we wish to emulate across. For neutrons, we emulate across energies and the potential parameters:

$$\boldsymbol{\alpha} \equiv \{\boldsymbol{\omega}, E\}, \tag{5.5}$$

The solutions to Eq. 5.3 can be numerically computed by various methods. We refer to the conventional ways of computing the solution as "high-fidelity solvers" throughout the rest of the manuscript. These include:

- Methods that integrate d^2u/ds^2 in a discretized coordinate basis (r or s), imposing initial conditions at $s \to 0$; these include the Numerov [131] and Runge-Kutta [98, 148] methods.

- Calculable R-matrix methods, which expand $F_{\boldsymbol{\alpha}}$[1] in a convenient pre-selected basis of functions and impose asymptotic boundary conditions at the channel matching radius $s = a$ (see Appendix A.1) [103, 40]. For scattering problems, a basis of Lagrange-Legendre functions is typically employed due to their compact support [11].

We use the implementation of Runge-Kutta in `scipy.integrate.solve_ivp`, as well as the calculable R-matrix method on a Lagrange mesh (see [40, 39, 11, 10]), implemented in the novel software package `JITR`, to generate the results in this chapter [168, 46].

High-fidelity solvers often have control parameters that can be used to tune the precision of the solution obtained, providing a trade-off between accuracy and speed; in the case of the adaptive-step Runge-Kutta implementation in `scipy`, these are the relative and

[1] Really, a modified version of $F_{\boldsymbol{\alpha}}$ that, due to the introduction of the Bloch operator, restores Hermitian symmetry over $s \in [0, a]$.

absolute error tolerances in $u(s)$ used to determine the step Δs. The solver propagates an initial condition of the function and its derivative $\{u(s_0), u'(s_0)\}$ up to a maximum value $s_{\max} = kr_{\max}$, such that the short range potential vanishes $U(s) \approx 0$ for $s \geq s_{\max}$. The starting value $s_0 > 0$ is chosen such that $u(s)$ is well approximated by its power behavior for $s \leq s_0$. In the case of the calculable R-matrix method, it is the truncation of the set of functions that defines the basis. Unless otherwise specified, we use an absolute and relative tolerance of 10^{-9} in `solve_ivp`, and a basis size of 50 in `JITR`.

If we restrict the scaled scattering equation 5.3 to a channel radius $a \equiv kr_{\max}$, the exact solution u exists in an infinite-dimensional Hilbert space[2] $\mathcal{H}$. u exists within a manifold of $\mathcal{H}$ parametrized by all the variables $\boldsymbol{\alpha}$.

The reduced basis method reduces the dimension of this system by exploiting two linear subspaces of $\mathcal{H}$, one to restrict the input of $F_{\boldsymbol{\alpha}}$ (where u resides), and the other to restrict its output [20], through a Galerkin projection [144][3]. By working in these subspaces of smaller dimension n_u, computational efficiency can be significantly increased.

We approximate $u(s)$ by expanding in the reduced basis, which we will seek a suitable representation of:

$$u(s;\boldsymbol{\alpha}) \approx \hat{u}(s;\boldsymbol{\alpha}) = u_0(s) + \sum_{k=1}^{n_u} a_k(\boldsymbol{\alpha}) u_k(s). \tag{5.6}$$

Each channel (jl) will have a different reduced basis, built using the same procedure. We forgo (jl) indices for the remainder of this chapter.

The term $u_0(s)$ is an optional basis element without an assigned coefficient that helps enforce the initial conditions. Such a term is crucial to create a non-homogeneous system of equations for the coefficients $\mathbf{a}$, and avoid obtaining the trivial solution $\hat{u} = 0$. An alternative method is to use the Bloch operator, as in calculable R-matrix methods, which also has the

[2] If we instead consider the entire interval $s \in [0, \infty)$ then the scattering solutions $u(s)$ do not have compact support, and are instead said to exist in a rigged Hilbert space.

[3] Formally, this can be seen as a restriction of the weak formulation of the equations to a subspace of the Hilbert space [121].

advantage of restoring Hermitian symmetry on the Hilbert space of scattering equations within the channel radius [40]. Although the latter is not explored in this work, it is a worthwhile future direction of investigation. We select $u_0(s)$ as a free solution to Eq. 5.3; the Coulomb function $F_l(\eta, s)$ (see Appendix A.1).

The reduced basis can be thought of as a compression of the training set. We do this compression using the principal component analysis (PCA)[4]. The PCA defines a coordinate transformation onto a set of bases which are sequentially ordered by their variance across the training set, referred to as principal components. This can be written as as a matrix decomposition; the singular value decomposition:

$$\mathbf{A} = \mathbf{U} \begin{bmatrix} \ddots & & \\ & s_i & \\ & & \ddots \end{bmatrix} \mathbf{V}^T \tag{5.7}$$

Here, $\mathbf{A}$ is $N \times \mathcal{N}$ matrix of observations, N being the number of observations and $\mathcal{N}$ is the dimension of each observation. These correspond to, respectively, the size of the training set, and the number of elements representing each wavefunction (e.g. in a mesh over the radial coordinate). The principal components are then the columns of $\mathbf{U}$. The fraction of explained variance of each principal component in a PCA decomposition is

$$\frac{\sigma^2_{\text{explained}}}{\sigma^2} = \frac{s_i^2}{\sum_i s_i^2}, \tag{5.8}$$

where s_i are the singular values. These are monotonically decreasing. We choose as our reduced basis the principal components of the difference between the free solution and each element in the "training" set, which is composed of N "snapshots" $u(s; \boldsymbol{\omega}_m)$. Each snapshot is a high-fidelity solutions to Eq. 5.3, each at a different point in parameter space:

[4]The PCA is related to the singular value decomposition algorithm [23], AKA the proper orthogonal decomposition [142].

$$\{u_k\}_{k=1}^{n_u} = \mathrm{PCA}\Big[\{u(s,\boldsymbol{\alpha}_m) - u_0(s)\}_{m=1}^{N}\Big]. \tag{5.9}$$

The PCA captures the n_u directions in which the variance is largest in the training set, corresponding to the variation —caused by the potential— around the "free" solution $u_0(s)$. In practice, n_u can be chosen to preserve some fraction of the explained variance of the training data set using Eq. 5.8.

Once the reduced basis has been constructed, we construct a system of equations for the coefficients $\mathbf{a}$ by selecting the second subspace of $\mathcal{H}$ expanded by "projecting" (or "test") functions ψ_j with $j \in [1, n_u]$. The output of the operator $F_{\boldsymbol{\alpha}}$ is restricted to this subspace, and satisfying Eq. 5.3 (in this subspace) is done by requiring that the projection of the residual $F_{\boldsymbol{\alpha}}[\hat{u}]$ onto each of the ψ_j, for $j \in [1, n_u]$, is zero:

$$\langle \psi_j | F_{\boldsymbol{\alpha}}[\hat{u}] \rangle = \langle \psi_j | F_{\boldsymbol{\alpha}} | u_0 \rangle + \sum_{k=1}^{n_u} a_k \langle \psi_j | F_{\boldsymbol{\alpha}} | u_k \rangle = 0. \tag{5.10}$$

Here we have used that the operator Eq. 5.3 is linear: $F_{\boldsymbol{\alpha}}[\hat{u}] = F_{\boldsymbol{\alpha}}\hat{u}$. We select

$$\psi_j(s) = u_j^{\dagger}(s) \tag{5.11}$$

for the projecting functions, a choice that connects the Galerkin-method approach with scattering emulators based on the Kohn-Variational-Principle [61, 48, 20]. With this choice, a double complex conjugate will cancel in the bras.

In the matrix form, Eq. 5.10 is written:

$$\mathbf{M}(\boldsymbol{\alpha})\mathbf{a} = \mathbf{c}(\boldsymbol{\alpha}), \tag{5.12}$$

where,

$$
\begin{aligned}
M_{jk} &= \langle \psi_j | F_{\boldsymbol{\alpha}} | u_k \rangle = \int \psi_j^\dagger(s) F_{\boldsymbol{\alpha}} u_k(s) ds, \\
c_j &= -\langle \psi_j | F_{\boldsymbol{\alpha}} | u_0 \rangle = -\int \psi_j^\dagger(s) F_{\boldsymbol{\alpha}} u_0(s) ds.
\end{aligned}
\tag{5.13}
$$

These integrals are computed only once in what is called the offline, or training, stage of the emulator. The online stage consists of then using the trained emulator to swiftly give an approximate solution for a new value of the parameters by solving the n_u-dimensional linear system in Eqs. 5.12 [142, 79]. Every computation in the online stage is in the n_u dimensional reduced basis, while the high-fidelity solutions and integrals evaluated offline involve a fine coordinate mesh. For the sake of comparison, we will consider a fine mesh of size $\mathcal{N}$, which characterizes the time complexity of any operation in the high fidelity space. Having $n_u \ll \mathcal{N}$ is the key to achieving a computational speedup.

A demonstration of the principal components for the $^{27}\mathrm{Al}(p,p)$ at 28 MeV test problem are displayed in Fig. 5.1a. This test problem trained an emulator to $^{27}\mathrm{Al}(p,p)$ at 28 MeV. Training points were determined by Latin hypercube sampling using a training range of $\pm 50\%$ around the default Koning-Delaroche (KD) parameters [95]. It is worth noting that the three principal components displayed explain $\sim$99% of the variance on the training set.

5.2 The empirical interpolation method (EIM)

Computing the integrals Eqs. 5.13 for a general unspecified value of the parameters – so that they can be used online – can be done only if the operator $F_{\boldsymbol{\alpha}}$ is affine in those quantities. This is the case for the multiplicative depth parameters for each term in Eq. 2.69, since they factorize from each term into a function that depends on r (or s). This is not the case, however, for the radius R, or diffuseness a for any of the terms, or for the energy for the scaled potential $U(s;\boldsymbol{\alpha})$ in Eq. 5.3. We can recover an affine dependence on $U(s;\boldsymbol{\alpha})$ through the empirical interpolation method (EIM) [7, 73, 142, 79].

When Eq. 5.3 is projected on a grid, $u(s)$ is represented as a vector of size $\mathcal{N}$ while the

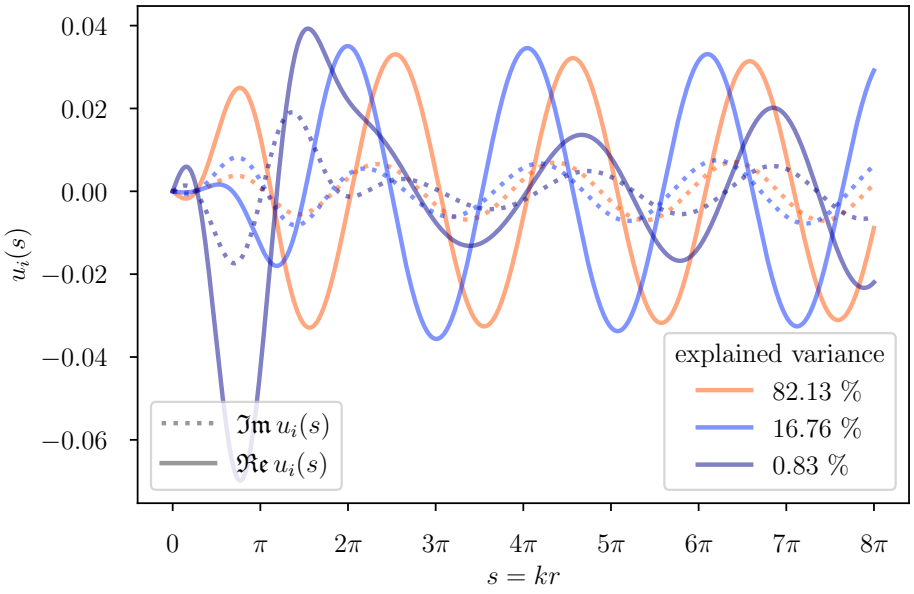

(a) The reduced basis elements $u_k(s)$. Only the first three basis elements are shown, and they are colored and labeled by the fraction of explained variance.

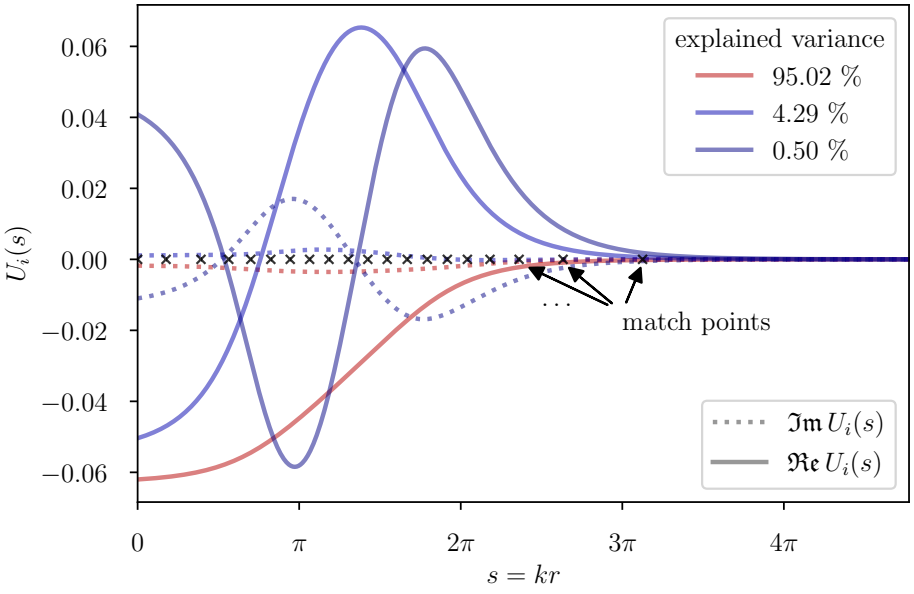

(b) The empirical interpolation method (EIM) basis elements, $U_i(s)$. Only the first three basis elements are shown, and they are colored and labeled by the fraction of explained variance. Also shown as x's are the match points chosen by the MAXVOL algorithm (see text for details).

Figure 5.1: Demonstration of RBM and EIM principal components for the $s_{1/2}$ partial wave at a randomly sampled test point in the ^{27}Al(p,p) at 28 MeV test problem.

potential $U(s;\boldsymbol{\alpha})$ is represented as a matrix of size $\mathcal{N}^2$ (diagonal, in the case of local optical potentials). In the same spirit as Eq. 5.6, we seek a reduced dimensional representation of $U(s;\boldsymbol{\alpha})$ by constructing an approximation through the sum of $n_{EIM} \ll \mathcal{N}^2$ terms:

$$U(s,\boldsymbol{\alpha}) \approx \widehat{U}(s,\boldsymbol{\alpha}) = \sum_{i=1}^{n_{EIM}} b_i(\boldsymbol{\alpha}) U_i(s). \tag{5.14}$$

The s dependence is now only carried by the basis $u_i(s)$; the coefficients $\mathbf{b} \equiv \{b_i(\boldsymbol{\alpha})\}$ are functions only of $\boldsymbol{\alpha}$. This is an *affine decomposition* of a generally non-affine parametric operator.

The basis expansion $u_i(s)$ is computed once during the offline stage. Explicitly, we calculate $N_U \geq n_{EIM}$ potentials $U(s;\boldsymbol{\alpha})$ for N_U values of the parameters $\boldsymbol{\alpha}$, perform a principal component analysis, and retain the n_{EIM} most important components (again chosen to explain some fraction of the variance of the training set):

$$\{U_i(s)\}_{i=1}^{n_{EIM}} = \mathrm{PCA}\Big[\{U(s,\boldsymbol{\alpha}_m)\}_{m=1}^{N_U}\Big]. \tag{5.15}$$

The reduced basis in Eq. 5.15 is computed once offline, but the coefficients $\mathbf{b}(\boldsymbol{\alpha})$ must be determined for every new value of the parameters. The EIM is a prescription for determining these coefficient for a given $\boldsymbol{\alpha}$: by forcing $\widehat{U}(s,\boldsymbol{\alpha})$ to interpolate $U(s,\boldsymbol{\alpha})$, making the approximation Eq. 5.14 exact at exactly n_{EIM} locations s_j:

$$U(s_j,\boldsymbol{\alpha}) - \sum_{i=1}^{n_{EIM}} b_i(\boldsymbol{\alpha}) U_i(s_j) = 0, \quad \text{for } j \in [1, n_{EIM}]. \tag{5.16}$$

To select the locations s_j on which to do the interpolation, we follow the MAXVOL algorithm [70]:

$$\{s_j\}_{j=1}^{n_{EIM}} = \mathrm{MAXVOL}\Big[\{U_i(s)\}_{i=1}^{n_{EIM}}\Big] \tag{5.17}$$

to obtain a "D-optimal" design [123, 129, 122]; in this case, finding the square sub-matrix

of maximum determinant. In general, this is an NP-hard problem [175], however a local optimum can be efficiently identified using the MAXVOL. In practice, this is sufficient to recover a desirable interpolation accuracy. We construct a matrix of size $\mathcal{N} \times n_{EIM}$ in which the columns are the n_{EIM} basis $u(s)$ and the rows are the fine grid over s, of size $\mathcal{N}$, containing all possible candidates s_j. The algorithm seeks to choose the n_{EIM} locations s_j that maximize the determinant of the following reduced $n_{EIM} \times n_{EIM}$ matrix:

$$\mathbf{U}^{\mathrm{EIM}} = \begin{bmatrix} U_1(s_1) & U_2(s_1) & \dots & U_{n_{EIM}}(s_1) \\ U_1(s_2) & U_2(s_2) & \dots & U_{n_{EIM}}(s_2) \\ \vdots & \vdots & \vdots & \vdots \\ U_1(s_{n_{EIM}}) & U_2(s_{n_{EIM}}) & \dots & U_{n_{EIM}}(s_{n_{EIM}}) \end{bmatrix}_{n_{EIM} \times n_{EIM}} \tag{5.18}$$

The algorithm is started by first selecting n_{EIM} locations s_j at random over the grid and then iteratively swapping them for other locations in a greedy fashion by comparing their expansion coefficients [70].

A set of bases of the EIM are shown in Fig. 5.1b for the ^{27}Al(p,p) at 28 MeV test problem. In this case, N_U was 1000, and the number of terms kept in the decomposition for online use was 20. It is worth noting that the three principal components displayed explain over 99% of the variance on the training set. Also displayed are the matching points chosen by MAXVOL. The horizontal axis only goes to $s \approx 4\pi$; MAXVOL chooses points corresponding to the regions in which the training set has it's most variance.

Once the matching locations s_j have been chosen, for a given $\boldsymbol{\alpha}$ the $n_{EIM} \times n_{EIM}$ linear system Eq. 5.16 can be solved for the coefficients $\mathbf{b}(\boldsymbol{\alpha})$. In practice, the inverse of the $n_{EIM} \times n_{EIM}$ matrix formed by $\mathbf{U}^{\mathrm{EIM}}_{ji} \equiv U_i(s_j)$ is pre-computed in the offline stage since it is independent of $\boldsymbol{\alpha}$. In the online stage the exact potential can be evaluated at the interpolation points $c_j^{\mathrm{EIM}}(\boldsymbol{\alpha}) = U(s_j, \boldsymbol{\alpha})$, and the coefficients determined by a simple matrix-vector multiplication:

$$\mathbf{b}(\boldsymbol{\alpha}) = \left(\mathbf{U}^{\mathrm{EIM}}\right)^{-1} \mathbf{c}^{\mathrm{EIM}}(\boldsymbol{\alpha}). \tag{5.19}$$

This determines a realization of the approximate affine decomposition in Eq. 5.14 for a given $\boldsymbol{\alpha}$. An approximate operator $\widehat{F}_{\boldsymbol{\alpha}}$ can then be constructed by substituting the approximation Eq. 5.14 in Eq. 5.3:

$$F_{\boldsymbol{\alpha}} \approx \widehat{F}_{\boldsymbol{\alpha}} = F^{(0)} + \sum_{i=1}^{n_{EIM}} b_i(\boldsymbol{\alpha}) F^{(i)}, \tag{5.20}$$

where $F^{(0)}$ represents the part of the original operator that is independent of the parameters, and $F^{(i)} = U_i(s)$ are the n_{EIM} identified principal components of variations in the part of the operator that depends on the parameters Eq. 5.15. An approximate version of Eq. 5.12 can then be constructed by the projections $\langle \psi_j | \widehat{F}_{\boldsymbol{\alpha}}[\hat{u}] \rangle$:

$$\widehat{\mathbf{M}}(\mathbf{b})\mathbf{a} = \widehat{\mathbf{c}}(\mathbf{b}), \tag{5.21}$$

where now the approximate matrix $\widehat{\mathbf{M}}$ and approximate vector $\widehat{\mathbf{c}}$ consist of the sum of the projections of the $n_{EIM} + 1$ operators in Eq. 5.20 with the test functions ψ_j on the reduced basis U_k, and with the u_0 term, respectively:

$$\begin{aligned} \widehat{\mathbf{M}}(\mathbf{b}) &= \widehat{\mathbf{M}}^{(0)} + \sum_{i=1}^{n_{EIM}} b_i(\boldsymbol{\alpha}) \widehat{\mathbf{M}}^{(i)}, \\ \widehat{\mathbf{c}}(\mathbf{b}) &= \widehat{\mathbf{c}}^{(0)} + \sum_{i=1}^{n_{EIM}} b_i(\boldsymbol{\alpha}) \widehat{\mathbf{c}}^{(i)}. \end{aligned} \tag{5.22}$$

Both quantities are now affine in the coefficients $\mathbf{b}$, and are constructed as:

$$\begin{aligned} \widehat{\mathbf{M}}^{(i)}_{jk} &= \langle \psi_j | F^{(i)} | u_k \rangle = \int \psi_j^\dagger(s) F^{(i)} u_k(s) ds, \\ \widehat{\mathbf{c}}^{(i)}_j &= -\langle \psi_j | F^{(i)} | u_0 \rangle = -\int \psi_j^\dagger(s) F^{(i)} u_0(s) ds. \end{aligned} \tag{5.23}$$

for $i \in [0, n_u]$. All such projections are calculated in the offline stage of the emulator.

In the online stage, when the emulator is deployed and evaluated for a new parameter

$\boldsymbol{\alpha}$, the coefficients in Eq. 5.19 are computed and the approximate matrix and vector are built by summing the pre-computed matrix terms in Eqs. 5.22. Finally, the approximate system of equations 5.21 are solved for the coefficients $\mathbf{a}$ of the reduced basis expansion Eq. 5.6. None of these operations on the online stage scale with the original high dimension size $\mathcal{N}$. Fig. 5.2 demonstrates the effectiveness of the EIM decomposition for the ^{27}Al test problem.

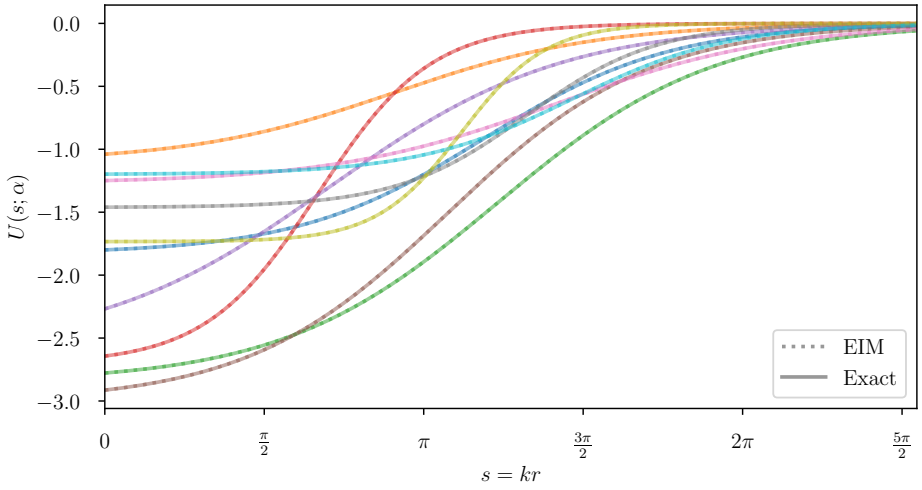

Figure 5.2: Exact coordinate space optical potentials versus empirical interpolation method (EIM) emulated for the ^{27}Al(p,p) at 28 MeV test problem at randomly sampled test points. 20 terms were used in the EIM decomposition, compressed from 1000 training points.

5.3 Results for a local optical potential

We present in this section demonstrations of the effectiveness of the RBM at emulating a high-fidelity solver for problems involving local optical potentials in a limited region of $\boldsymbol{\alpha}$-space. Fig. 5.3 amounts to a spot-check, demonstrating the emulation of the wavefunction and phase-shifts at a randomly chosen point in $\boldsymbol{\alpha}$-space for the previously described ^{27}Al test problem. Agreement is nearly exact, phase shift relative error magnitudes are generally below 1×10^{-4}

Also displayed in Fig. 5.4 are the emulated differential cross sections and analyzing powers for the ^{27}Al test problem, as compared to the high-fidelity solver. Excellent agreement

is obtained.

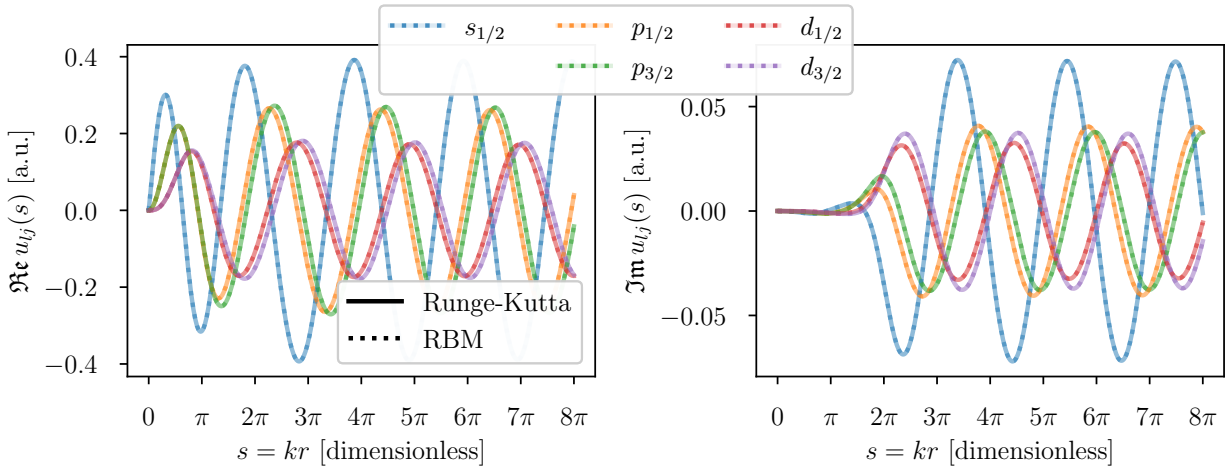

(a) Emulated versus Runge-Kutta wavefunctions at an arbitrary, randomly sampled test parameter not on the training set for ^{27}Al(p,p) at 28 MeV test problem. Excellent accuracy is achieved. The left panels contain the real part of the wavefunctions, while the imaginary parts are on the right.

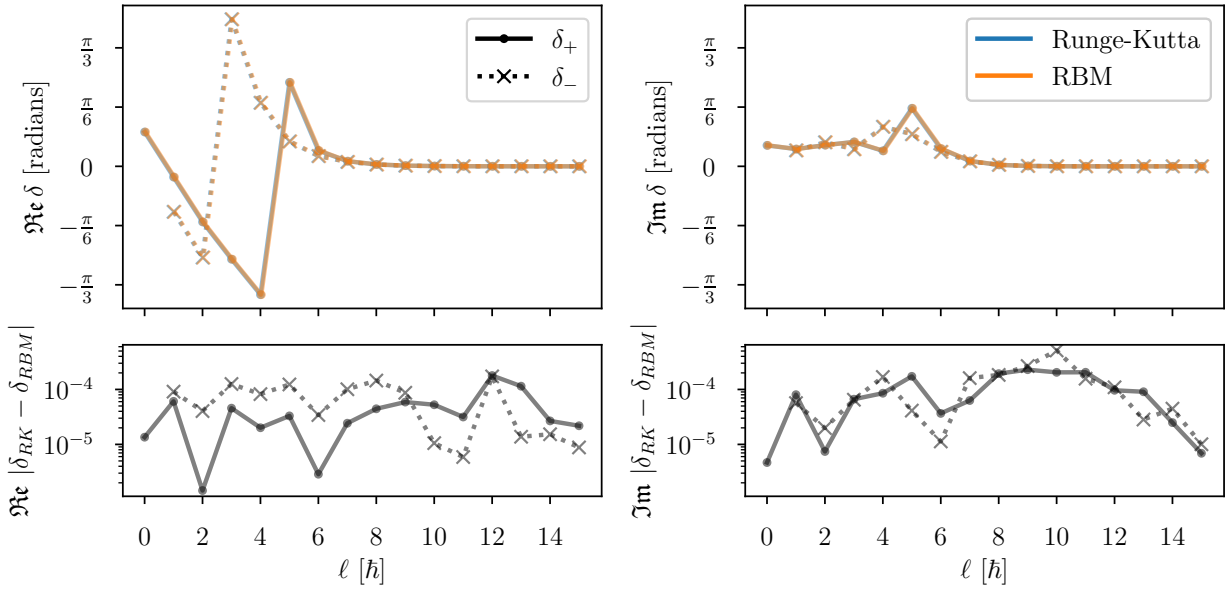

(b) Emulated versus Runge-Kutta phase shifts for an arbitrary, randomly sampled test parameter not on the training set for ^{27}Al(p,p) at 28 MeV test problem. Again, excellent accuracy is achieved; the lines are on top of each other. The magnitude of the relative error is displayed in the lower panels. The left panels contain the real part of the phase shifts, while the imaginary parts are on the right.

Figure 5.3: Spot-check at a random test point for the ^{27}Al(p,p) at 28 MeV test problem. 20 EIM terms were used, paired with a 15-dimensional RBM space.

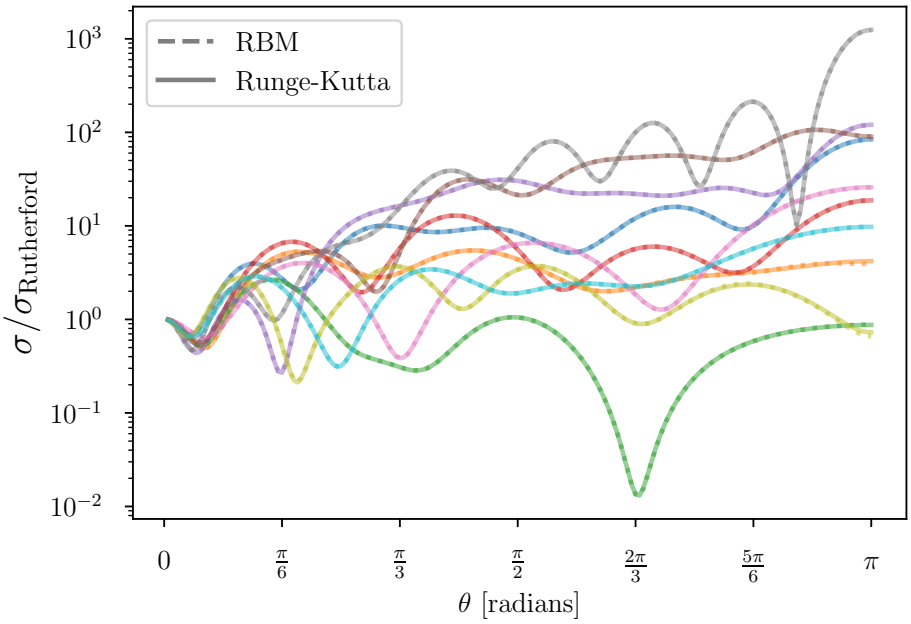

(a) Emulated versus high-fidelity differential scattering cross sections at a set of randomly generated test points.

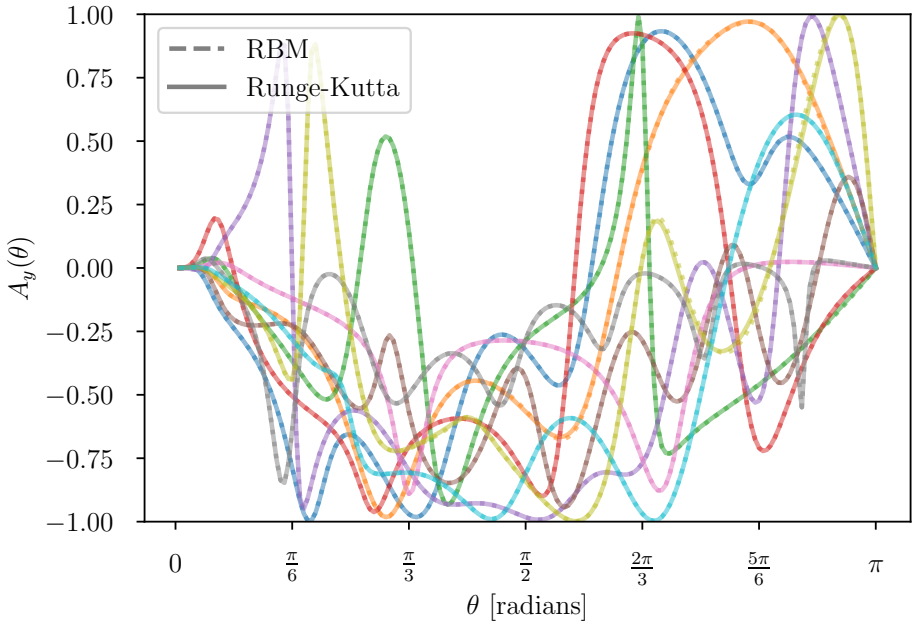

(b) Emulated versus high-fidelity analyzing powers at a set of randomly generated test points.

Figure 5.4: Emulator performance for scattering observables in the ^{27}Al(p,p) at 28 MeV test problem.

The next test problem was ^{40}Ca(n,n) at 14.1 MeV. Again, the training space was constructed by using Latin hypercube sampling within bounds taken as $\pm$50% around the default KD local optical model potential (OMP) parameters. In this case, we conducted a systematic hyper-parameter exploration to determine the optimal basis sizes, n_u and n_{EIM}. Fig. 5.5 displays the results of this computational accuracy vs. time (CAT) analysis, in which multiple RBM configurations are constructed, and compared to a series of Runge-Kutta solvers with varying tolerances. Relative error in differential cross sections on a randomly selected test set is the accuracy metric, where a Runge-Kutta solver with the extremely tight relative and absolute tolerances of 1×10^{-11} is chosen as the "ground truth". The clear conclusion is that the RBM categorically outperforms the Runge-Kutta method, achieving roughly two order of magnitude speedups for the same accuracy.

As the number of wave-function basis n_u and the number of interaction basis n_{EIM} increase, the ROSE calculations become exponentially more accurate. For comparison, `FRESCO` [164], a widely-used production solver requires $\sim$ 30 milliseconds per calculation using standard settings. `JITR` has a similar performance; both are outperformed by the RBM.

Having tested `ROSE`'s performance, we set up the following calibration task as a demonstration, using the same ^{40}Ca(n,n) test problem. We perform a Bayesian calibration to an experimental differential cross section [119], using the default KD parameters as a prior. To accelerate the calibration, based on the performance shown in Fig. 5.5, we select the emulator built with $(n_u, n_{EIM}) = (15, 15)$, since it offers in the worst case an error of 0.1%, which is roughly two orders of magnitudes smaller than the experimental error of $\sim$10%, while still able to perform at $\sim$ 100 samples per second.

To be conservative we set the overall emulator error to 1% across all angles, independent of the value of the parameters, to allow for the emulator performing poorly when the Markov-chain Monte Carlo (MCMC) samples outside of our near the boundaries of the training space.

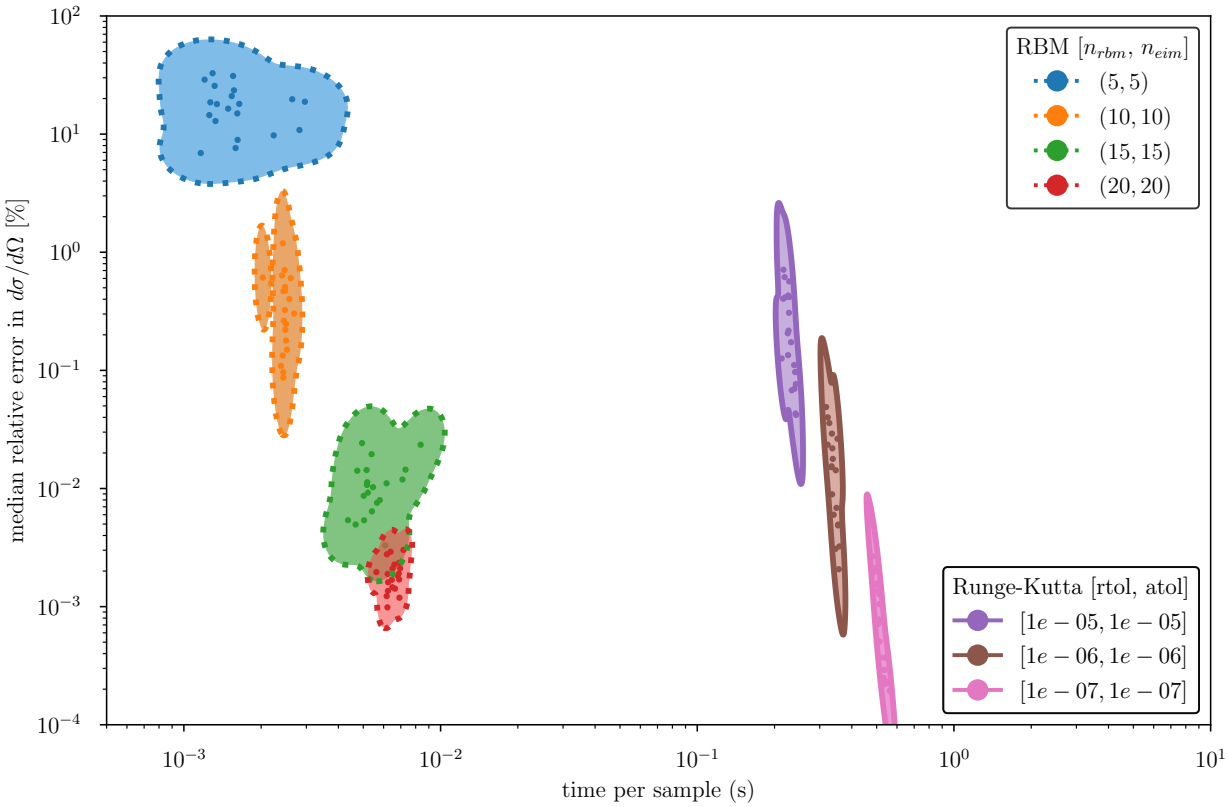

Figure 5.5: The computational accuracy vs. time (CAT) plot for different reduced basis method (RBM) and empirical interpolation method (EIM) configurations for the test problem of optical model differential cross section of ^{40}Ca(n,n) at 14.1 MeV. The vertical axis is the median relative error (across all angles) for each test sample, and compared to Runge-Kutta with absolute and relative tolerances of 1×10^{-11} The horizontal axis represents a configurations mean time to sample. An 2 order of magnitude speedup was achieved while maintaining sub per-mille error.

We choose an independent Gaussian prior distribution for each parameter with mean ω_k^{pr} and standard deviation $0.25\omega_k^{\text{pr}}$, which leads to an overall prior

$$p(\boldsymbol{\omega}) = \prod_{k=1}^{10} p(\omega_k),\ p(\omega_k) \propto \exp\left\{-\frac{1}{2}\frac{(\omega_k - \omega_k^{\text{pr}})^2}{(0.25\omega_k^{\text{pr}})^2}\right\}. \tag{5.24}$$

The calibration of the optical potential parameters was carried out with `surmise`, a Python package—part of the BAND framework [15]—that interfaces Bayesian emulation and calibration [138]. We employ the Metropolis-Hastings algorithm available in `surmise` to sample from the posterior distribution [62].

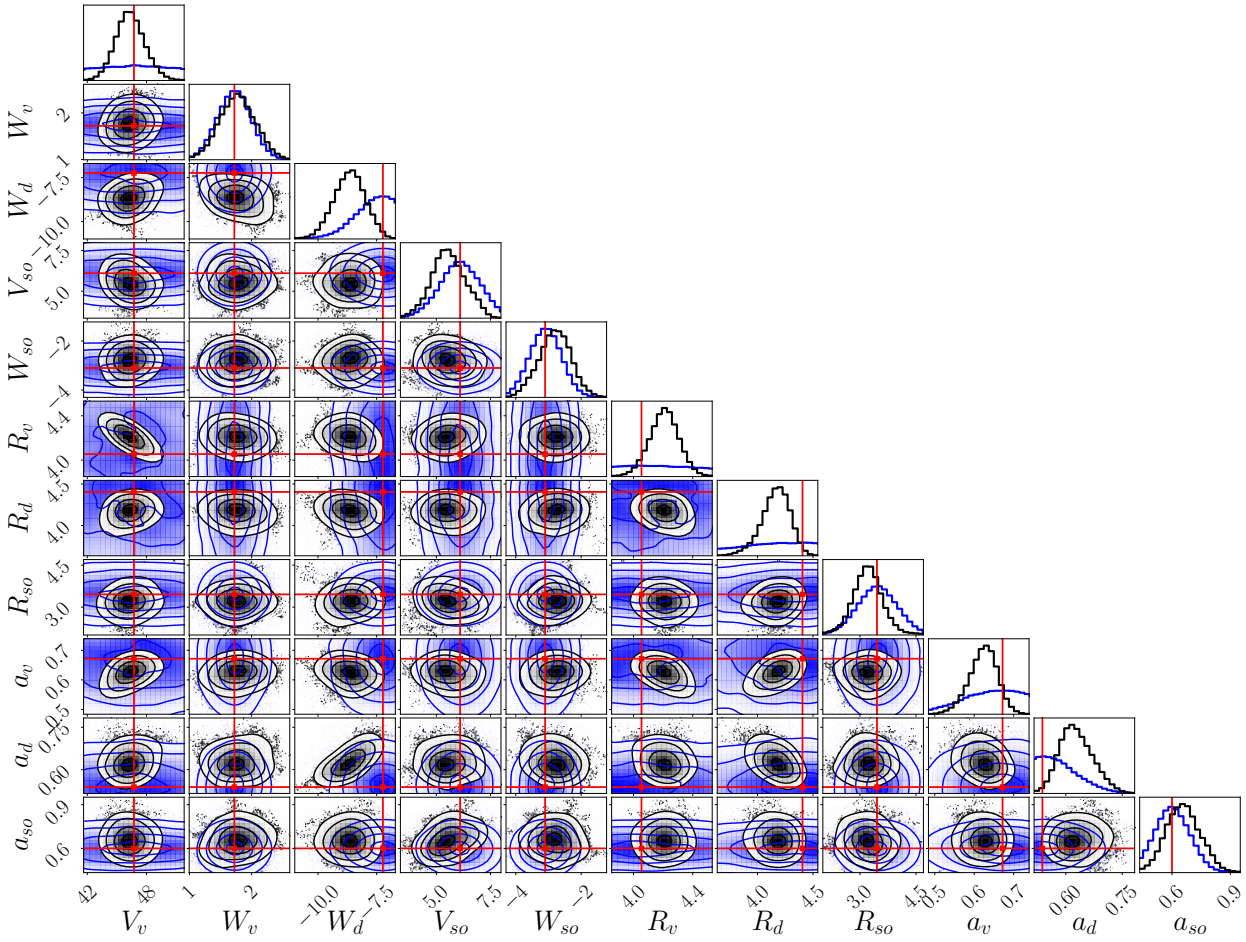

Figure 5.6: Cornerplot [58] for the calibration of the optical model differential cross section of ^{40}Ca(n,n) at 14.1 MeV, calibrated to experimental data from [119]. This plot shows mono- and bivariate marginals of posterior probability distributions, Eq. 5.1. The black histograms represent the posterior Eq. 2.75, approximated by 800,000 samples visited by 5 MCMC walkers; the blue filled contours represent the Gaussian prior Eq. 5.24. The red lines show the values of the true parameters ω^t obtained from [26]. All units of depth terms are in MeV; all radii and diffuseness are in fm.

A total of 40 chains, of 20,000 MCMC samples each, were obtained in just over an hour of wall time on 8 cores of an 3.0 GHz Intel Xeon Gold 6154 processor. Each walker had a burn-in period of n_{burn} = 500 samples, and started randomly within a small region around the prior center to avoid known multi-modal posteriors of the optical potential [81].

Figure 5.6 shows the results of the posterior sampling for neutrons. As has been identified in previous studies, e.g. [109], some parameters are strongly correlated - such

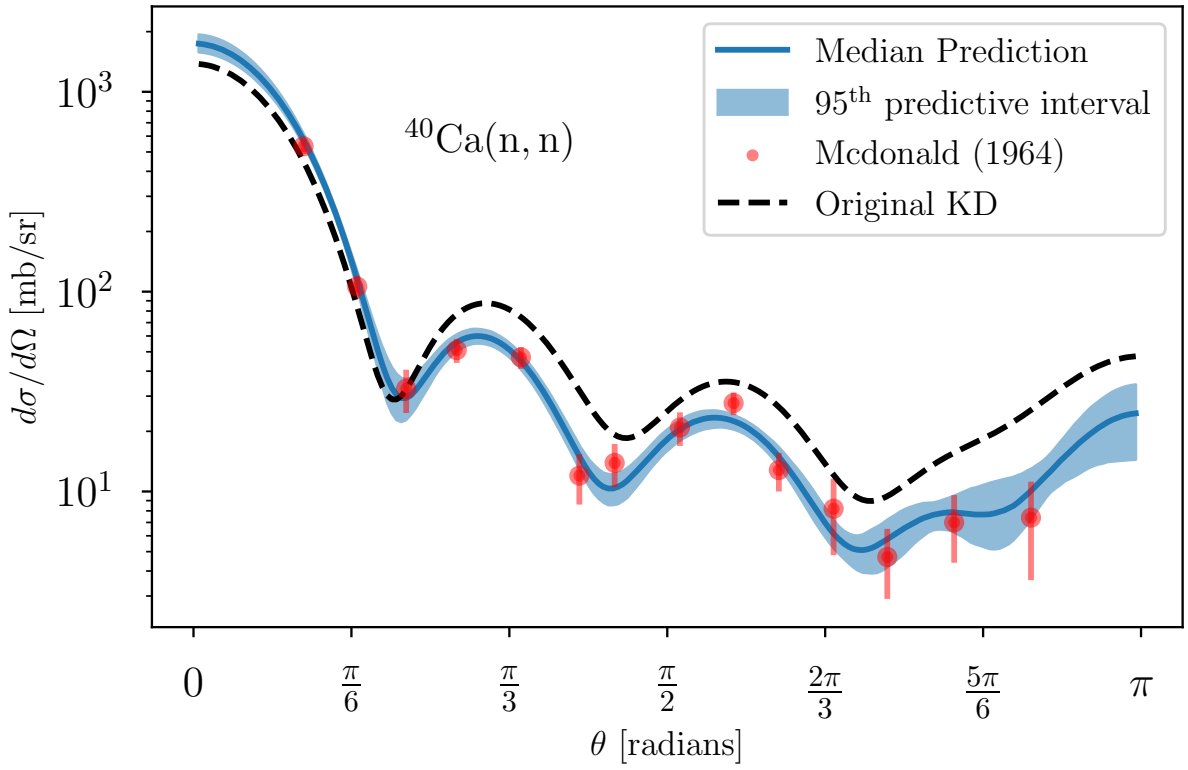

Figure 5.7: Predictive posterior distribution for the differential cross section of ^{40}Ca(n,n) at 14.1 MeV in the laboratory frame, calibrated to experimental data from [119]. The calculation used 800,000 random parameters obtained during the MCMC sampling. The 95% credible interval is calculated using Eq. 2.77 by taking into account the error structure of the data.

as the real volume V_v and real radius R_v, and they display posteriors that are sharply peaked in comparison to the original prior distribution. Meanwhile, the posterior of other parameters, such as the imaginary volume strength W_v, remains close to their prior distribution, not learning much from this specific cross section data at the selected energy. Most of the parameters' true values (red lines) are covered by posterior distribution, with W_d, R_d, and a_{so} being covered just barely by the tails of the distributions. Further Bayesian studies, powered by emulators such as ROSE, on how much the optical parameters can be constrained by data could be particularly relevant for the new rare isotope beams era [75].

Finally, in Fig. 5.7 we show the predictive posterior distribution, calculated through

Eq. 2.77, for ^{40}Ca(n,n). These cross sections were calculated through 800,000 random samples from the visited parameters on the respective posteriors. The 95% credible interval covers the data well, with all red data points covered and a couple of them almost outside the band, indicating a reasonable credibility estimate.

5.4 The active subspace quilting (ASQ)

For the global OMPs, the parameter picture changes slightly. The parameter space we would like to emulate across, $\boldsymbol{\alpha}$, could become, for example:

$$\boldsymbol{\alpha} = \{E, \mu, V_v, R_v, a_v, W_v, R_w, a_w, W_d, R_d, a_d, V_{so}, W_{so}, R_{so}, a_{so}\}, \tag{5.25}$$

.

Each global potential may be different; e.g. Whitehead-Lim-Holt (WLH) uses the same radii and diffuseness for the real and imaginary volume terms. The actual parameters that one would calibrate over are different for each potential as well. Typically they are between roughly 10 – 40 parameters, and a given potential is simply a mapping O, determined by the functional form of the model:

$$\boldsymbol{\alpha} = O(A, Z, E, \boldsymbol{\omega}). \tag{5.26}$$

Thus at each point in the (12-dimensional in the above example) $\boldsymbol{\omega}$-space, we have a map from A, Z, E into $\boldsymbol{\alpha}$-space, which becomes much bigger than in the local example, even for only a single instance of $\boldsymbol{\omega}$ if one wants to emulate across the nuclear chart and over a large energy range.

The RBM method described above works well for problems in which $\boldsymbol{\alpha}$ varies within a small region about some value, e.g. $\bar{\boldsymbol{\alpha}}$. This is because the manifold on which the solutions

trace as a function of $\boldsymbol{\alpha}$ is, in the neighborhood of $\bar{\boldsymbol{\alpha}}$, well described by the span of $\{u_i(s)\}_{i=1}^{n_u}$. In other words, it is *locally linear* in the neighborhood of $\bar{\boldsymbol{\alpha}}$, with *local* dimension n_u. What happens when one tries to leave the neighborhood?

Outside the neighborhood, the actual manifold may flow into a region with a non-negligible component that is orthogonal to $\{u_i(s)\}_{i=1}^{n_u}$, and, therefore, the method will fail. Thus, even if the parametric operator $F_{\boldsymbol{\alpha}}$ is linear at a given point in $\boldsymbol{\omega}$-space, the manifold may be sufficiently non-linear over a large region of space that the method fails. This has been pointed out in the case of both a simple toy model and with a many-body problem of several fermionic particles confined in a harmonic trap [152]. This is also the case for global optical potentials, when one desires to construct an RBM to emulate across the nuclear chart, or over a wide range of energies. One could simply increase the number of dimensions of the RBM, but, to describe a sufficiently large manifold, this quickly defeats the purpose of constructing a surrogate model at all.

The fields of information geometry and manifold learning are concerned with dimensionality reduction for nonlinear manifolds [156, 88]. Perhaps the simplest approach is the local PCA, in which the parameter space is discretized into voxels, and a PCA is done on samples drawn from each voxel. As long as the manifold is smooth, as the voxels get smaller, this clearly learns the linear tangent space in each voxel. This, of course, suffers the curse of dimensionality. More sophisticated methods, like local linear embedding and local tangent space alignment, propose meshless methods that stitch these local tangent spaces together [33, 174, 186]. These methods are suitable for dimensionality reduction of a non-linear dataset, but make no prescription for projective model order reduction; e.g. given a test point in parameter space, finding a local tangent space, and projecting an operator onto it. Work is being done to construct such a local technique, [2], but these methods use a voxel decomposition, and do not extend to very large parameter spaces as in a global OMP.

The active subspace quilting (ASQ) described here is a novel method designed to be

useful in such a situation. The intuitive idea is to randomly select a subset of of the training set as tangent points. For each tangent point, one then constructs an RBM emulator, exactly as described above, using only training points from the local neighborhood (e.g. k nearest neighbors) around the tangent point. For a given test point, one then finds the RBM belonging to its closest tangent point, and uses it to emulate the solution. All of this can be done efficiently using a KD-tree; in this work we use `scipy.spatial.KDtree` [168].

The algorithm for constructing the quilt from a training set is contained in Alg. 1. By choosing a small fraction of variance that must be explained by the preserved principal components, the ASQ method learns the local dimensionality of the full non-linear manifold in each tangent patch. By choosing a number of tangent points n_t and a neighborhood size k such that $n_t \times k > N$, the number of training points, some overlap is guaranteed between the set of training data used to construct the bases for adjacent patches, which should provide some degree of smoothness from patch to patch.

Algorithm 1 Make the patches of the quilt

Given the training set composed of N points $\{\boldsymbol{\alpha}_i\}$, and their associated high-fidelity solutions $\{u(s,\boldsymbol{\alpha}_i)\}$, a neighborhood size k, a subset of the training set defining the set of tangent points, $\mathbb{T} \subset \{\boldsymbol{\alpha}_i\}$, and some desired fraction of explained variance:

for all $\boldsymbol{\alpha}_i \in \mathbb{T}$ **do**
  $\mathbb{T}_i \equiv \{\boldsymbol{\alpha}_j\}_{j=1}^{k} \leftarrow$`findNearestNeighbors`$(\boldsymbol{\alpha}_i, k)$ ▷ find the i^{th} training neighborhood
  $\mathbb{N}_i \equiv \{u_m\}_{m=1}^{n_u} = \mathrm{PCA}\Big[\{u(s,\boldsymbol{\alpha}_j) - u_0(s)\}_{j\in\mathbb{T}_i}\Big]$
  $\mathbb{E}_i \equiv \{U_m(s)\}_{m=1}^{n_{EIM}} = \mathrm{PCA}\Big[\{U(s,\boldsymbol{\alpha}_j)\}_{j\in\mathbb{T}_i}\Big]$
end for

Here, we have implicitly assumed that n_u and n_{EIM} are chosen for each tangent point to reproduce the expected variance fraction in $\{\boldsymbol{\alpha}_j\}_{j=1}^{k}$. $\mathbb{T}_i$ defines the i^{th} training neighborhood; the set of k points closest to the i^{th} tangent point. The result is the set of of neighborhood bases $\mathbb{N}_i$, and neighborhood EIM bases, $\mathbb{E}_i$, at each tangent point i. This completes the offline stage. In the online stage, given a test point $\boldsymbol{\alpha}_k$, one simply uses `findNearestNeighbors` to find nearest tangent point; e.g. $\arg\min\left[|\boldsymbol{\alpha}_k - \boldsymbol{\alpha}_i|^2\right]_{i=0}^{N}$, and then the emulation proceeds

exactly as described in the previous sections.

However, there is no guarantee that the nearest tangent space will actually embed the test point, or that the nearest neighbors to the tangent point on the training space will form a suitably low-dimensional linear tangent space at all. This is addressed by defining the nearest neighbor to be that, not on the parameter space, but the *active subspace*. The active subspace, introduced by Constantine et al., is the span of the largest L principal components of the gradient of some scalar function of $\boldsymbol{\alpha}$ [36]. We adapt this idea here to come up with a new distance metric, rather than $|\boldsymbol{\alpha}_k - \boldsymbol{\alpha}_i|^2$, that better approximates the geodesic distance on the full manifold.

We choose as our scalar response of interest, the functional

$$\mathcal{F}_{\boldsymbol{\alpha}}\left[u(s;\boldsymbol{\alpha})\right] \equiv \langle \psi_j | F_{\boldsymbol{\alpha}}[u(s;\boldsymbol{\alpha})]\rangle \,. \tag{5.27}$$

We define the gradient of $\mathcal{F}$ in $\boldsymbol{\alpha}$-space as a Gateaux derivative. Along some unit direction $\hat{\boldsymbol{\alpha}}$:

$$(\nabla_{\boldsymbol{\alpha}} \cdot \hat{\boldsymbol{\alpha}})\ \mathcal{F}_{\boldsymbol{\alpha}}\left[u(s,\boldsymbol{\alpha})\right] = \lim_{\delta\to 0} \frac{\mathcal{F}_{\boldsymbol{\alpha}}\left[u(s,\boldsymbol{\alpha}+\delta\hat{\boldsymbol{\alpha}})\right] - \mathcal{F}_{\boldsymbol{\alpha}}\left[u(s,\boldsymbol{\alpha})\right]}{\delta}. \tag{5.28}$$

Because $\mathcal{F}_{\boldsymbol{\alpha}}$ is identically 0 when it takes as input $u(s,\boldsymbol{\alpha})$, the second term in the numerator disappears. Defining $\boldsymbol{\alpha}' = \boldsymbol{\alpha} + \delta\hat{\boldsymbol{\alpha}}$, the numerator reduces like so:

$$\begin{aligned} \mathcal{F}_{\boldsymbol{\alpha}}\left[u(s;\boldsymbol{\alpha}')\right] &= \left\langle u^\dagger(s;\boldsymbol{\alpha}') \middle| \left(-\frac{d^2}{ds^2} + \frac{l(l+1)}{s^2} + \frac{2\eta}{s} + U(s;\boldsymbol{\alpha}) - 1\right) \middle| u(s;\boldsymbol{\alpha}')\right\rangle. \\ &= \left\langle u^\dagger(s;\boldsymbol{\alpha}') \middle| U(s;\boldsymbol{\alpha}) - U(s;\boldsymbol{\alpha}') \middle| u(s;\boldsymbol{\alpha}')\right\rangle \end{aligned} \tag{5.29}$$

For δ finite, this is a simple forward difference formula for two nearby points $\boldsymbol{\alpha}$ and $\boldsymbol{\alpha}'$, in terms of the matrix element of the difference in the interaction at those two points. Alg. 2 is the method used to approximately discover the active subspace. In practice, the entire sparse matrix $\left(\nabla_{\boldsymbol{\alpha}} \cdot \widehat{\boldsymbol{\alpha}_j - \boldsymbol{\alpha}_i}\,\mathcal{F}\right)_{ij}$ is never stored, it is only needed one block at a

time. The output is the approximate gradient, $(\nabla_{\boldsymbol{\alpha}}\mathcal{F})_i$, and the maximum finite difference, $\left(\nabla_{\boldsymbol{\alpha}} \cdot \widehat{\boldsymbol{\alpha}_j - \boldsymbol{\alpha}_i}\, \mathcal{F}\right)_{i,\max}$ at each training point.

Algorithm 2 Discover the active subspace

Given the training set N points $\mathbb{T} \equiv \{\boldsymbol{\alpha}_i\}$, their associated high-fidelity solutions $\{u(s, \boldsymbol{\alpha}_i)\}$, and a neighborhood size k:

for all $\boldsymbol{\alpha}_i \in \mathbb{T}$ **do**
  $\mathbb{T}_i \equiv \{\boldsymbol{\alpha}_j\}_{j=1}^{k} \leftarrow$`findNearestNeighbors`$(\boldsymbol{\alpha}_i, k)$

  for all $\boldsymbol{\alpha}_j \in \mathbb{T}_i$ **do**
    $\left(\nabla_{\boldsymbol{\alpha}} \cdot \widehat{\boldsymbol{\alpha}_j - \boldsymbol{\alpha}_i}\, \mathcal{F}\right)_{ij} \leftarrow \left\langle u^{\dagger}(s;\boldsymbol{\alpha}_j) \,\middle|\, U(s;\boldsymbol{\alpha}_i) - U(s;\boldsymbol{\alpha}_j) \,\middle|\, u(s;\boldsymbol{\alpha}_j) \right\rangle / |\boldsymbol{\alpha}_j - \boldsymbol{\alpha}_i|$
    $\boldsymbol{\alpha}^{\star} \leftarrow \arg\max \left[\left(\nabla_{\boldsymbol{\alpha}} \cdot \widehat{\boldsymbol{\alpha}_j - \boldsymbol{\alpha}_i}\, \mathcal{F}\right)_{ij} \right]_{j=0}^{k}$
    $\left(\nabla_{\boldsymbol{\alpha}} \cdot \widehat{\boldsymbol{\alpha}_j - \boldsymbol{\alpha}_i}\, \mathcal{F}\right)_{i,\max} \leftarrow \max \left[\left(\nabla_{\boldsymbol{\alpha}} \cdot \widehat{\boldsymbol{\alpha}_j - \boldsymbol{\alpha}_i}\, \mathcal{F}\right)_{ij} \right]_{j=0}^{k}$
    $(\nabla_{\boldsymbol{\alpha}}\mathcal{F})_i \leftarrow \widehat{\boldsymbol{\alpha}^{\star} - \boldsymbol{\alpha}_i}$
  end for

end for

The singular value decomposition of the $N \times m$ matrix $(\nabla_{\boldsymbol{\alpha}}\mathcal{F})_i$, m being the number of dimensions of the parameter space, is:

$$\begin{bmatrix} & | & \\ \cdots & (\nabla_{\boldsymbol{\alpha}}\mathcal{F})_i & \cdots \\ & | & \end{bmatrix} = \mathbf{U} \begin{bmatrix} \ddots & & \\ & s_i & \\ & & \ddots \end{bmatrix} \mathbf{V}^T \tag{5.30}$$

where s_i are the singular values.

We define the $m \times m$ transformation matrix:

$$\boldsymbol{\Lambda} \equiv \mathbf{U} \begin{bmatrix} \ddots & & \\ & s_i & \\ & & \ddots \end{bmatrix}. \tag{5.31}$$

$\boldsymbol{\Lambda}$ defines a transformation in coordinate space: a rotation unto the principal directions

of the gradient of $\mathcal{F}$, and a stretching by the singular value of each principal component, corresponding to the variance in the gradient $\mathcal{F}$ along that principal component. $\mathbf{\Lambda}$ defines a new distance metric, the *active subspace distance*:

$$|\boldsymbol{\alpha}_i - \boldsymbol{\alpha}_j|_{AS}^2 \equiv (\boldsymbol{\alpha}_i - \boldsymbol{\alpha}_j)^T \mathbf{\Lambda}^T \mathbf{\Lambda} (\boldsymbol{\alpha}_i - \boldsymbol{\alpha}_j). \tag{5.32}$$

By implementing `findNearestNeighbors` using the active subspace distance, one then finds the closest tangent point to a given test point on the active subspace, rather than the parameter space. This tangent point will be that with the most similar response $\mathcal{F}$, and, therefore, the most suitable RBM with which to emulate solutions.

5.5 Results for a global optical potential

An active subspace quilting (ASQ) was constructed for the Koning-Delaroche uncertainty quantified (KDUQ) potential for neutrons incident on 46 stable or near-stable isotopes in the atomic number region of the fission fragments, from energies of 100keV to 10MeV. 1000 training points were used, with 200 tangent points amongst them. The neighborhood size was chosen to be $k = 50$. The fraction of explained variance was chosen to be 1.0×10^{-9}, which resulted in n_u and n_{EIM} to range between 10-20 in each patch. The tangent points were sampled by according to the $\left(\nabla_{\boldsymbol{\alpha}} \cdot \widehat{\boldsymbol{\alpha}_j - \boldsymbol{\alpha}_i}\, \mathcal{F}\right)_{i,\max}$ so that tangent patches are biased towards regions of high variation on the full manifold. In practice, rather than constructing a separate quilt for each partial wave, the same quilt structure is used, with a set of RBM emulators at each patch, one for each partial wave.

The parameter space was centered and scaled before the active subspace discovery. Because multiple orders of magnitude of energy are covered, sampling was performed in $\log(E)$-space. Fig. 5.8 displays the explained variance of each principal component of the discovered active subspace, as well as the first few columns of $\mathbf{\Lambda}$. The first component is fairly aligned in the direction of the scattering energy; from the figure, the active subspace

distance between two points nearby in energy will be $\sim 15\times$ the actual distance in the (centered and scaled parameter space).

Differential and total cross sections for ^{137}Ba(n,n) over the energy range were emulated and compared to high-fidelity solutions as a test problem for the ASQ. The results are displayed in Figs. 5.9 and 5.10. Of the 200 tangent points in the training space, the test problem over the whole energy range only used six. This emphasizes the sheer volume in parameter space global OMPs cover as compared to local ones, and the degree of difficulty in emulating across such large spaces. Still, with only six tangent patches, reasonable agreement is obtained to the high fidelity solutions. Typically, a speedup of at least two orders of magnitude was achieved relative to the high-fidelity solver. This indicates the online computational expense of the ASQ is essentially same as a single RBM; the nearest-neighbor lookup adds negligible overhead. Of course, the ASQ requires much more time to train; roughly 40 minutes on commodity hardware for this test case.

This encapsulates the formulation, construction and demonstration of a novel PMOR technique for non-linear parameter spaces and large manifolds. It is underpinned by the use of the active subspace metric to determine the similarity in the local linear span of the manifold between two points. This method is shown to be effective in emulating a global optical potential across a large parameter space. However, and perhaps predictably, it does not always compare favorably in accuracy to the single RBM for a local potential. Still, this represents a significant step towards emulating global optical potentials, and in general parametric system with non-linear latent manifolds.

In tests, the ASQ displayed sensitivity to the location of tangents. While the biased sampling towards regions of high variability in $\mathcal{F}$ significantly ameliorates this issue, when the number of tangent points is $\sim$ 100, a single random choice of tangent points from the training space introduces a degree of noise to the accuracy. Increasing the number of tangent points past a few hundred can become memory constrained on commodity hardware, depending on the neighborhood size, n_u, and n_{EIM}. Iterative methods where

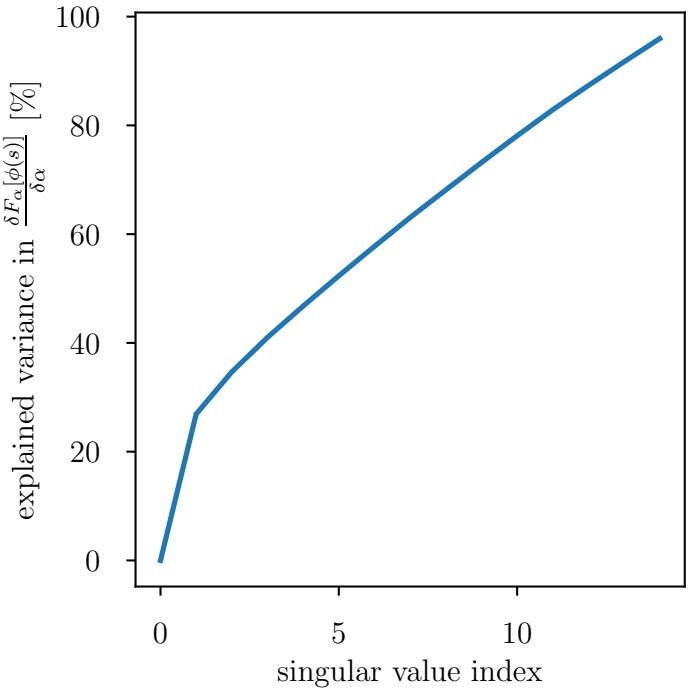

(a) The fraction of variance explained by each principal component of the active subspace. The lack of convergence indicates that the active subspace is not necessarily useful for *compression*, but it is useful to define a distance metric, Eq. 5.32

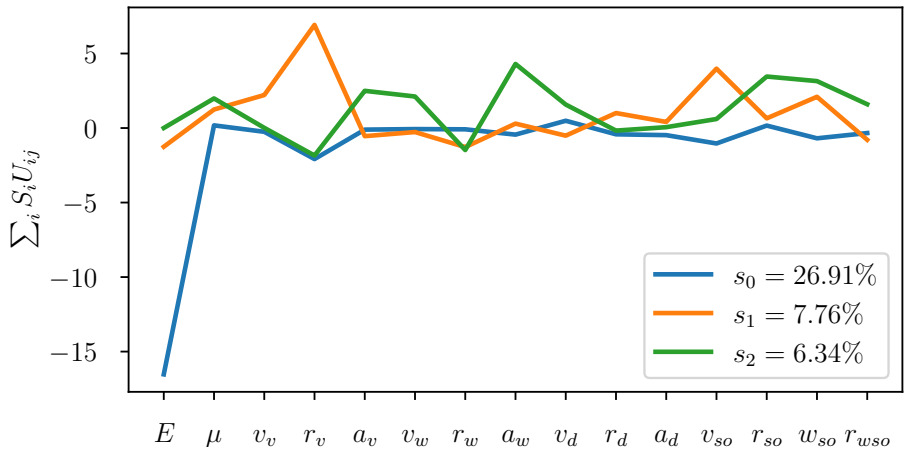

(b) The first few principal components of the active subspace, or, equivalently, columns in the transformation matrix $\mathbf{\Lambda}$ (see Eq. 5.31), labeled by the percentage of variance they explain. Interestingly, the scattering energy E is prominently featured in the first principal component, indicating a large degree of variance in $\mathcal{F}$ in the direction of E in parameter space.

Figure 5.8: The discovery of the active subspace

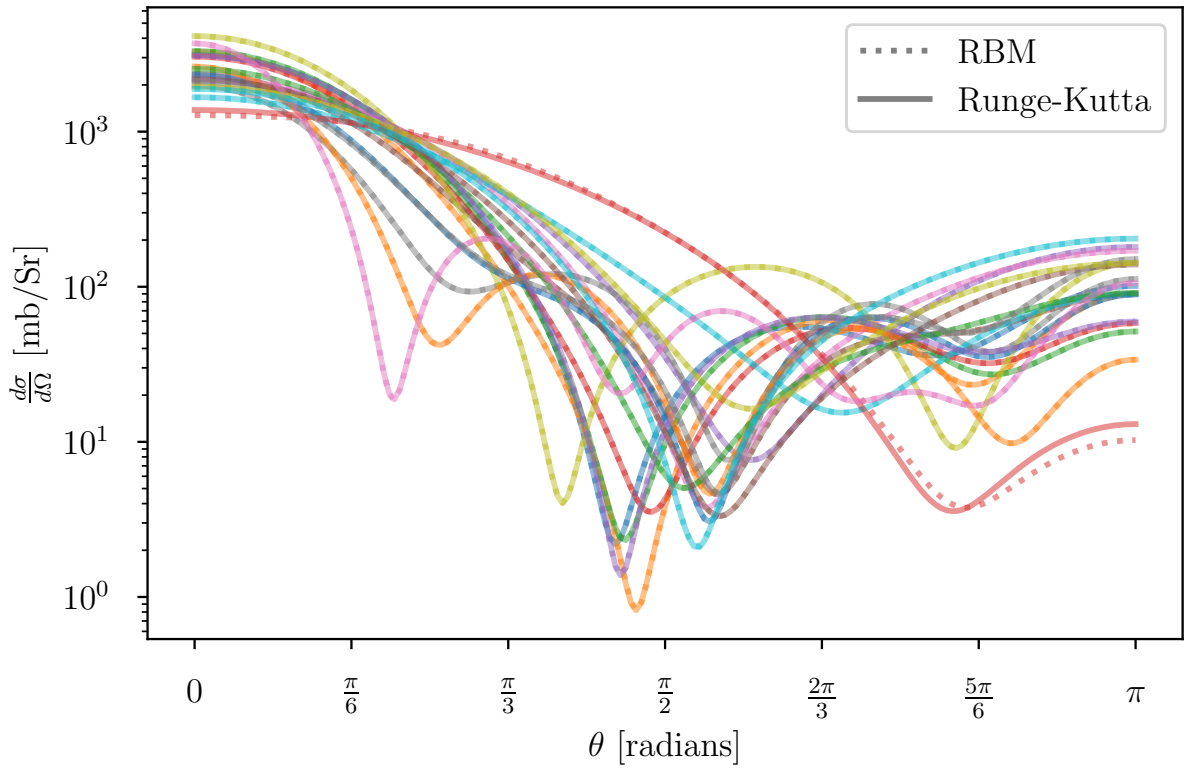

Figure 5.9: Emulated differential cross sections for $^{137}\mathrm{Ba}(n,n)$ using the ASQ compared to a high-fidelity solver. Generally good agreement is achieved.

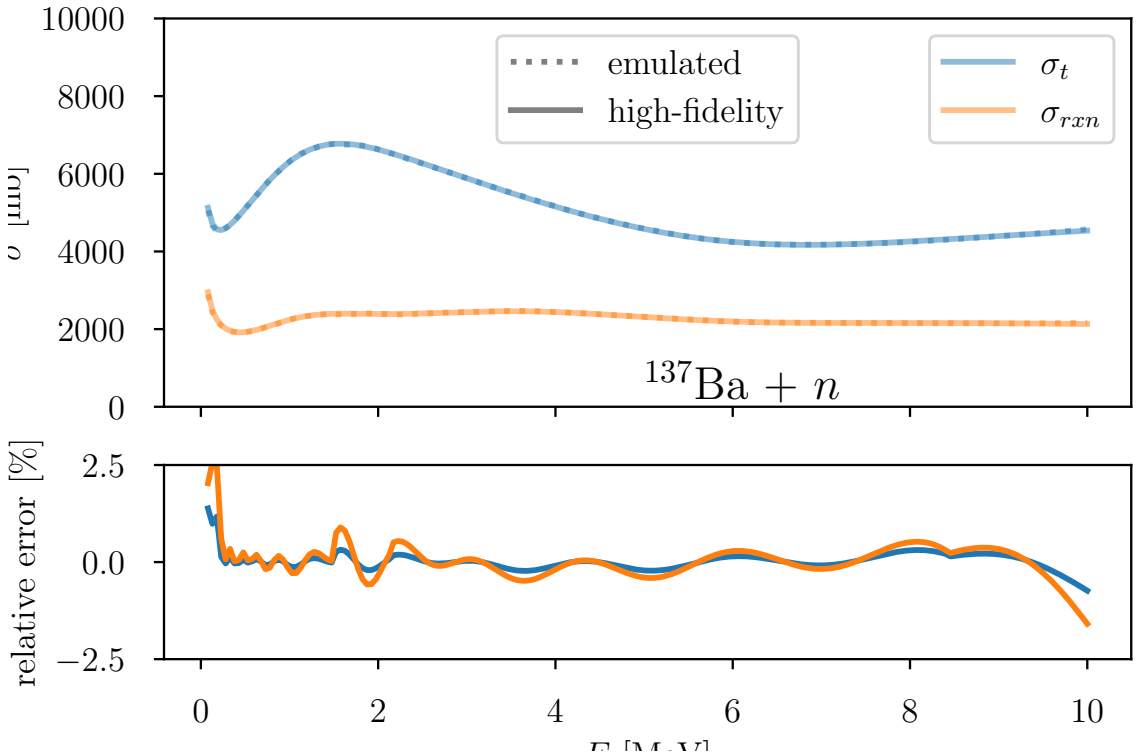

Figure 5.10: Emulated total and reaction cross sections for ^{137}Ba(n,n) using the ASQ compared to a high-fidelity solver. Agreement to within a few percent is achieved near the energy bounds, with sub-percent accuracy achieved over most of the domain.

multiple random samplings could be explores, but this could add significant training cost. Alternatively, exploring the use of a greedy algorithm, similar to MAXVOL, to choose tangent points, is worth exploring. Finally, this method introduces further hyper-parameters in the neighborhood size, k and number of tangent points. Exploring the sensitivity to these, or, better yet, determining systematics for choosing them, is a reasonable next step.

Future work will incorporate these emulators into an Monte Carlo Hauser-Feshbach (MCHF) code. This has the potential to significantly alleviate the computational burden of modeling compound nucleus (CN) de-excitation, making calibration of OMP parameters to fission observables tractable.

Chapter 6

Conclusions and a Path Forward

In Chapters 3 and 4 in this work we have compiled a new corpus of experimental data, one unfamiliar to optical potentials, including observables from nuclear fission, and neutron stars. We explore the use of these data sets as constraints and consistency checks in the context of two modern, uncertainty-quantified potentials; one phenomenological and constrained by a large corpus of tradition optical model potential (OMP) observables (differential elastic and angle-integrated total and reaction cross sections), the other from a microscopic nuclear-matter approach, and constructed from chiral forces consistent with quantum chromodynamics.

In Chapter 3, We showed that fission observables, especially those correlating neutron energies with fragment mass and/or energy, are strongly sensitive to the optical potential parameters, an encouraging result for the prospect of using them as constraints. However, this optimism should be tempered with the following considerations: 1) Monte Carlo Hauser-Feshbach (MCHF) simulations of fission fragment de-excitation are strongly sensitive to multiple model inputs, especially those relating to the initial fission fragment state following scission but before prompt emission (e.g. excitation energy sharing), and 2) the computational cost of performing the uncertainty quantification was significant, and scaling up to a full calibration using the current version of CGMF would be intractable.

In Chapter 4, we have confronted the two uncertainty-quantified optical potentials considered in this work with experimental constraints on their symmetry dependence. We find that the phenomenological model generally disagrees with them, to statistical significance. This points to the limitations of scattering observables in the valley of stability at constraining isospin dependence. Moving forward, we recommend the use of judiciously chosen constraints, or at least consistency checks, from measurements of the nuclear matter symmetry energy. The analytic constraints for (approximate) Lane-consistency, like those used in the original Koning-Delaroche parameterization (see [95] Eq. 20), clearly improve agreement with the microscopic nuclear matter approach, and work should be done to incorporate constraints like this into future Bayesian calibration.

The prospect of introducing new observables into such calibrations, especially the fission observables from Chapter 3, strongly motivate the need for effective surrogate models, in particular for fission fragment de-excitation. The nuclear physics field has recently embraced model order reduction, in particular projective techniques which are constrained by the underlying physics of the system being emulated. In Chapter 5, we present our work applying the reduced basis method (RBM) to develop a fast emulator for local optical potentials. Then, we take the first step to extend this technique to global optical potentials using the novel active subspace quilting (ASQ) method.

This work elucidates several potentially fruitful directions of future exploration. In Chapter 3, we have also identified in specific neutron-fragment correlated observables that are *not* strongly sensitive to the optical potential, that we recommend including in ongoing work globally optimizing model inputs relating to fission fragment initial conditions in CGMF [111]. Any calibration of an OMP will have to carefully select observables to carefully manage correlation with other model inputs. We also call for a renewed experimental effort to measure fission fragnment-neutron correlations using a fission arm spectrometer, for enhanced mass, charge and energy resolution.

Further exploration of enforcing consistency with nuclear matter symmetry energy

measurements presented in Chapter 4 in a Bayesian approach are warranted. One strategy is to sample the real volume isovector potential parameters from the experimentally constrained region(s) displayed in Fig. 4.3 [105], or even include them as constraints in the likelihood function. More advanced approaches could apply a nuclear matter "unfolding" to phenomenological potentials for finite nuclei, using microscopic nuclear density distributions.

Further, the need for incorporating constraints from bound states, especially below the Fermi energy, is emphasized. Additionally, analytic constraints provided by the dispersion relation, which is a consequence of time-ordering the particle-hole excitations that make up the optical potential $\mathbb{Q}$-space, have been demonstrated for local optical potentials. Extending this to cover the nuclear chart in an uncertainty-quantified fully non-local potential that connects bound and scattering states is the recommended path forward.

Finally, the work presented in Chapter 5 just scratches the surface of applications for fast and accuate emulators for nuclear reactions. Work is underway to extend this approach to reactions other than elastic scattering. Specifically, future work will incorporate this into a Hauser-Feshbach calculation of compound nuclear observables. This technique also has the potential to provide significant speedups for general applications of Monte-Carlo Hauser-Feshbach codes.

The constraints and consistency checks for optical potentials proopsed here are especially important in the context of the multi-modality of the OMP. The construction of a unique and unambiguous optical potential constrained by many orthogonal quantities, including both scattering observables and bound states, provides a sturdier vessel on which to venture beyond the valley of stability.

Acronyms

Acronym	Description	Page List
χ-EFT	chiral effective field theory	2, 38
`mpi4py`	MPI for Python	48
ASQ	active subspace quilting	vii, xii, 10, 75, 93, 94, 98, 99, 101, 102, 105, 107
CAT	computational accuracy vs. time	xi, 89, 90
CLT	Central Limit Theorem	47
CN	compound nucleus	9, 26–29, 41–43, 46, 63, 64, 103, 107
COM	center-of-mass	ix, x, 14, 29, 43, 47, 54, 56, 61, 62, 107
DOM	dispersive optical model	21, 107
EIM	empirical interpolation method	vii, x, xi, 81–83, 86, 87, 90, 95
EOS	Equation-of-State	65, 66, 107
FPY	fission product yield	viii, 2, 4
HF	Hauser-Feshbach	42, 64
I-LDA	improved local density approximation	38
KCK	Kawano-Chiba-Koura	46
KD	Koning-Delaroche	2, 3, 46, 68, 69, 81, 89

Acronym	Description	Page List
KDUQ	Koning-Delaroche uncertainty quantified	vi, x, 3, 9, 11, 31, 36–39, 41, 46, 49, 65–73, 98
MBPT	many-body perturbation theory	38
MCHF	Monte Carlo Hauser-Feshbach	7, 30, 40, 41, 44–47, 49, 56, 64, 75, 103, 104
MCMC	Markov-chain Monte Carlo	89
MPI	Message Passing Interface	48, 107
OMP	optical model potential	viii, x, 1–3, 7–9, 21, 26, 30, 32, 33, 35–37, 40–47, 49–52, 54–56, 63, 64, 72, 89, 93, 94, 99, 103–107
PCA	principal component analysis	79, 80, 107
PFNS	prompt fission neutron spectrum	viii, ix, 7, 47–49, 51, 52, 54, 57, 58
PMOR	projective model order reduction	8, 74, 75, 99
QCD	quantum chromodynamics	2, 3, 34, 38
QRPA	quasi-particle random phase approximation	44
RBM	reduced basis method	vii, x, xi, 8, 10, 74–76, 82, 86, 87, 89, 90, 93–95, 98, 99, 105, 107
SEM	standard error in the mean	47

Acronym	Description	Page List
TKE	total kinetic energy	ix, x, 45, 51–56, 59–62, 64
TXE	total excitation energy	45
WLH	Whitehead-Lim-Holt	vi, x, 2, 3, 9, 11, 31, 34, 38, 39, 41, 46, 49, 51, 52, 55, 63, 65–73, 93

Software

ROSE

A Python software package to which the authors contributed using the Reduced Basis Method to emulate few-body nuclear reactions for uncertainty-quantification [134]. 10, 74, 75, 89

CGMF

A C++ and Python software package from Los Alamos National Laboratory for modeling nuclear fission using the Monte Carlo Hauser-Feshbach framework [160]. A modified version by the authors was used in this work.. viii, 4, 7, 36, 40, 41, 45–48, 75, 104, 105

JITR

A Python software package by the authors that uses just-in-time (JIT) compilation to calculate reaction observables using the calculabe R-matrix method on a Lagrange-Legendre mesh with high performance [13] . 74, 77, 78, 89

omp-uq

A Python framework by the authors for driving the uncertainty propagation of optical potentials into fission observables described in this work . 48

OSIRIS

A Python package by the authors for uncertainty-quantification of few-body reaction observables [14] . 48, 49

Bibliography

[1] B. P. Abbott et al. "GW170817: Observation of Gravitational Waves from a Binary Neutron Star Inspiral". In: *Phys. Rev. Lett.* 119 (16 Oct. 2017), p. 161101. DOI: 10.1103/PhysRevLett.119.161101. URL: https://link.aps.org/doi/10.1103/PhysRevLett.119.161101.

[2] David Amsallem, Matthew J Zahr, and Charbel Farhat. "Nonlinear model order reduction based on local reduced-order bases". In: *International Journal for Numerical Methods in Engineering* 92.10 (2012), pp. 891–916.

[3] Peter Anninos et al. "Relativistic tidal disruption and nuclear ignition of white dwarf stars by intermediate-mass black holes". In: *The Astrophysical Journal* 865.1 (2018), p. 3.

[4] Iair Arcavi et al. "Optical emission from a kilonova following a gravitational-wave-detected neutron-star merger". In: *Nature* 551.7678 (2017), pp. 64–66.

[5] MC Atkinson et al. "Dispersive optical model analysis of Pb 208 generating a neutron-skin prediction beyond the mean field". In: *Physical Review C* 101.4 (2020), p. 044303.

[6] T Aumann et al. "Quenching of single-particle strength from direct reactions with stable and rare-isotope beams". In: *Progress in Particle and Nuclear Physics* 118 (2021), p. 103847.

[7] Maxime Barrault et al. "An 'empirical interpolation' method: application to efficient reduced-basis discretization of partial differential equations". In: *C. R. Math.* 339.9 (2004), pp. 667–672. DOI: https://doi.org/10.1016/j.crma.2004.08.006.

[8] OA Batenkov et al. "Prompt Neutron Emission in the Neutron-Induced Fission of 239Pu and 235U". In: *AIP Conference Proceedings*. Vol. 769. 1. American Institute of Physics. 2005, pp. 1003–1006.

[9] E Bauge, JP Delaroche, and M Girod. "Lane-consistent, semimicroscopic nucleon-nucleus optical model". In: *Physical Review C* 63.2 (2001), p. 024607.

[10] Daniel Baye. "Lagrange-mesh method for quantum-mechanical problems". In: *physica status solidi (b)* 243.5 (2006), pp. 1095–1109.

[11] Daniel Baye. "The Lagrange-mesh method". In: *Physics reports* 565 (2015), pp. 1–107.

[12] JS Bell and EJ Squires. "A formal optical model". In: *Physical Review Letters* 3.2 (1959), p. 96.

[13] Kyle Beyer. *JITR*. Version 1.0. Oct. 2023. URL: https://github.com/beykyle/jitr.

[14] Kyle Beyer. *OSIRIS*. Version 0.1. URL: https://github.com/beykyle/osiris.

[15] Kyle Beyer et al. *BANDFramework: An Open-Source Framework for Bayesian Analysis of Nuclear Dynamics*. Tech. rep. Version 0.3.0. 2023. URL: https://github.com/bandframework/bandframework.

[16] Aage Niels Bohr and Ben R Mottelson. *Nuclear Structure (in 2 volumes)*. World Scientific Publishing Company, 1998.

[17] J. W. Boldeman and M. G. Hines. "Prompt Neutron Emission Probabilities Following Spontaneous and Thermal Neutron Fission". In: *Nuclear Science and Engineering* 91.1 (1985), pp. 114–116. DOI: 10.13182/NSE85-A17133. eprint: https://doi.org/10.13182/NSE85-A17133. URL: https://doi.org/10.13182/NSE85-A17133.

[18] JW Boldeman, AR de L Musgrove, and RL Walsh. "Prompt neutrons from 236U fission fragments". In: *Australian Journal of Physics* 24.4 (1971), pp. 821–834.

[19] G Bollen. "FRIB—Facility for rare isotope beams". In: *AIP Conference Proceedings*. Vol. 1224. 1. American Institute of Physics. 2010, pp. 432–441.

[20] Edgard Bonilla et al. "Training and projecting: A reduced basis method emulator for many-body physics". In: *Physical Review C* 106.5 (2022), p. 054322.

[21] Harry R Bowman et al. "Further Studies of the Prompt Neutrons from the Spontaneous Fission of Cf 252". In: *Physical Review* 129.5 (1963), p. 2133.

[22] David A Brown et al. "ENDF/B-VIII. 0: the 8th major release of the nuclear reaction data library with CIELO-project cross sections, new standards and thermal scattering data". In: *Nuclear Data Sheets* 148 (2018), pp. 1–142.

[23] Steven L Brunton and J Nathan Kutz. *Data-driven science and engineering: Machine learning, dynamical systems, and control*. Cambridge, England: Cambridge University Press, 2019. DOI: https://doi.org/10.1017/9781108380690.

[24] C. Budtz-Jørgensen and H.-H. Knitter. "Simultaneous investigation of fission fragments and neutrons in 252Cf (SF)". In: *Nuclear Physics A* 490.2 (1988), pp. 307–328. ISSN: 0375-9474. DOI: https://doi.org/10.1016/0375-9474(88)90508-8. URL: https://www.sciencedirect.com/science/article/pii/0375947488905088.

[25] R Capote et al. "Prompt fission neutron spectra of actinides". In: *Nuclear Data Sheets* 131 (2016), pp. 1–106.

[26] Roberto Capote et al. "RIPL–reference input parameter library for calculation of nuclear reactions and nuclear data evaluations". In: *Nuclear Data Sheets* 110.12 (2009), pp. 3107–3214. DOI: https://doi.org/10.1016/j.nds.2009.10.004.

[27] F Capuzzi and C Mahaux. "Projection operator approach to the self-energy". In: *annals of physics* 245.1 (1996), pp. 147–208.

[28] F Capuzzi and C Mahaux. "Relationship between Feshbach's and Green's Function Theories of the Nucleon–Nucleus Mean Field". In: *Annals of Physics* 281.1-2 (2000), pp. 223–359.

[29] AD Carlson et al. "International evaluation of neutron cross section standards". In: *Nuclear Data Sheets* 110.12 (2009), pp. 3215–3324.

[30] M. Catacora-Rios et al. "Exploring experimental conditions to reduce uncertainties in the optical potential". In: *Phys. Rev. C* 100 (6 Dec. 2019), p. 064615. DOI: 10.1103/PhysRevC.100.064615. URL: https://link.aps.org/doi/10.1103/PhysRevC.100.064615.

[31] Manuel Catacora-Rios et al. "Statistical tools for a better optical model". In: *Physical Review C* 104.6 (2021), p. 064611.

[32] A Chalupka et al. "Results of a Low-Background Measurement of the Fission Neutron Spectrum from 252Cf in the 9-to 29-MeV Energy Range". In: *Nuclear Science and Engineering* 106.3 (1990), pp. 367–376.

[33] Jing Chen and Yang Liu. "Locally linear embedding: a survey". In: *Artificial Intelligence Review* 36 (2011), pp. 29–48.

[34] Paulo RP Coelho, Aucyone A Da Silva, and Jose R Maiorino. "Neutron energy spectrum measurements of neutron sources with an NE-213 spectrometer". In: *Nuclear Instruments and Methods in Physics Research Section A: Accelerators, Spectrometers, Detectors and Associated Equipment* 280.2-3 (1989), pp. 270–272.

[35] Wikimedia Commons. *File:Nucleosynthesis periodic table.svg — Wikimedia Commons, the free media repository*. [Online; accessed 29-February-2024]. 2023. URL: %5Curl%7Bhttps://commons.wikimedia.org/w/index.php?title=File:Nucleosynthesis_periodic_table.svg&oldid=725687587%7D.

[36] Paul G Constantine, Eric Dow, and Qiqi Wang. "Active subspace methods in theory and practice: applications to kriging surfaces". In: *SIAM Journal on Scientific Computing* 36.4 (2014), A1500–A1524.

[37] Stephen Croft, Andrea Favalli, and Robert D. McElroy Jr. "A review of the prompt neutron nu-bar value for 252Cf spontaneous fission". In: *Nuclear Instruments and Methods in Physics Research Section A: Accelerators, Spectrometers, Detectors and Associated Equipment* 954 (2020). Symposium on Radiation Measurements and Applications XVII, p. 161605. ISSN: 0168-9002. DOI: https://doi.org/10.1016/j.nima.2018.11.064. URL: https://www.sciencedirect.com/science/article/pii/S0168900218316747.

[38] Lisandro Dalcín, Rodrigo Paz, and Mario Storti. "MPI for Python". In: *Journal of Parallel and Distributed Computing* 65.9 (2005), pp. 1108–1115. ISSN: 0743-7315. DOI: https://doi.org/10.1016/j.jpdc.2005.03.010. URL: https://www.sciencedirect.com/science/article/pii/S0743731505000560.

[39] Pierre Descouvemont. "An R-matrix package for coupled-channel problems in nuclear physics". In: *Computer physics communications* 200 (2016), pp. 199–219.

[40] Pierre Descouvemont and D Baye. "The R-matrix theory". In: *Reports on progress in physics* 73.3 (2010), p. 036301.

[41] WH Dickhoff. "Linking nuclear reactions and nuclear structure to study exotic nuclei using the dispersive optical model". In: *Compound-Nuclear Reactions*. Springer, 2021, pp. 83–90.

[42] WH Dickhoff, RJ Charity, and MH Mahzoon. "Novel applications of the dispersive optical model". In: *Journal of Physics G: Nuclear and Particle Physics* 44.3 (2017), p. 033001.

[43] WH Dickhoff et al. "Nonlocal extension of the dispersive optical model to describe data below the Fermi energy". In: *Physical Review C* 82.5 (2010), p. 054306.

[44] Willem Hendrik Dickhoff and Dimitri VY Van Neck. *aany-body theory exposed! Propagator description of quantum mechanics in many-body systems*. World Scientific Publishing Company, 2008.

[45] Shengyao Ding et al. "Research of prompt neutron from 252 Cf spontaneous fission fragment". In: *Chinese Journal of Nuclear Physics* 6.3 (1984), pp. 201–209.

[46] John R Dormand and Peter J Prince. "A family of embedded Runge-Kutta formulae". In: *Journal of computational and applied mathematics* 6.1 (1980), pp. 19–26. DOI: https://doi.org/10.1016/0771-050X(80)90013-3.

[47] C. Drischler et al. "BUQEYE Guide to Projection-Based Emulators in Nuclear Physics". In: *Front. Phys.* 10 (Dec. 2023), p. 92931. ISSN: 2296-424X. DOI: 10.3389/fphy.2022.1092931. arXiv: 2212.04912. URL: https://www.frontiersin.org/articles/10.3389/fphy.2022.1092931.

[48] C. Drischler et al. "Toward emulating nuclear reactions using eigenvector continuation". In: *Phys. Lett. B* 823 (2021), p. 136777. ISSN: 0370-2693. DOI: https://doi.org/10.1016/j.physletb.2021.136777. URL: https://www.sciencedirect.com/science/article/pii/S0370269321007176.

[49] Camille Ducoin, Jérôme Margueron, and Constança Providencia. "Nuclear symmetry energy and core-crust transition in neutron stars: A critical study". In: *Europhysics Letters* 91.3 (2010), p. 32001.

[50] M. Dupuis et al. "Challenging microscopic structure and reaction models for nucleon scattering off nuclei in the $A = 208$ mass region". In: *Phys. Rev. C* 100 (4 Oct. 2019), p. 044607. DOI: 10.1103/PhysRevC.100.044607. URL: https://link.aps.org/doi/10.1103/PhysRevC.100.044607.

[51] V.N. Dushin et al. "Facility for neutron multiplicity measurements in fission". In: *Nuclear Instruments and Methods in Physics Research Section A: Accelerators, Spectrometers, Detectors and Associated Equipment* 516.2 (2004), pp. 539–553. ISSN: 0168-9002. DOI: https://doi.org/10.1016/j.nima.2003.09.029. URL: https://www.sciencedirect.com/science/article/pii/S0168900203025117.

[52] G. Edwards, D.J.S. Findlay, and E.W. Lees. "Measurements of prompt $\bar{\nu}$ and variance for the spontaneous fission of 252Cf and 242Pu". In: *Annals of Nuclear Energy* 9.3 (1982), pp. 127–135. ISSN: 0306-4549. DOI: https://doi.org/10.1016/0306-4549(82)90012-3. URL: https://www.sciencedirect.com/science/article/pii/0306454982900123.

[53] CA Engelbrecht and HA Weidenmüller. "Single-particle states in nuclei". In: *Nuclear Physics A* 184.2 (1972), pp. 385–416.

[54] Herman Feshbach. *LNS 1992 symposium: On the matter of particles - Herman Feshbach - The optical model*. Mar. 2018. URL: https://www.youtube.com/watch?v=6I06GvMBvAE.

[55] Herman Feshbach. "The optical model and its justification". In: *Annual Review of Nuclear Science* 8.1 (1958), pp. 49–104.

[56] Herman Feshbach. "Unified theory of nuclear reactions". In: *Annals of Physics* 5.4 (1958), pp. 357–390.

[57] Herman Feshbach. "Unified theory of nuclear reactions". In: *Annals of Physics* 5.4 (1958), pp. 357–390. ISSN: 0003-4916. DOI: https://doi.org/10.1016/0003-4916(58)90007-1. URL: https://www.sciencedirect.com/science/article/pii/0003491658900071.

[58] Daniel Foreman-Mackey. "corner.py: Scatterplot matrices in Python". In: *The Journal of Open Source Software* 1.2 (June 2016), p. 24. DOI: 10.21105/joss.00024. URL: https://doi.org/10.21105/joss.00024.

[59] Message P Forum. *MPI: A Message-Passing Interface Standard*. Tech. rep. USA, 1994.

[60] CB Franklyn, C Hofmeyer, and DW Mingay. "Angular correlation of neutrons from thermal-neutron fission of 235U". In: *Physics Letters B* 78.5 (1978), pp. 564–567.

[61] R .J. Furnstahl et al. "Efficient emulators for scattering using eigenvector continuation". In: *Phys. Lett. B* 809 (2020), p. 135719. ISSN: 0370-2693. DOI: https://doi.org/10.1016/j.physletb.2020.135719. URL: https://www.sciencedirect.com/science/article/pii/S0370269320305220.

[62] Andrew Gelman et al. *Bayesian data analysis*. CRC press, 2013. DOI: https://doi.org/10.1201/b16018.

[63] Nathan P. Giha et al. "Correlations between energy and γ-ray emission in ^{239}Pu(n,f)". In: *Phys. Rev. C* 107 (1 Jan. 2023), p. 014612. DOI: 10.1103/PhysRevC.107.014612. URL: https://link.aps.org/doi/10.1103/PhysRevC.107.014612.

[64] Pablo Giuliani et al. "Toward emulating nuclear reactions using eigenvector continuation." In: *APS Division of Nuclear Physics Meeting Abstracts*. Vol. 2021. 2021, pp. LM–006.

[65] Kyle Godbey, Landon Buskirk, and Pablo Giuliani. *BMEX - The Bayesian Mass Explorer*. Sept. 2022. DOI: 10.5281/zenodo.7111988. URL: https://doi.org/10.5281/zenodo.7111988.

[66] Kyle Godbey et al. *Dimensionality Reduction in Nuclear Physics*. https://dr.ascsn.net/.

[67] Jonathan Goodman and Jonathan Weare. "Ensemble samplers with affine invariance". In: *Communications in applied mathematics and computational science* 5.1 (2010), pp. 65–80.

[68] A. Göök, F.-J. Hambsch, and M. Vidali. "Prompt neutron multiplicity in correlation with fragments from spontaneous fission of ^{252}Cf". In: *Phys. Rev. C* 90 (6 Dec. 2014), p. 064611. DOI: 10.1103/PhysRevC.90.064611. URL: https://link.aps.org/doi/10.1103/PhysRevC.90.064611.

[69] Alf Göök et al. "Prompt neutrons in correlation with fission fragments from U 235 (n, f)". In: *Physical Review C* 98.4 (2018), p. 044615.

[70] S. A. Goreinov et al. "How to Find a Good Submatrix". In: *Matrix Methods: Theory, Algorithms and Applications*. World Scientific, Apr. 2010, pp. 247–256. DOI: 10.1142/9789812836021_0015. URL: https://doi.org/10.1142%2F9789812836021_0015.

[71] Stéphane Goriely and J-P Delaroche. "The isovector imaginary neutron potential: A key ingredient for the r-process nucleosynthesis". In: *Physics Letters B* 653.2-4 (2007), pp. 178–183.

[72] Kurt Gottfried et al. *Quantum Mechanics: Fundamentals*. Springer, 2003.

[73] Martin A Grepl et al. "Efficient reduced-basis treatment of nonaffine and nonlinear partial differential equations". In: *ESAIM: Math. Model. Numer. Anal.* 41.3 (2007), pp. 575–605. DOI: https://doi.org/10.1051/m2an:2007031.

[74] R Gwin, RR Spencer, and RW Ingle. "Measurements of the energy dependence of prompt neutron emission from 233U, 235U, 239Pu, and 241Pu for En= 0.005 to 10 eV relative to emission from spontaneous fission of 252Cf". In: *Nuclear Science and Engineering* 87.4 (1984), pp. 381–404.

[75] C Hebborn et al. "Optical potentials for the rare-isotope beam era". In: *Journal of Physics G: Nuclear and Particle Physics* 50.6 (Apr. 2023), p. 060501. DOI: 10.1088/1361-6471/acc348. URL: https://dx.doi.org/10.1088/1361-6471/acc348.

[76] Chloë Hebborn and Gregory Potel. "Green's function knockout formalism". In: *Physical Review C* 107.1 (2023), p. 014607.

[77] Chloë Hebborn et al. "Quantifying uncertainties due to optical potentials in one-neutron knockout reactions". In: *arXiv preprint arXiv:2212.06056* (2022).

[78] K Hebeler et al. "Nuclear forces and their impact on neutron-rich nuclei and neutron-rich matter". In: *Annual Review of Nuclear and Particle Science* 65 (2015), pp. 457–484.

[79] Jan S Hesthaven, Gianluigi Rozza, Benjamin Stamm, et al. *Certified reduced basis methods for parametrized partial differential equations*. Vol. 590. Springer, 2016.

[80] S. Hilaire, Ch. Lagrange, and A.J. Koning. "Comparisons between various width fluctuation correction factors for compound nucleus reactions". In: *Annals of Physics* 306.2 (2003), pp. 209–231. ISSN: 0003-4916. DOI: https://doi.org/10.1016/S0003-4916(03)00076-9. URL: https://www.sciencedirect.com/science/article/pii/S0003491603000769.

[81] Peter Edward Hodgson. "The nuclear optical model". In: *Reports on Progress in Physics* 34.2 (1971), p. 765. DOI: https://dx.doi.org/10.1088/0034-4885/34/2/306.

[82] Marvin M Hoffman. "Directional correlation of fission fragments and prompt gamma rays associated with thermal neutron fission". In: *Physical Review* 133.3B (1964), B714.

[83] Norman E Holden and Martin S Zucker. "Prompt neutron emission multiplicity distribution and average values (nubar) at 2200 m/s for the fissile nuclides". In: *Nuclear Science and Engineering* 98.2 (1988), pp. 174–181.

[84] Jeremy W Holt and Taylor R Whitehead. "Modern approaches to optical potentials". In: *Handbook of Nuclear Physics*. Springer, 2022, pp. 1–30.

[85] JW Holt, N Kaiser, and W Weise. "Nuclear energy density functional from chiral two-nucleon aaand three-nucleon interactions". In: *The European Physical Journal A* 47 (2011), pp. 1–10.

[86] Martin Hořeňovský. *Catch2 3.5*. 2024. URL: https://github.com/catchorg/Catch2.

[87] N.M. Hugenholtz and L. van Hove. "A theorem on the single particle energy in a Fermi gas with interaction". In: *Physica* 24.1 (1958), pp. 363–376. ISSN: 0031-8914. DOI: https://doi.org/10.1016/S0031-8914(58)95281-9. URL: https://www.sciencedirect.com/science/article/pii/S0031891458952819.

[88] Alan Julian Izenman. "Introduction to manifold learning". In: *Wiley Interdisciplinary Reviews: Computational Statistics* 4.5 (2012), pp. 439–446.

[89] Patrick Jaffke et al. "Hauser-Feshbach fission fragment de-excitation with calculated macroscopic-microscopic mass yields". In: *Physical Review C* 97.3 (2018), p. 034608.

[90] J.P Jeukenne, A Lejeune, and C Mahaux. "Many-body theory of nuclear matter". In: *Physics Reports* 25.2 (1976), pp. 83–174. ISSN: 0370-1573. DOI: https://doi.org/10.1016/0370-1573(76)90017-X. URL: https://www.sciencedirect.com/science/article/pii/037015737690017X.

[91] T. Kawano et al. "Influence of nonstatistical properties in nuclear structure on emission of prompt fission neutrons". In: *Phys. Rev. C* 104 (1 July 2021), p. 014611. DOI: 10.1103/PhysRevC.104.014611. URL: https://link.aps.org/doi/10.1103/PhysRevC.104.014611.

[92] Toshihiko Kawano, Satoshi Chiba, and Hiroyuki Koura. "Phenomenological Nuclear Level Densities using the KTUY05 Nuclear Mass Formula for Applications Off-Stability". In: *Journal of Nuclear Science and Technology* 43.1 (2006), pp. 1–8. DOI: 10.1080/18811248.2006.9711062. eprint: https://www.tandfonline.com/doi/pdf/10.1080/18811248.2006.9711062. URL: https://www.tandfonline.com/doi/abs/10.1080/18811248.2006.9711062.

[93] Yasuyuki Kikuchi et al. "Neutron nuclear data of 235 U, 238 U, 239 Pu, 240 Pu and 241 Pu adopted in JENDL-1". In: (1977).

[94] G. B. King et al. "Direct Comparison between Bayesian and Frequentist Uncertainty Quantification for Nuclear Reactions". In: *Phys. Rev. Lett.* 122 (23 June 2019), p. 232502. DOI: 10.1103/PhysRevLett.122.232502. URL: https://link.aps.org/doi/10.1103/PhysRevLett.122.232502.

[95] AJ Koning and JP Delaroche. "Local and global nucleon optical models from 1 keV to 200 MeV". In: *Nuclear Physics A* 713.3-4 (2003), pp. 231–310.

[96] NV Kornilov. "Verification of the 252 Cf standard in the energy range 2–20 MeV". In: *INDC (USA)-108, International Atomic Energy Agency, International Nuclear Data Committee* (2015).

[97] Holger Krekel et al. *pytest 8.2*. 2004. URL: https://github.com/pytest-dev/pytest.

[98] Wilhelm Kutta. *Beitrag zur näherungsweisen Integration totaler Differentialgleichungen*. Teubner, 1901.

[99] A Lajtai et al. "Energy spectrum measurements of neutrons for energies 30 keV-4 meV from thermal fission of main fuel elements". In: *Radiation Effects* 93.1-4 (1986), pp. 277–280.

[100] A Lajtai et al. "Low-energy neutron spectrometer and its application for 252Cf neutron spectrum measurements". In: *Nuclear Instruments and Methods in Physics Research Section A: Accelerators, Spectrometers, Detectors and Associated Equipment* 293.3 (1990), pp. 555–561.

[101] A.M. Lane. "Isobaric spin dependence of the optical potential and quasi-elastic (p, n) reactions". In: *Nuclear Physics* 35 (1962), pp. 676–685. ISSN: 0029-5582. DOI: https://doi.org/10.1016/0029-5582(62)90153-0. URL: https://www.sciencedirect.com/science/article/pii/0029558262901530.

[102] AM Lane. "New term in the nuclear optical potential: implications for (p, n) mirror state reactions". In: *Physical Review Letters* 8.4 (1962), p. 171.

[103] AM Lane and RG Thomas. "R-matrix theory of nuclear reactions". In: *Reviews of Modern Physics* 30.2 (1958), p. 257. DOI: https://doi.org/10.1103/RevModPhys.30.257.

[104] A.C. Larsen et al. "Novel techniques for constraining neutron-capture rates relevant for r-process heavy-element nucleosynthesis". In: *Progress in Particle and Nuclear Physics* 107 (2019), pp. 69–108. ISSN: 0146-6410. DOI: https://doi.org/10.1016/j.ppnp.2019.04.002. URL: https://www.sciencedirect.com/science/article/pii/S0146641019300298.

[105] Bao-An Li and Xiao Han. "Constraining the neutron–proton effective mass splitting using empirical constraints on the density dependence of nuclear symmetry energy around normal density". In: *Physics Letters B* 727.1 (2013), pp. 276–281. ISSN: 0370-2693. DOI: https://doi.org/10.1016/j.physletb.2013.10.006. URL: https://www.sciencedirect.com/science/article/pii/S0370269313007995.

[106] Yeunhwan Lim and Jeremy W. Holt. "Structure of neutron star crusts from new Skyrme effective interactions constrained by chiral effective field theory". In: *Phys. Rev. C* 95 (6 June 2017), p. 065805. DOI: 10.1103/PhysRevC.95.065805. URL: https://link.aps.org/doi/10.1103/PhysRevC.95.065805.

[107] A E Lovell, A T Mohan, and P Talou. "Quantifying uncertainties on fission fragment mass yields with mixture density networks". In: *Journal of Physics G: Nuclear and Particle Physics* 47.11 (Sept. 2020), p. 114001. DOI: 10.1088/1361-6471/ab9f58. URL: https://dx.doi.org/10.1088/1361-6471/ab9f58.

[108] A. E. Lovell and F. M. Nunes. "Constraining transfer cross sections using Bayes' theorem". In: *Phys. Rev. C* 97 (6 June 2018), p. 064612. DOI: 10.1103/PhysRevC.97.064612. URL: https://link.aps.org/doi/10.1103/PhysRevC.97.064612.

[109] A. E. Lovell et al. "Uncertainty quantification for optical model parameters". In: *Phys. Rev. C* 95 (2 Feb. 2017), p. 024611. DOI: 10.1103/PhysRevC.95.024611. URL: https://link.aps.org/doi/10.1103/PhysRevC.95.024611.

[110] AE Lovell et al. "Recent advances in the quantification of uncertainties in reaction theory". In: *Journal of Physics G: Nuclear and Particle Physics* 48.1 (2020), p. 014001.

[111] Amy Lovell and Arvind Mohan. "Novel emulators for fission event generators". In: *Bulletin of the American Physical Society* (2023).

[112] Amy E Lovell and Denise Neudecker. *Correcting the PFNS for more consistent fission modeling*. Tech. rep. Los Alamos National Lab.(LANL), Los Alamos, NM (United States), 2021.

[113] Amy E Lovell and Denise Neudecker. *Energy-dependent optimization of the prompt fission neutron spectrum with CGMF*. Tech. rep. Los Alamos National Lab.(LANL), Los Alamos, NM (United States), 2022.

[114] Ruprecht Machleidt and David Rodrignez Entem. "Chiral effective field theory and nuclear forces". In: *Physics Reports* 503.1 (2011), pp. 1–75.

[115] C Mahaux and R Sartor. "Single-particle motion in nuclei". In: *Advances in Nuclear Physics*. Springer, 1991, pp. 1–223.

[116] Stefano Marin et al. "Event-by-event neutron–photon multiplicity correlations in 252Cf (sf)". In: *Nuclear Instruments and Methods in Physics Research Section A: Accelerators, Spectrometers, Detectors and Associated Equipment* 968 (2020), p. 163907.

[117] Stefano Marin et al. "Structure in the event-by-event energy-dependent neutron-γ multiplicity correlations in Cf 252 (sf)". In: *Physical Review C* 104.2 (2021), p. 024602.

[118] H Märten et al. "The 252Cf (sf) neutron spectrum in the 5-to 20-MeV energy range". In: *Nuclear science and engineering* 106.3 (1990), pp. 353–366.

[119] W.J. McDonald and J.M. Robson. "The scattering of 14.1 MeV neutrons by Ca40". In: *Nuclear Physics* 59.2 (1964), pp. 321–331. ISSN: 0029-5582. DOI: https://doi.org/10.1016/0029-5582(64)90087-2. URL: https://www.sciencedirect.com/science/article/pii/0029558264900872.

[120] K Meierbachtol et al. "The SPIDER fission fragment spectrometer for fission product yield measurements". In: *Nuclear Instruments and Methods in Physics Research Section A: Accelerators, Spectrometers, Detectors and Associated Equipment* 788 (2015), pp. 59–66.

[121] JA Melendez et al. "Model reduction methods for nuclear emulators". In: *Journal of Physics G: Nuclear and Particle Physics* 49.10 (2022), p. 102001.

[122] Alan J Miller and Nam-Ky Nguyen. "Algorithm AS 295: A Fedorov exchange algorithm for D-optimal design". In: *Journal of the Royal Statistical Society. Series C (Applied Statistics)* 43.4 (1994), pp. 669–677. DOI: http://dx.doi.org/10.2307/2986264.

[123] Toby J Mitchell. "An algorithm for the construction of "D-optimal" experimental designs". In: *Technometrics* 42.1 (2000), pp. 48–54. DOI: https://doi.org/10.2307/1271431.

[124] PA Moldauer. "Optical-Model Fringe Absorption and the Neutron Strength Function". In: *Physical Review Letters* 9.1 (1962), p. 17.

[125] AM Moro and FM Nunes. "Transfer to the continuum and breakup reactions". In: *Nuclear Physics A* 767 (2006), pp. 138–154.

[126] Petr Navrátil et al. "Unified ab initio approaches to nuclear structure and reactions". In: *Physica Scripta* 91.5 (2016), p. 053002.

[127] VN Nefedov. "High precision spectra measurements for neutrons arising from the fission of Cf-252, U-233, U-235, Pu-239 in the energy range 0.045 MeV". In: *All-Union Conf. Neutron Physics, Kiev, Oct. 2-6, 1983*. Vol. 2. 1983, p. 285.

[128] W. G. Newton and Bao-An Li. "Constraining the gravitational binding energy of PSR J0737-3039B using terrestrial nuclear data". In: *Phys. Rev. C* 80 (6 Dec. 2009), p. 065809. DOI: 10.1103/PhysRevC.80.065809. URL: https://link.aps.org/doi/10.1103/PhysRevC.80.065809.

[129] Nam-Ky Nguyen and Alan J Miller. "A review of some exchange algorithms for constructing discrete D-optimal designs". In: *Computational Statistics & Data Analysis* 14.4 (1992), pp. 489–498. DOI: https://doi.org/10.1016/0167-9473(92)90064-M.

[130] K. Nishio et al. "Multiplicity and energy of neutrons from 235U(nth,f) fission fragments". In: *Nuclear Physics A* 632.4 (1998), pp. 540–558. ISSN: 0375-9474. DOI: https://doi.org/10.1016/S0375-9474(98)00008-6. URL: https://www.sciencedirect.com/science/article/pii/S0375947498000086.

[131] B. V. Noumerov. "A Method of Extrapolation of Perturbations". In: *Monthly Notices of the Royal Astronomical Society* 84.8 (June 1924), pp. 592–602. ISSN: 0035-8711. DOI: 10.1093/mnras/84.8.592. eprint: https://academic.oup.com/mnras/article-pdf/84/8/592/3661174/mnras84-0592.pdf. URL: https://doi.org/10.1093/mnras/84.8.592.

[132] Andreas Oberstedt et al. "Improved values for the characteristics of prompt-fission γ-ray spectra from the reaction 235 U (n th, f)". In: *Physical Review C* 87.5 (2013), p. 051602.

[133] Daniel Odell et al. *Reduced Order Scattering Emulator (ROSE) Documentation*. 2023. URL: https://reduced-order-scattering-emulator.readthedocs.io.

[134] Daniel Odell et al. "ROSE: A reduced-order scattering emulator for optical models". In: *arXiv preprint arXiv:2312.12426* (2023).

[135] Kazuhiro Oyamatsu, Kei Iida, and Hiroyuki Koura. "Neutron drip line and the equation of state of nuclear matter". In: *Phys. Rev. C* 82 (2 Aug. 2010), p. 027301. DOI: 10.1103/PhysRevC.82.027301. URL: https://link.aps.org/doi/10.1103/PhysRevC.82.027301.

[136] Arno A Penzias. "The origin of the elements". In: *Reviews of Modern Physics* 51.3 (1979), p. 425.

[137] F. Perey and B. Buck. "A non-local potential model for the scattering of neutrons by nuclei". In: *Nuclear Physics* 32 (1962), pp. 353–380. ISSN: 0029-5582. DOI: https://doi.org/10.1016/0029-5582(62)90345-0. URL: https://www.sciencedirect.com/science/article/pii/0029558262903450.

[138] Matthew Plumlee et al. *surmise 0.2.1 Users Manual*. Tech. rep. Version 0.2.1. NAISE, 2023. URL: https://surmise.readthedocs.io.

[139] CD Pruitt, JE Escher, and R Rahman. "Uncertainty-quantified phenomenological optical potentials for single-nucleon scattering". In: *Physical Review C* 107.1 (2023), p. 014602.

[140] Cole Pruitt et al. "Toward the Next Generation of Optical-Model Potentials". In: *APS Division of Nuclear Physics Meeting Abstracts*. Vol. 2020. 2020, FD–010.

[141] Cole Davis Pruitt et al. "Isotopically resolved neutron total cross sections at intermediate energies". In: *Physical Review C* 102.3 (2020), p. 034601.

[142] Alfio Quarteroni, Andrea Manzoni, and Federico Negri. *Reduced Basis Methods for Partial Differential Equations: An Introduction*. Vol. 92. New York: Springer, 2015. DOI: https://doi.org/10.1007/978-3-319-15431-2.

[143] APD Ramirez et al. "Nuclear level densities of 64, 66 Zn from neutron evaporation". In: *Physical Review C* 88.6 (2013), p. 064324.

[144] George Rawitscher, Victo dos Santos Filho, and Thiago Carvalho Peixoto. "Galerkin and Collocation Methods". In: *An Introductory Guide to Computational Methods for the Solution of Physics Problems*. New York: Springer, 2018, pp. 17–31. DOI: https://doi.org/10.1007/978-3-319-42703-4.

[145] "Reaching for the Horizon: The 2015 Long Range Plan for Nuclear Science". In: (Sept. 2015). URL: https://www.osti.gov/biblio/1296778.

[146] Michael Evan Rising et al. *Correlated Fission Physics, Transport and Applications.* Tech. rep. Lawrence Livermore National Lab.(LLNL), Livermore, CA (United States), 2019.

[147] Nathaniel Roth et al. "General Relativistic Implicit Monte Carlo Radiation-hydrodynamics". In: *The Astrophysical Journal* 933.2 (2022), p. 226.

[148] Carl Runge. "Über die numerische Auflösung von Differentialgleichungen". In: *Mathematische Annalen* 46.2 (1895), pp. 167–178. DOI: http://dx.doi.org/10.1007/bf01446807.

[149] P. Santi and M. Miller. "Reevaluation of Prompt Neutron Emission Multiplicity Distributions for Spontaneous Fission". In: *Nuclear Science and Engineering* 160.2 (2008), pp. 190–199. DOI: 10.13182/NSE07-85. eprint: https://www.tandfonline.com/doi/pdf/10.13182/NSE07-85. URL: https://www.tandfonline.com/doi/abs/10.13182/NSE07-85.

[150] HW Schmitt, WE Kiker, and CW Williams. "Precision measurements of correlated energies and velocities of Cf 252 fission fragments". In: *Physical Review* 137.4B (1965), B837.

[151] Nicolas Schunck and David Regnier. "Theory of nuclear fission". In: *Progress in Particle and Nuclear Physics* 125 (2022), p. 103963.

[152] Tomasz Sowiński and Miguel A Garcia-March. "Fundamental limitations of the eigenvalue continuation approach". In: *Physical Review C* 106.2 (2022), p. 024002.

[153] R. R. Spencer, R. Gwin, and R. Ingle. "A Measurement of the Average Number of Prompt Neutrons from Spontaneous Fission of Californium-252". In: *Nuclear Science and Engineering* 80.4 (1982), pp. 603–629. DOI: 10.13182/NSE82-A18973. eprint: https://doi.org/10.13182/NSE82-A18973. URL: https://doi.org/10.13182/NSE82-A18973.

[154] BI Starostov, VN Nefedov, and AA Boytzov. "High Precision Prompt Neutron Spectra Measurement for Neutrons from Cf-252, U-233, U-235, Pu-239 fission in the energy range 2.–11 MeV". In: *Nejtronnaja Fizika (6-th Conf. for Neutron Phys., Kiev. 1983), v2. p285*. Vol. 290. 1983, p. 294.

[155] Ionel Stetcu et al. "Angular momentum removal by neutron and γ-ray emissions during fission fragment decays". In: *Physical Review Letters* 127.22 (2021), p. 222502.

[156] Ke Sun and Stéphane Marchand-Maillet. "An information geometry of statistical manifold learning". In: *International Conference on Machine Learning*. PMLR. 2014, pp. 1–9.

[157] Özge Sürer et al. "Uncertainty quantification in breakup reactions". In: *Physical Review C* 106.2 (2022), p. 024607.

[158] Kenji Suzuki and Shyh Yuan Lee. "Convergent Theory for Effective Interaction in Nuclei*)". In: *Progress of Theoretical Physics* 64.6 (Dec. 1980), pp. 2091–2106. ISSN: 0033-068X. DOI: 10.1143/PTP.64.2091. eprint: https://academic.oup.com/ptp/article-pdf/64/6/2091/5274301/64-6-2091.pdf. URL: https://doi.org/10.1143/PTP.64.2091.

[159] Patrick Talou and Ramona Vogt. *Nuclear Fission: Theories, Experiments and Applications*. Springer Nature, 2023.

[160] Patrick Talou et al. "Fission fragment decay simulations with the CGMF code". In: *Computer Physics Communications* 269 (2021), p. 108087.

[161] TARO TAMURA. "Analyses of the Scattering of Nuclear Particles by Collective Nuclei in Terms of the Coupled-Channel Calculation". In: *Rev. Mod. Phys.* 37 (4 Oct. 1965), pp. 679–708. DOI: 10.1103/RevModPhys.37.679. URL: https://link.aps.org/doi/10.1103/RevModPhys.37.679.

[162] John R Taylor. *Scattering theory: the quantum theory of nonrelativistic collisions*. Courier Corporation, 2006.

[163] Ian J Thompson and Filomena M Nunes. *Nuclear reactions for astrophysics: principles, calculation and applications of low-energy reactions*. Cambridge University Press, 2009.

[164] Ian J. Thompson. "Coupled reaction channels calculations in nuclear physics". In: *Computer Physics Reports* 7.4 (1988), pp. 167–212. ISSN: 0167-7977. DOI: https://doi.org/10.1016/0167-7977(88)90005-6. URL: https://www.sciencedirect.com/science/article/pii/0167797788900056.

[165] A Trkov, R Capote, and VG Pronyaev. "Current issues in nuclear data evaluation methodology: 235U prompt fission neutron spectra and multiplicity for thermal neutrons". In: *Nuclear Data Sheets* 123 (2015), pp. 8–15.

[166] S. Typel and B. Alex Brown. "Neutron radii and the neutron equation of state in relativistic models". In: *Phys. Rev. C* 64 (2 June 2001), p. 027302. DOI: 10.1103/PhysRevC.64.027302. URL: https://link.aps.org/doi/10.1103/PhysRevC.64.027302.

[167] Jacobus JM Verbaarschot, Hans A Weidenmüller, and Martin R Zirnbauer. "Grassmann integration in stochastic quantum physics: The case of compound-nucleus scattering". In: *Physics Reports* 129.6 (1985), pp. 367–438.

[168] Pauli Virtanen et al. "SciPy 1.0: Fundamental Algorithms for Scientific Computing in Python". In: *Nature Methods* 17 (2020), pp. 261–272. DOI: 10.1038/s41592-019-0686-2.

[169] AV Voinov et al. "Test of nuclear level density inputs for Hauser-Feshbach model calculations". In: *Physical Review C* 76.4 (2007), p. 044602.

[170] AS Vorobyev. "Distribution of prompt neutron emission probability for fission fragments in spontaneous fission of^< 252> Cf and^< 244, 248> Cm". In: *International Seminar on Interactions of Neutrons with Nuclei,(ISINN-9), 2001*. Vol. 9. 2001, pp. 276–295.

[171] AS Vorobyev et al. "Angular and energy distributions of prompt neutrons from thermal neutron-induced fission of U-233, U-235 (N, F)". In: *Proc. of the XVII International Seminar on Interaction of Neutrons with Nuclei: Neutron Spectroscopy, Nuclear Structure, Related Topics (AM Sukhovoj, ed.),(Dubna)*. 2010, p. 60.

[172] Arthur C Wahl. *Systematics of fission-product yields*. Tech. rep. Los Alamos National Lab., 2002.

[173] A Wallner, B Strohmaier, and H Vonach. "Extraction of nuclear level densities from neutron spectra emitted in proton-induced reactions on lead isotopes and Bi". In: *Physical Review C* 51.2 (1995), p. 614.

[174] Jianzhong Wang and Jianzhong Wang. "Local tangent space alignment". In: *Geometric Structure of High-Dimensional Data and Dimensionality Reduction* (2012), pp. 221–234.

[175] William J Welch. "Algorithmic complexity: three NP-hard problems in computational statistics". In: *Journal of Statistical Computation and Simulation* 15.1 (1982), pp. 17–25. DOI: https://doi.org/10.1080/00949658208810560.

[176] H Werle and H Bluhm. "Fission-neutron spectra measurements of 235U, 239Pu and 252Cf". In: *Journal of Nuclear Energy* 26.4 (1972), pp. 165–176.

[177] Taylor Whitehead. "Microscopic Nucleon-Nucleus Optical Potentials from Chiral Effective Field Theory". PhD thesis. 2021.

[178] TR Whitehead, Y Lim, and JW Holt. "Global Microscopic Description of Nucleon-Nucleus Scattering with Quantified Uncertainties". In: *Physical Review Letters* 127.18 (2021), p. 182502.

[179] TR Whitehead et al. "Prediction for (p, n) charge-exchange reactions with uncertainty quantification". In: *Physical Review C* 105.5 (2022), p. 054611.

[180] JN Wilson et al. "Angular momentum generation in nuclear fission". In: *Nature* 590.7847 (2021), pp. 566–570. URL: https://doi.org/10.1038/s41586-021-03304-w.

[181] C. Winstead and P. W. Langhoff. "Feshbach–Fano formalism in Hilbert space: Application to shape resonances in molecular photoionization". In: *The Journal of Chemical Physics* 95.5 (Sept. 1991), pp. 3107–3118. ISSN: 0021-9606. DOI: 10.1063/1.460868. eprint: https://pubs.aip.org/aip/jcp/article-pdf/95/5/3107/13409260/3107_1_online.pdf. URL: https://doi.org/10.1063/1.460868.

[182] R. B. Wiringa, V. G. J. Stoks, and R. Schiavilla. "Accurate nucleon-nucleon potential with charge-independence breaking". In: *Phys. Rev. C* 51 (1 Jan. 1995), pp. 38–51. DOI: 10.1103/PhysRevC.51.38. URL: https://link.aps.org/doi/10.1103/PhysRevC.51.38.

[183] Chang Xu, Bao-An Li, and Lie-Wen Chen. "Symmetry energy, its density slope, and neutron-proton effective mass splitting at normal density extracted from global nucleon optical potentials". In: *Phys. Rev. C* 82 (5 Nov. 2010), p. 054607. DOI: 10.1103/PhysRevC.82.054607. URL: https://link.aps.org/doi/10.1103/PhysRevC.82.054607.

[184] Wang Yufeng et al. "AN EXPERIMENTAL STUDY OF THE PROMPT NEUTRON SPECTRUM OF U-235 FISSION INDUCED BY THERMAL NEUTRONS". In: *Physics and Chemistry of Fission: Proceedings of the XVIIIth International Symposium on Nuclear Physics, Gaussig (GDR), 21-25 November 1988*. Nova Publishers. 1992, p. 183.

[185] Sh Zeynalov et al. "Neutron emission in fission of 252 Cf (sf)". In: *AIP Conference Proceedings*. Vol. 1175. 1. American Institute of Physics. 2009, pp. 359–362.

[186] Zhenyue Zhang and Hongyuan Zha. "Principal Manifolds and Nonlinear Dimensionality Reduction via Tangent Space Alignment". In: *SIAM Journal on Scientific Computing* 26.1 (2004), pp. 313–338. DOI: 10.1137/S1064827502419154. eprint: https://doi.org/10.1137/S1064827502419154. URL: https://doi.org/10.1137/S1064827502419154.

Appendix

A.1 Details of single-particle scattering

Typical optical potentials that take only the elastic channel as the $\mathbb{P}$-space further assume that the relevant target ground state is spherical, with angular momentum and parity 0^+. As this describes the optical potentials used in this work, we will describe the relevant results for the scattering of a spin-1/2 nucleon on such a system here. We will primarily adapt our description from the texts [162, 44]. A more general description of scattering which includes arbitrary target angular momenta, deformed ground state which couple to bands of excited states, etc., is given in various places in the literature, including, for example [161, 164, 163].

We begin with the Dyson equation in operator form as given in Eq. 2.34, as well as the version involving the $\mathcal{T}$-matrix, Eq. 2.35. Our goal will be to perform a partial wave expansion, obtaining useful and well-known formulae for the scattering observables — cross sections, analyzing powers, etc. — in terms of the partial-wave matrix elements of the scattering amplitude Eq. 2.48 (or, equivalently, in terms of $\mathcal{S}$ or $\mathcal{T}$).

To do so, we use the definition of the spherical harmonics to expand the plane wave spin state $|\mathbf{k}sm_s\rangle = |\mathbf{k}\,\tfrac{1}{2}\,m_s\rangle$:

$$\begin{aligned} |\mathbf{k}\,\tfrac{1}{2}\,m_s\rangle &= \sum_{lm_l} \langle klm_lm_s|\mathbf{k}\,\tfrac{1}{2}\,m_s\rangle\,|klm_lm_s\rangle \\ &= \sum_{lm_l} Y_l^{m_l\,*}(\theta,\phi)\,|klm_lm_s\rangle\,, \end{aligned} \tag{1}$$

where (θ,ϕ) are the azimuthal and polar angle in the direction of the plane wave state $\mathbf{k}$.

Because of the presence of spin-orbit coupling in the optical potential, Eq. 2.69, the interaction V_{om}, and, therefore the scattering matrices, will not be diagonal in the uncoupled angular momentum basis $|klm_lm_s\rangle$. We will instead transform to a basis to total angular momentum (which is used throughout Chapter 2), with states of the operator

$$\mathbf{J} \equiv \mathbf{L} + \mathbf{S}, \tag{2}$$

which does commute with V_{om}:

$$|kl\,\tfrac{1}{2}\,jm\rangle = \sum_{m_l m_s} \langle lm_l\,\tfrac{1}{2}\,m_s|jm\rangle\,|klm_l\,\tfrac{1}{2}\,m_s\rangle\,. \tag{3}$$

The unitary matrix defining this transformation has as elements the Clebsch-Gordan coefficients $\langle lm_l\,\frac{1}{2}\,m_s|jm\rangle$.

In this basis, we have a free propagator diagonal in $|kjlsm_j\rangle$:

$$G^{(0)}_{jl\,\frac{1}{2}\,m}(k,k';E) = \frac{\delta(k-k')}{k^2}\,\frac{1}{E-E_k+i\eta}, \tag{4}$$

with $E_k = \hbar^2k^2/2\mu$, as usual. In the presence of the Coulomb-term, our definition of the free Hamiltonian $\mathcal{H}^{(0)} \equiv \mathcal{H}_{om} - V_{om}$ differs by the long-range Coulomb interaction, and determines a different free propagator. This is treated in standard texts on scattering theory, e.g. [162, 72]. We will proceed with the derivation for neutral particles, and state the modifications required for protons at the end. Furthermore, we will assume the interaction is rotationally invariant, such that every operator will be diagonal in m. Accordingly, we now drop the $\frac{1}{2}\,m$ for notational compactness. The resulting Dyson equation is diagonal in the total angular momentum:

$$\begin{aligned} G_{jl}(k,k';E) &= G^{(0)}_{jl}(k,k';E) + \frac{1}{E-E_k+i\eta}\int_0^\infty dqq^2\ \langle k|V^{jl}_{om}(E)|q\rangle\,G_{jl}(k,k';E) \\ &= G^{(0)}_{jl}(k,k';E) + \frac{\langle k|\mathcal{T}^{jl}(E)|k'\rangle}{(E-E_k+i\eta)(E-E_{k'}+i\eta)}. \end{aligned} \tag{5}$$

We can write this in the radial coordinate space using a double Fourier-Bessel transform:

$$G_{jl}(r,r';E) = \frac{2}{\pi}\int_0^\infty\int_0^\infty dkdk'\,k^2k'^2\,j_l(kr)G_{jl}(k,k',E)j_l(k'r'), \tag{6}$$

where $j_l(s)$ are the spherical Bessel functions of the first kind. The result is

$$
\begin{aligned}
G_{jl}(r,r';E) &= G^{(0)}_{jl}(r,r';E) + \int_0^\infty \int_0^\infty dr_1 dr_2\, r_1^2 r_2^2 G^{(0)}_{jl}(r,r_1;E)\, \langle r_1|V^{jl}_{om}(E)|r_2\rangle\, G_{jl}(r_2,r';E) \\
&= G^{(0)}_{jl}(r,r';E) + \int_0^\infty dr_1\, r_1^2 G^{(0)}_{jl}(r,r_1;E)\, \langle r_1|V^{jl}_{om}(E)|r_1\rangle\, G_{jl}(r_1,r';E).
\end{aligned}
\tag{7}
$$

The last equality is true only if the optical potential is local in coordinate-space; e.g.

$$
\langle r_1|V^{jl}_{om}(E)|r_2\rangle = \delta(r_1 - r_2) V^{jl}_{om}(r_1;E) \tag{8}
$$

but this is not a necessary assumption for the following. A set of contour integrations, each taking place in the upper or lower complex-k half-plane, yields a form for the free propagator in coordinate-space:

$$
G^{(0)}_{jl}(r,r';E) = -ik\frac{2\mu}{\hbar^2} j_l(kr_<) h^+_l(kr_>), \tag{9}
$$

where h^+_l is the outgoing spherical Hankel function, and $r_{>(<)}$ refers to the greater(lesser) of $\{r,r'\}$. In terms of the $\mathcal{T}$-matrix, the propagator is

$$
G_{jl}(r,r';E) = G^{(0)}_{jl}(r,r',E) + \int_0^\infty \int_0^\infty dr_1 dr_2\, r_1^2 r_2^2\, G^{(0)}_{jl}(r,r_1;E)\, \langle r_1|\mathcal{T}^{jl}(E)|r_2\rangle\, G^{(0)}_{jl}(r_2,r';E). \tag{10}
$$

We would like to determine the behavior of the propagator far away from the short-range influence of V_{om}; e.g. as $r' \to \infty$, and to decompose this behavior into the propagation of an incoming and outgoing wave. The result is

$$
\begin{aligned}
G_{jl}(r,r';E) &\to -i\frac{\mu}{\hbar^2} h^+_l(kr') \left(h^-_l(kr) + \left[1 - 2\pi i \frac{\mu k}{\hbar^2} \left\langle k \middle| \mathcal{T}^{jl}(E_k) \middle| k \right\rangle \right] h^+_l(kr) \right) \\
&= -i\frac{\mu}{\hbar^2} h^+_l(kr') \left(h^-_l(kr) + \mathcal{S}^{jl}(E_k) h^+_l(kr) \right).
\end{aligned}
\tag{11}
$$

This is a statement that the ratio of the incoming and outgoing asymptotic wavefunctions

is exactly the on-shell $\mathcal{S}$-matrix, which has the expected relation to the $\mathcal{T}$-matrix. This has equivalent meaning to what we derived in the time-dependent formalism in Section 2.2, except for that now, we have broken the scattering matrices into individual partial waves, which provides a useful calulational framework for observables. To account for charged projectiles, we simply replace the Bessel and Hankel functions, $j_l(kr)$, and $h^{\pm}(kr)$, with the Coulomb-wave and Coulomb-Hankel functions $F_l(\eta, kr)$, $H_l^{\pm}(\eta, kr)$.

We define the scattering phase shift $\delta_{jl(E)}$ for a partial wave:

$$\mathcal{S}^{jl}(E) = e^{2i\delta_{jl}(E)}, \tag{12}$$

which is complex when $\mathcal{S}$ is not unitary. We now recall our definition of the scattering amplitude, which, in this case, forms a 2×2 matrix in spin-space:

$$f_{m_s', m_s}(\theta, \phi) = \frac{4\mu\pi^2}{\hbar^2} \langle \mathbf{k}' m_s' \,|\, \mathcal{T}(E_k) \,|\, \mathbf{k} m_s \rangle \,. \tag{13}$$

To break this into partial waves so that it can be related to the partial-wave matrix elements, we write the scattering amplitude in the customary form:

$$f_{m_s', m_s}(\theta, \phi) = \delta_{m_s', m_s} \mathcal{F}(\theta) + [\boldsymbol{\sigma} \cdot \hat{\mathbf{n}}]_{m_s', m_s} \mathcal{G}(\theta), \tag{14}$$

where σ_i are the Pauli-matrices, and $\hat{\mathbf{n}}$ points in the direction of $\mathbf{k}' \times \mathbf{k}'$. This leads to the following definitions of $\mathcal{F}$ and $\mathcal{G}$ in terms of the $\mathcal{S}$-matrix elements [162]:

$$\mathcal{F}(\theta) = \frac{1}{2ik} \sum_l^{\infty} \left[(l+1)(S^{l+\frac{1}{2}, l} - 1) + l(S^{l-\frac{1}{2}, l} - 1) \right] P_l(\cos\theta), \tag{15}$$

and

$$\mathcal{G}(\theta) = \frac{1}{2ik} \sum_l^{\infty} \left(S^{l+\frac{1}{2}, l} - S^{l-\frac{1}{2}, l} \right) P_l^1(\cos\theta), \tag{16}$$

where $P_l(z)$, $P_l^m(z)$ are, respectively, the Legendre polynomials, and the associated Legen-

dre polynomials.

We cannot have a negative total angular momentum; $\mathcal{S}^{j0}$ is only non-zero for $j = 1/2$. In the case that we have a charged projectile, we must modify the spin-preserving amplitude $\mathcal{F}$:

$$\begin{aligned}\mathcal{F}(\theta) \leftarrow \frac{1}{2ik}\sum_{l}^{\infty} e^{2i\sigma_l}\left[(l+1)(S^{l+\frac{1}{2},l}-1)+l(S^{l-\frac{1}{2},l}-1)\right]P_l(\cos\theta) \\ -\frac{\eta}{2k\sin^2\theta/2}\exp 2i(\sigma_0-\eta\ln\sin\theta/2),\end{aligned} \tag{17}$$

where $\eta = Z_1 Z_2 e^2\mu/\hbar^2 k$ is the Sommerfield parameter, σ_l is the Coulomb phase shift:

$$\sigma_l = \arg\Gamma\left(l+1+i\eta\right), \tag{18}$$

and Γ is the gamma function.

We then have unpolarized differential elastic scattering cross section:

$$\frac{d\sigma}{d\Omega} = |\mathcal{F}(\theta)|^2 + |\mathcal{G}(\theta)|^2. \tag{19}$$

The analyzing powers are:

$$A_y = \frac{2\mathfrak{Re}\left[\mathcal{F}^*(\theta)\mathcal{G}(\theta)\right]}{|\mathcal{F}(\theta)|^2+|\mathcal{G}(\theta)|^2}. \tag{20}$$

The angle-integrated elastic cross section results from the optical theorem and the orthogonality of the Legendre polynomials, it is:

$$\begin{aligned}\sigma_{el} =& \frac{\pi}{k^2}\frac{1}{2l+1}\sum_{l=0}^{\infty}\left|(l+1)(S^{l+\frac{1}{2},l}-1)+l(S^{l-\frac{1}{2},l}-1)\right|^2 \\ &+\frac{\pi}{k^2}\frac{1}{2l+1}\sum_{l=0}^{\infty}\left|l(l+1)(S^{l+\frac{1}{2},l}-S^{l-\frac{1}{2},l})\right|^2\end{aligned}. \tag{21}$$

The total cross section is

$$\sigma_t = \frac{2\pi}{k^2}\sum_l^\infty (l+1)(1-\mathfrak{Re}\mathcal{S}^{l+\frac{1}{2},l}) + l(1-\mathfrak{Re}\mathcal{S}^{l-\frac{1}{2},l}), \tag{22}$$

so that, by unitary, we have the reaction cross section for transitions to the $\mathbb{Q}$-space:

$$\begin{aligned}\sigma_{rxn} &= \frac{\pi}{k^2}\sum_l^\infty (l+1)(1-\left|\mathcal{S}^{l+\frac{1}{2},l}\right|^2) + l(1-\left|\mathcal{S}^{l-\frac{1}{2},l}\right|^2) \\ &= \frac{\pi}{k^2}\sum_l^\infty (l+1)\mathbb{T}^{l+\frac{1}{2},l} + l\mathbb{T}^{l-\frac{1}{2},l},\end{aligned} \tag{23}$$

using the definition of the transmission coefficients, $\mathbb{T}^{jl}$.

In practice, one calculates these $\mathcal{S}$-matrix elements by numerically evaluating the logarithmic derivative of the channel wavefunction at some matching radius $r = a$, outside the range of V_{om}, in which the wavefunctions approach their asymptotic behavior. These logarithmic derivatives are called the channel R-matrix elements $R^{jl}(E)$; one can write the $\mathcal{S}$-matrix as a unitary transformation of this R-matrix [40]:

$$\mathcal{S}^{jl} = e^{2i\phi_l}\frac{1-L_l^* R^{jl}(E)}{1-L_l R^{jl}(E)}, \tag{24}$$

where L_l is a function of the asymptotic wavefunctions at the channel radius:

$$L_l = \frac{ka}{F_l(ka)^2 + G_l(ka)^2}\left[F_l(ka)F_k'(ka) + G_l(ka)G_l'(ka) + i\right], \tag{25}$$

where $G_l(ka)$ is the Coulomb-wavefunction of the second kind[1] and ϕ_l is the hard-sphere phase shift:

$$\phi_l = -\tan^{-1}\left(F_l(ka)/G_l(ka)\right). \tag{26}$$

[1]The Coulomb wavefunctions of the first and second kind, $F_l(\eta, z)$ and $G_l(\eta, z)$, reduce to $zj_l(z)$ and $z\eta_l(z)$, the spherical Bessel functions of the first and second kinds, when the Sommerfield parameter $\eta = 0$, e.g., for neutral projectiles.